Convection in fluid and porous media

Carr, Magda

Convection in Fluid and Porous Media

Magda Carr

A thesis presented for the degree of
Doctor of Philosophy

Numerical Analysis
Department of Mathematical Sciences
University of Durham
England

July 2003

Dedicated to

My family and the memory of BJ Goodwin.

Convection in Fluid and Porous Media

Magda Carr

Submitted for the degree of Doctor of Philosophy
July 2003

Abstract

The subject of convection in fluid and porous media is investigated. Particular attention is paid to penetrative convection. The first two chapters are devoted to penetrative convection when fluid overlies and saturates a porous medium. Penetrative convection is described by a quadratic equation of state in the first instance and via internal heating in the second. Linear instability analyses are performed in both cases. A surprising and striking array of streamlines are presented at the onset of convection. The streamlines exhibit novel behaviour when physical parameters of the problem are varied.

Penetrative convection in a horizontally isotropic porous layer is discussed next. Again penetrative convection is described by a quadratic equation of state and internal heating. The internally heated model is dealt with primarily as it yields a global nonlinear stability bound. The two models are shown to be mathematically adjoint and the nonlinear stability results compared with previously published linear ones. Good agreement between the two is seen.

The effect of convection on the evolution of under-ice meltponds is investigated next. Linear and nonlinear analyses are employed to yield instability and global stability results respectively. Discrepancy between the two is found and the region of possible subcritical instabilities is presented.

Finally convection in a porous medium is investigated via a cubic equation of state. It is found that unconditional nonlinear stability results can be established if Forchheimer theory is introduced. The results are compared to previously published linear ones and it is shown that the linear theory essentially captures the physics involved.

Declaration

The work in this thesis is based on research carried out in the Numerical Analysis Group, Department of Mathematical Sciences, University of Durham, England. No part of this thesis has been submitted elsewhere for any other degree or qualification and it is all my own work with the exception of chapters 2 & 4. Chapter 2 was written in collaboration with Prof B Straughan of the University of Durham, England, and chapter 4 with Mr S de Putter of the Technical University of Eindhoven, The Netherlands. In both instances the collaborating author contributed 50% of the work. The content of chapters 2, 4, 5, & 6 are published in [11–14].

Acknowledgements

It is with great pleasure and deepest gratitude that I thank my supervisor Prof Brian Straughan. The guidance, commitment and time which he has freely given me and the generosity and wisdom with which he has supervised me are immeasurable. I would also like to thank Prof Straughan for enhancing my knowledge of footballers from the 60's and 70's and being the first Mackem to admit what a good player Alan Shearer is.

I thank everyone in the Department of Mathematical Sciences at the University of Durham for their help and assistance. In particular I would like to thank Dr JV Armitage for his encouragement, advice and friendship. I pay a special mention to all members of the Numerical Analysis Group particularly, Dr JP Coleman for his time and support, and Imran M for saving myself and others precious time by preparing this LaTeX template.

Special thank also to Bamba (BJ Goodwin R.I.P) and Mr EM Morrison for fostering my love of mathematics in the early days. Thank to all of my friends, near and far. Last but not least I would like to thank my family, Mom, Dad, Lucy and Thomas. Your unconditional love and support was and *is* my inspiration and rock, thank you.

This work was supported by a research studentship of the Engineering and Physical Sciences Research Council.

Contents

List of Figures

List of Tables

Chapter 1

Introduction

The objective of this thesis is to investigate thermal convection in fluid and porous media via stability and instability analyses. The aim of this chapter is to introduce the underlying theory and provide a brief outline of the work done. We begin by explaining exactly what is meant by stability and instability in the context of this work. The governing equations exhibit stationary solutions which allow some simple flow patterns. If a system is in a stationary state this simply means that none of the variables describing it are a function of time. The main purpose of this thesis is to investigate what happens to a system which is in a stationary state when subjected to some disturbance. If the disturbance gradually dies and the stationary state is unaffected then the system is said to be stable. On the other hand if the disturbance grows and the system is affected such that it never reverts back to its initial state then it is said to be unstable. A system is only considered stable if it can be shown to be stable with respect to every disturbance to which it may be subject. On the other hand, a system is considered unstable if it can be shown to be unstable with respect to any one disturbance.

To clarify this concept and introduce some mathematical notation we begin with a simple illustrative example. Suppose u is a solution of the linear diffusion equation with a linear source term and subject to boundary and initial conditions as follows, (cf. Straughan

[94])

$$\begin{aligned} &\frac{\partial u}{\partial t} = \frac{\partial^2 u}{\partial x^2} + au, \qquad x \in (0,1), \quad t > 0, \\ &u(0,t) = u(1,t) = 0, \\ &u(x,0) = u_0(x). \end{aligned} \tag{1.1}$$

Here t and x are time and spatial point respectively, and a is some real, positive constant. The stationary solution, $u \equiv 0$, is clearly a solution of (1.1). To investigate the stability of this solution we introduce some perturbation (disturbance) to it. If all perturbations decay to zero with time t, then the solution is said to be stable. If just one disturbance can be found that grows in amplitude with time, then the solution is unstable.

Perturbations are introduced by a normal mode representation of the form

$$u(x,t) = e^{\sigma t + ikx}, \tag{1.2}$$

where k is a real number and σ (constant, possibly complex) is the growth rate. This is a suitable representation since $(1.1)_1$ is linear, and (1.2) allows the instability of the zero solution to be studied against any periodic disturbance in x. A full justification of the normal mode representation can be found in detail in Chandrasekhar [15], p.3-6. The sign of $Re(\sigma)$ determines whether the zero solution is stable or not. If $Re(\sigma) > 0$ then the perturbation will grow exponentially with time and clearly there will be instability. On the other hand if $Re(\sigma) < 0$ the normal modes will decay with time and there is stability.

Imposing boundary conditions $(1.1)_2$, the normal mode representation (1.2), reduces to the form

$$u(x,t) = e^{\sigma t}\sin kx, \qquad k = n\pi, \qquad n = \pm 1, \pm 2, \ldots.$$

Substituting this representation into $(1.1)_1$ yields

$$\sigma = -k^2 + a, \qquad \text{where} \quad k^2 = n^2\pi^2, \qquad n = \pm 1, \pm 2, \ldots.$$

Therefore, $\sigma \in \mathbb{R}$ and $\sigma < 0 \Leftrightarrow a < k^2 \Leftrightarrow a < k^2_{\min} = \pi^2$. So for $a < \pi^2$ we say there is linear stability. On the other hand if $a > \pi^2$ then $\sigma > 0$ for $n = 1$ and there is linear instability. Hence $a = \pi^2$ is the linear instability-stability boundary. In general the locus which separates instability and stability is known as the neutral stability curve. The neutral stability curve represents a marginal state between stability and instability.

This marginal state exhibits one of two kinds of motion, stationary ($\sigma \in \mathbb{R}$) or oscillatory ($\sigma \in \mathbb{C}$) . If the motion is stationary, perturbations grow (or are damped) aperiodically whereas if it is oscillatory they grow (or are damped) periodically. If instability sets in as stationary motion the principle of exchange of stabilities is said to hold. On the other hand if instability sets in as oscillatory motion then the system is said to be subject to overstability. One of the aims of this thesis is to generate neutral stability curves and investigate their state.

In the work that follows the governing systems under consideration are all nonlinear. While a linear instability analysis like that described above yields useful information for such systems, it is important that nonlinear results can be established as well. The energy method is an excellent means of doing this, cf. Straughan [94]. It can provide precise and practical information about the stability of a nonlinear system. To illustrate how the energy method may be implemented the linear system (1.1) is taken as a simple example again. It is noted at this point that the example is simply illustrative and the method applies to a nonlinear system in an analogous way though ad hoc techniques may be necessary to deal with the nonlinearities (see chapters 4-6).

To begin, an energy $E(t)$ is defined by

$$E(t) = \frac{1}{2}\|u\|^2,$$

where $\|\cdot\|$ denotes the norm on $L^2(0,1)$ (where $L^2(0,1)$ is the space of square integrable functions on $(0,1)$), i.e.,

$$\|u\|^2 = \int_0^1 u^2 dx.$$

Then differentiating $E(t)$ and using $(1.1)_1$ yields

$$\frac{dE}{dt} = \frac{1}{2}\int_0^1 \frac{\partial u^2}{\partial t}dx = \int_0^1 u\frac{\partial u}{\partial t}dx = \int_0^1 u\frac{\partial^2 u}{\partial x^2}dx + a\int_0^1 u^2 dx. \tag{1.3}$$

Integrating by parts and noting the boundary conditions, we note that

$$\int_0^1 u\frac{\partial^2 u}{\partial x^2}dx = \left[u\frac{\partial u}{\partial x}\right]_0^1 - \int_0^1 \left(\frac{\partial u}{\partial x}\right)^2 dx = -\|u_x\|^2,$$

where $u_x = \partial u/\partial x$. Hence (1.3) can be written as

$$\begin{aligned} \frac{dE}{dt} &= -\|u_x\|^2 + a\|u\|^2, \\ &= -a\|u_x\|^2 \left(\frac{1}{a} - \frac{\|u\|^2}{\|u_x\|^2}\right), \\ &\leq -a\|u_x\|^2 \left(\frac{1}{a} - \max_{\mathcal{H}} \frac{\|u\|^2}{\|u_x\|^2}\right), \end{aligned} \tag{1.4}$$

where $\mathcal{H}$ is the space of admissible functions,

$$\mathcal{H} = \left\{u \in C^2(0,1) | u = 0 \quad \text{when} \quad x = 0, 1\right\},$$

and $C^2(0,1)$ is the space of twice continuously differentiable functions on $(0,1)$. Suppose now that R_E is defined by

$$\frac{1}{R_E} = \max_{\mathcal{H}} \frac{\|u\|^2}{\|u_x\|^2},$$

then (1.4) becomes

$$\frac{dE}{dt} \leq -a\|u_x\|^2 \left(\frac{1}{a} - \frac{1}{R_E}\right).$$

Let $c = 1/a - 1/R_E$, then if $a < R_E$, $c > 0$, and Poincaré's inequality (see Appendix B.1) can be used to deduce that

$$\frac{dE}{dt} \leq -ac\pi^2\|u\|^2 = -2\pi^2 acE.$$

This implies

$$\frac{d}{dt}(e^{2\pi^2 act}E) \leq 0,$$

which integrates up to yield

$$E(t) \leq e^{-2\pi^2 act}E(0).$$

Recall that $E(t) = \frac{1}{2}\|u\|^2$; therefore

$$\|u\|^2 \leq e^{-2\pi^2 act}\|u_0\|^2 \to 0 \quad \text{as} \quad t \to \infty.$$

Hence it has been shown that provided $a < R_E$, $\|u\| \to 0$ at least exponentially as $t \to \infty$, and so the zero solution to (1.1) is stable.

To find R_E let $I_1 = \|u\|^2$, $I_2 = \|u_x\|^2$ and recall that

$$\frac{1}{R_E} = \max_{\mathcal{H}} \frac{I_1}{I_2}.$$

Suppose u is a maximising solution and consider solutions of the form $u + \epsilon\eta$ where ϵ is some constant and η is an arbitrary $C^2(0,1)$ function such that $\eta(0) = \eta(1) = 0$. Clearly the maximum occurs at $\epsilon = 0$ so,

$$\left[\frac{d}{d\epsilon}\left(\frac{I_1}{I_2}\right)\right]_{\epsilon=0} = \left[\frac{1}{I_2}\frac{dI_1}{d\epsilon} - \frac{I_1}{I_2^2}\frac{dI_2}{d\epsilon}\right]_{\epsilon=0} = \delta I_1 \left[\frac{1}{I_2}\right]_{\epsilon=0} - \frac{\delta I_2}{R_E}\left[\frac{1}{I_2}\right]_{\epsilon=0} = 0,$$

where δ stands for the derivative with respect to ϵ evaluated at $\epsilon = 0$. Hence it can be deduced that

$$R_E \delta I_1 - \delta I_2 = 0, \tag{1.5}$$

where

$$\delta I_1 = \left[\frac{d}{d\epsilon}\int_0^1 (u+\epsilon\eta)^2 dx\right]_{\epsilon=0} = 2\int_0^1 u\eta dx,$$
$$\delta I_2 = \left[\frac{d}{d\epsilon}\int_0^1 (u_x+\epsilon\eta_x)^2 dx\right]_{\epsilon=0} = 2\int_0^1 u_x\eta_x dx.$$

Therefore (1.5) yields

$$\int_0^1 (R_E u\eta - u_x\eta_x)dx = 0,$$

which can be integrated by parts to give

$$\int_0^1 \eta(R_E u + u_{xx})dx = 0.$$

Apart from the continuity and boundary conditions it must satisfy, η is arbitrary hence it can be concluded that,

$$\frac{d^2u}{dx^2} + R_E u = 0, \qquad u(0) = u(1) = 0. \tag{1.6}$$

This is known as the Euler-Lagrange equation for the example at hand. It yields an eigenvalue problem for R_E.

In the work that follows, the Chebyshev tau method (cf. Fox [32] and Orszag [75]), or the compound matrix method (cf. Drazin & Reid [24] and Ng & Reid [65–67]) are used in the linear and nonlinear analyses to yield generalised eigenvalue problems of the form,

$$A\mathbf{x} = \sigma B\mathbf{x},$$

where A and B are matrices and $\mathbf{x}$ is some vector, all of which depend upon the system under consideration. Straughan & Walker [95] applied these two techniques to linear

and nonlinear stability problems for convection in porous media. Their paper provides an excellent summary of the two aforementioned methods. They compare the techniques and highlight the advantages and disadvantages of both when investigating stability problems. Details of the numerical methods as employed here can be found in the relevant chapters and appendix A.

The general solution of (1.6) is given by

$$u = A \sin \sqrt{R_E} x + B \cos \sqrt{R_E} x,$$

where A, B are constants. The boundary condition $u(0) = 0$ implies that $B = 0$, hence

$$u = A \sin \sqrt{R_E} x.$$

For a non arbitrary solution suppose $A \neq 0$, then $u(1) = 0$ implies that

$$\begin{aligned} \sqrt{R_E} &= n\pi, \qquad \text{where} \qquad n = \pm 1, \pm 2, \ldots . \\ \text{i.e.} \qquad R_E &= \pi^2, 4\pi^2, 9\pi^2, \ldots . \end{aligned}$$

Recall that stability requires $a < R_E$. The minimum value of R_E is π^2 so as expected, $a < \pi^2$, is the stability bound of the zero solution to (1.1).

In general it is found that the energy method yields some critical threshold below which everything is stable and a linear instability analysis some bound above which everything is unstable. In the example above the energy method and normal mode analysis yield the same critical instability-stability boundary. This is due to the fact that the differential equation under consideration $(1.1)_1$ is linear. If nonlinearities are introduced then it is found that in general a nonlinear stability analysis will yield a different critical threshold to one obtained by a linear analysis. A linear analysis assumes that any perturbation is small and so neglects terms of quadratic order and higher, hence discrepancy between linear instability and nonlinear stability results can occur. One of the aims of this thesis, and energy theory in general, is to try and arrange that the two thresholds are as close together as possible and so reduce the possibility of subcritical instabilities which may occur below the linear instability bound and above the nonlinear stability threshold. Many techniques have been used to do this and the theory applied to a range of important physical problems. There are many references in the literature and significant advancement has been made in the last 50 years. For reference we mention some recent papers

and the citations therein namely, Basurto & Lombardo [5], Lombardo *et al.* [49, 50], and Mulone [64]. Many more references and a thorough discussion of the energy method and its subtleties can be found in Straughan [94].

Having established the underlying theory, a brief outline of each chapter is now given. In chapter 2 an accurate numerical calculation is presented for the onset of thermal convection in a two layer system in which water overlies and saturates a porous layer. The physical picture is such that water at the density maximum may be encompassed. To account for the fact that the density may have a maximum, an equation of state is adopted which expresses the density in the buoyancy force as a quadratic function of temperature. It is found that the onset of convection may have a bi-modal nature in which convection can be dominated by the porous medium or by the fluid depending on parameters which appear in the problem. The important parameters in this instance turn out to be the ratio of fluid to porous medium depth, the upper surface temperature, and a parameter representing non-dimensional permeability of the porous matrix. A surprising array of streamline patterns are found and presented at the onset of convection as one varies the appropriate parameters.

In chapter 3 a similar system to that described in chapter 2 is investigated. In this case however an alternative model is employed to describe thermal convection. Instead of employing a quadratic equation of state, a linear one is used and internal heat sinks are introduced in both layers to simulate convection. The internal sinks are found to have a dramatic effect on both the onset of convection and the size of the ensuing convection cells. It is found that the heat sink Q, in the fluid layer has a destabilising effect on the system whereas the heat sink Q_m, in the porous medium can be either stabilising or destabilising depending on the steady state temperature profile and the strength of Q. A range of streamlines are presented that exhibit novel behaviour when Q and Q_m are varied. The model is compared with that given in chapter 2 and when the two are mathematically adjoint they are shown to yield the same critical instability threshold but different eigenfunctions. It is also found that the initiating cell is not necessarily the strongest one. This curious behaviour is explained and illustrated with a range of streamline plots.

In chapter 4 convection in a horizontally isotropic porous layer is investigated primarily using an internal heat sink model and alternatively, a quadratic density temperature

law. Employing the heat sink model, it is shown that the temporal growth rate for the linearised system is real. A nonlinear energy analysis is also presented, yielding a global stability threshold i.e. a stability bound which is independent of the intial state of the system and without constraint. The heat sink model is compared to the quadratic density model and it is found that the linearised systems are adjoint, implying that the instability boundaries which can be derived from the two models are the same.

In chapter 5 a model for convection in the evolution of under-ice melt ponds is presented. The system exhibits two competing effects namely, a temperature gradient which is destabilising and a salt gradient which is stabilising. Density is assumed to have a dependence quadratic in temperature and linear in concentration. A linear instability analysis and a nonlinear stability analysis are both performed. The standard energy method does not yield unconditional stability so a weighted energy analysis is employed to achieve global results. The global stability bound is found to be independent of the salt field and a presentation of the region of possible subcritical instabilities is given.

In chapter 6 a nonlinear stability analysis of thermal convection in a saturated porous medium is presented again. In this case however, the medium is assumed isotropic, the density has a cubic temperature dependence and the equations of flow in the porous medium incorporate a Forchheimer drag term. Unconditional (global) stability is established using L^3 and L^4 norms and it is shown that L^2 theory is insufficient to obtain similar results.

Finally in chapter 7 some concluding remarks are made, the implications of this thesis discussed and some suggestions for future work are given.

Chapter 2

Penetrative Convection in a Superposed Porous-Fluid Layer via a Quadratic Density Law

The object of this chapter is to provide an accurate numerical calculation for the instability that arises due to penetrative convection when water overlies and saturates a layer of porous material. Penetrative convection refers to convective motion which begins in an unstable layer and penetrates into otherwise stable layer(s), cf. Veronis [102]. Penetrative convection has many applications in the real world. For example penetrative convection is believed to play an integral part in the formation of patterned ground, cf. George *et al.* [33]. Patterned ground is the natural arrangement of stones into regular shapes such as circles, stripes or polygons. Typically, it consists of stone borders with soil centres forming regular hexagonal stone nets. The regularity of the stone nets can be remarkable and quite striking, for example see the photographs given in Krantz *et al.* [44]. The size and shape of patterned ground tends to be the same at any one site but can vary in width for a single stone net, from about 4cm to 4m depending on location cf. Gleason [37]. In general, patterned ground tends to form above the timberline in the high mountains of the temperature zone, in remote locations beyond the tree line in the Arctic and Antarctic, and even under water in shallow Alpine lakes.

As well as being inherently fascinating, patterned ground is of significant geophysical interest as it can disclose clues to various climate conditions. For example relict patterns

can give clues to prehistoric climates, active patterns can be used to monitor mankind's impact on polar regions, and patterned ground on Mars [55–57] can be compared to that seen on Earth to further our understanding of climatic conditions in space. The formation and evolution of patterned ground has been discussed in geological literature for more than a century and is still a subject of debate, cf. Kessler & Werner [43] and Mann [58].

Gleason [37] and Krantz *et al.* [44] reported findings of hexagonal stone patterns on the bed of shallow alpine lakes in Wyoming and Colorado. McKay & Straughan [53] developed a porous-fluid layer model to study such under water patterned ground formation. They used a shooting method and assumed stationary convection. In this chapter we essentially use the model of McKay & Straughan but employ a more accurate numerical technique, namely the Chebyshev tau method. This allows for the possibility of oscillatory convection and yields many new streamline patterns.

The fundamental model for convection in a porous-fluid layer system is due to Nield [68], with an important extension in Nield [69]. Chen & Chen [17] also analysed the problem of thermal convection in a superposed two layer system in which a layer of fluid overlies and saturates a porous medium. The layer is heated from below with the bottom of the porous medium and the upper surface of the fluid both assumed fixed. Chen & Chen made the significant discovery that the linear instability neutral curves for the onset of convective motion, i.e., the Rayleigh number against wave number curves for which $\sigma = 0$, may be bi-modal in the sense that they possess two local maxima. These maxima correspond to a parameter range where convection is initiated in the fluid layer, or alternatively in the porous layer. The cell sizes are different depending on whether convection is dominated by the fluid or the porous layer. Further work on the superposed porous-fluid layer problem, also due to Chen & Chen [17], is the study of the onset of instability when both a thermal and a salt field are present. These writers employed an orthonormal shooting method to numerically calculate the eigenvalues.

In recent work Straughan [92, 93] has developed a Chebyshev tau D^2 method applicable to the porous-fluid layer thermal convection problem. Straughan [92] focused on the problem where the upper surface is exposed to the atmosphere and surface tension is important. Whereas in [93] the effect of the various fluid and porous matrix properties on the instability criteria were investigated. It was discovered that porous permeability may

have a strong effect and the interface condition between the fluid and the porous medium was crucial.

Since the eigenvalues occurring in porous-fluid convection problems are highly sensitive to changes in parameters, a very accurate numerical method such as a Chebyshev tau one is necessary. In Straughan [92, 93] it was found that all eigenvalues were real, but in the present work we find that the spectrum also contains complex conjugate pairs. Spurious eigenvalues may present a problem in hydrodynamical stability studies, see for example the comprehensive account by Dawkins *et al.* [22]. We have been careful to exclude such terms and this point is revisited in section 2.6. Further references to work on the porous-fluid convection problem can be found in Nield [70–72], and Nield & Bejan [73].

In this chapter we consider water saturating a porous medium with the water forming a layer of finite depth above. The lower surface at the bottom of the porous layer is maintained at a constant temperature of 0°C while the upper fluid layer is kept at a fixed temperature greater than this. When the upper temperature, T_U, is greater than 4°C we have a situation in which the water in the region $0 - 4$°C is in a potentially gravitationally unstable state while that above is stably stratified. This is due to the fact that the density of water is a maximum at approximately 4°C. Therefore convective instability may arise in the lower part of the layer and penetrate into the stable upper part. Thus the model is capable of describing penetrative convection. A careful numerical study of this instability is the goal of this chapter. This is the first time a highly accurate numerical technique has been applied to the problem, and we find that an array of complex fluid instability patterns may occur.

As well as patterned ground formation under water, penetrative convection in a porous-fluid layer system has many more important applications. For example there is speculation as to whether convection patterns may have a bearing on accelerated melting of the Arctic ice sheet, cf. Bogorodskii & Nagurnyi [9]. This is investigated in more detail in chapter 5 and the implications discussed at length in chapter 7. In addition there are many other applications for the porous-fluid flow system including contaminant transport due to flow of water under the Earth's surface, cf. Allen [2], Allen & Khosravani [3], Curran & Allen [20], El-Habel *et al.* [28], Ewing [29], Ewing & Weekes [30], flow of oil

in underground reservoirs, cf. Allen [1], Ewing [29], bio-remediation of contaminated ground, cf. Suchomel *et al.* [97,98], and hydrothermal synthesis in the growth of crystalline materials, cf. Chen *et al.* [18]. Penetrative convection in a single layer is also a subject receiving recent attention with very important applications. For example Zhang & Schubert [107, 108] reported a penetrative convection effect which may be important in planetary and stellar atmospheres and Krishnamurti [45] and Larson [46,47] reported penetrative convection effects when radiation is added to a standard model for cumulus convection.

Penetrative convection can be described in several different ways, at least five of which are discussed in detail in Straughan [91]. In this thesis we concentrate on two of the most widely employed models, namely a quadratic equation of state and internal heating. In chapter 6 the effect of a cubic equation of state is also investigated. The strengths and weaknesses of the various models are discussed in the relevant chapters and a comparison between models is often made.

In this chapter the penetrative effect is due to the fact that water has a density maximum at approximately 4°C. Hence we choose to model penetrative convection by a quadratic equation of state of the form, cf. Veronis [102],

$$\rho = \rho_0 \left[1 - \bar{\alpha}(T-4)^2\right], \tag{2.0.1}$$

where ρ, T, and $\bar{\alpha}$ are density, temperature, and thermal expansion, and ρ_0 is the density of water at 4°C. Detailed numerical studies of penetrative convection in a fluid layer employing a law like (2.0.1) are given in Chasnov & Tse [16] and Tse & Chasnov [100]. The buoyancy law (2.0.1) leads to non-Boussinesq effects. In a Boussinesq approximation ρ is linear in T and treated as a constant in all terms of the equation of motion except the term involving the external force. The basis for this is that there are flows in which the temperature (and hence density) variation are small yet the external force is not. Hence the variation of density is chosen to be neglected everywhere except in the external force term. The Boussinesq approximation simplifies the governing equations of hydrodynamics significantly. It is widely employed and its validity discussed at length in Chandrasekhar [15], p.16-18. Non-Boussinesq effects however are increasingly common and have been under much recent investigation, see e.g. Selak & Lebon [89], and Straughan [91, 94]. In this chapter we choose to employ a non-Boussinesq equation of

state. In the next chapter an alternative is given in which a Boussinesq approximation is used. A comparison of the two models is discussed in detail in chapter 3.

In the paper of Chen & Chen [17] the important parameter in their analysis is the ratio

$$\hat{d} = \frac{d}{d_m} = \frac{\text{depth of fluid layer}}{\text{depth of porous layer}}. \tag{2.0.2}$$

They interpret their findings by showing that for relatively small $\hat{d}$ (≤ 0.13) instability is initiated in and dominated by the porous medium. Otherwise, the mechanism changes and instability is dominated by the fluid layer. In the current work we find a very strong interplay between $\hat{d}$ and T_U, the temperature at the surface of the fluid layer. The influence of T_U and the quadratic law (2.0.1) can vastly change the findings as compared to those of Chen & Chen [17], and of Straughan [92, 93]. The non-dimensional permeability $\delta = \sqrt{K}/d_m$, where K is permeability and d_m is the depth of the porous layer, is also important in the current situation. In this chapter we find that streamline patterns for penetrative convection in a fluid overlying a porous layer are very different from what one finds for penetrative convection in a single layer of fluid or porous medium. We believe the present chapter contains new findings which will be of interest to anyone working in convection where a fluid overlies a porous layer.

2.1 Governing Equations

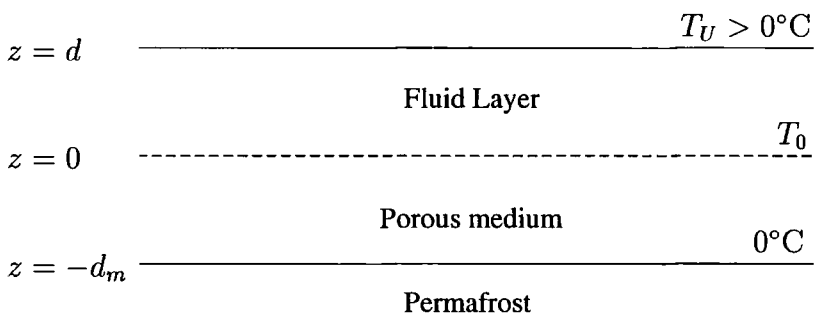

Figure 2.1: Schematic diagram of the governing system.

Consider a fluid (water) occupying the three dimensional layer $\{(x, y) \in \mathbb{R}^2\} \times \{z \in (0, d)\}$, saturating a porous medium superposed below $\{(x, y) \in \mathbb{R}^2\} \times \{z \in (-d_m, 0)\}$. The interface between the saturated porous medium and the water is at $z = 0$, see figure

2.1. The motion in the fluid layer can be described by the Navier-Stokes equations (see Chandrasekhar [15], p.11-13, for a derivation from first principles),

$$\frac{\partial v_i}{\partial t} + v_j \frac{\partial v_i}{\partial x_j} = -\frac{1}{\rho_o} p_{,i} + \nu \Delta v_i - \frac{1}{\rho_o} g\rho(T) k_i, \tag{2.1.1}$$

where v_i, t, x_i, p, ν, and g, are velocity, time, displacement, pressure, kinematic viscosity and gravity respectively and ρ the density, is assumed to be a quadratic function of temperature of the form (2.0.1). Standard indicial notation and the Einstein summation convention are employed throughout, and $\mathbf{k} = (0, 0, 1)^T$. The constant term in (2.0.1) can be absorbed into the pressure by defining a modified pressure $\hat{p}$ to be $p + g\rho_o(1 - 16\bar{\alpha})z$. Then, dropping the hat, (2.1.1) becomes

$$\frac{\partial v_i}{\partial t} + v_j \frac{\partial v_i}{\partial x_j} = -\frac{1}{\rho_o} p_{,i} + \nu \Delta v_i + g k_i \bar{\alpha} \left(T^2 - 8T\right). \tag{2.1.2}$$

Equation (2.1.2) together with an incompressibility condition (Chandrasekhar, p.11) and equation of energy balance (Chandrasekhar, p.18) yield the following system of governing equations

$$\begin{aligned} &\frac{\partial v_i}{\partial t} + v_j \frac{\partial v_i}{\partial x_j} = -\frac{1}{\rho_0} \frac{\partial p}{\partial x_i} + \nu \Delta v_i + g k_i \bar{\alpha} \left(T^2 - 8T\right), \\ &\frac{\partial v_i}{\partial x_i} = 0, \\ &\frac{\partial T}{\partial t} + v_i \frac{\partial T}{\partial x_i} = \frac{k_f}{(\rho_0 c_p)_f} \Delta T, \end{aligned} \tag{2.1.3}$$

where k_f and c_p are thermal conductivity and specific heat at constant pressure respectively. Equations (2.1.3) are assumed to hold for time $t > 0$, in the spatial domain $\{(x, y) \in \mathbb{R}^2, z \in (0, d)\}$. Subscript (or superscript) f or m denotes fluid or porous medium respectively, and the symbol Δ is the Laplace operator.

In the porous layer the equations of motion are described by Darcy's law. A full derivation, discussion and justification of Darcy's law can be found in Nield & Bejan [73]. In addition, the recent account by Brown [10] provides an interesting insight into Darcy's life and the making of his law. The buoyancy force is again given by (2.0.1); hence the governing equations for the porous medium are

$$\begin{aligned} &0 = -\frac{1}{\rho_0} \frac{\partial p^m}{\partial x_i} - \frac{\nu}{K} v_i^m + g k_i \bar{\alpha} \left(T_m^2 - 8T_m\right), \\ &\frac{\partial v_i^m}{\partial x_i} = 0, \\ &(\rho_0 c_p)^* \frac{\partial T_m}{\partial t} + (\rho_0 c_p)_f v_i^m \frac{\partial T_m}{\partial x_i} = k^* \Delta T_m. \end{aligned} \tag{2.1.4}$$

These equations hold on $\{(x,y) \in \mathbb{R}^2\} \times \{z \in (-d_m, 0)\} \times \{t > 0\}$, and the variables v_i^m, p_m, T_m are velocity, pressure and temperature in the porous medium. In $(2.1.4)_1$ the acceleration term has been omitted since this is believed to be small and negligible[1], cf. Nield & Bejan. Starred quantities are defined in terms of fluid and porous variables as

$$S^* = \phi S_f + (1-\phi) S_m,$$

where ϕ is the porosity and S stands for a physical variable such as thermal conductivity k.

The steady state solution whose stability is to be investigated is one where there is no fluid motion in either layer and the temperatures on the upper and lower boundaries are held fixed at constant temperatures, T_U and T_L, respectively, with $T_U > T_L$, $T_L = 0°\mathrm{C}$. The basic steady state solution to equations (2.1.3) and (2.1.4), denoted by $(\bar{v}_i, \bar{T}, \bar{p})$, $(\bar{v}_i^m, \bar{T}_m, \bar{p}^m)$, is then

$$\begin{aligned} &\bar{v}_i = 0, \qquad \bar{T} = \beta z + T_0, \qquad 0 \le z \le d, \\ &\bar{v}_i^m = 0, \qquad \bar{T}_m = \beta_m z + T_0, \qquad -d_m \le z \le 0, \end{aligned} \tag{2.1.5}$$

where $\beta = (T_U - T_0)/d, \beta_m = T_0/d_m$ and T_0 is the temperature at the interface. The temperature at the interface is found for known T_U by requiring continuity of temperature at $z = 0$ and continuity of the heat flux, viz.

$$k_f \frac{d\bar{T}}{dz} = k^* \frac{d\bar{T}_m}{dz} \qquad \text{at} \quad z = 0. \tag{2.1.6}$$

If we define $\epsilon_T = k_f/k^*$ then from (2.1.6) the relation, $T_0 = \epsilon_T T_U/(\epsilon_T + \hat{d})$, can be obtained. Furthermore we define $\mathcal{E} = \epsilon_T/(\epsilon_T + \hat{d})$, $\xi_1 = 4/T_U$, and ξ, ξ_m by

$$\xi = \frac{\xi_1 - \mathcal{E}}{1 - \mathcal{E}}, \qquad \xi_m = \frac{\xi_1 - \mathcal{E}}{\mathcal{E}}.$$

In our problem we need only specify T_U, and since ϵ_T and $\hat{d}$ are specified, T_0 does not enter the analysis directly and we know ξ and ξ_m.

[1] if the inertial term is included we have dependence on the porosity and an extra n eigenvalues are seen in the spectrum (n is the number of Chebyshev polynomials used in the numerical computation). However, the extra n eigenvalues do not appear in the upper part of the spectrum and so do not include the critical eigenvalue. The numerical value of the leading eigenvalue was computed with and without inertial effects and no significant difference was seen.

We are unaware of a specific existence theory which has been developed for the model outlined above. However, Rodrigues & Urbano [84] developed a mathematical existence theory for a general Darcy theory with ice present, and their analysis is a suitable starting point.

2.2 Perturbation Equations

In order to study the instability of the basic solutions (2.1.5) we introduce perturbations (u_i, θ, π), (u_i^m, θ^m, π_m), to these solutions and set,

$$v_i = \bar{v}_i + u_i, \quad T = \bar{T} + \theta, \quad p = \bar{p} + \pi,$$
$$v_i^m = \bar{v}_i^m + u_i^m, \quad T_m = \bar{T}_m + \theta^m, \quad p_m = \bar{p}_m + \pi_m.$$

The perturbation equations which arise from (2.1.3) and (2.1.4) may be shown to be,

$$\begin{aligned} &\frac{\partial u_i}{\partial t} + u_j \frac{\partial u_i}{\partial x_j} = -\frac{1}{\rho_0}\frac{\partial \pi}{\partial x_i} + \nu \Delta u_i - 2\bar{\alpha} g k_i (4 - \bar{T})\theta + \bar{\alpha} g k_i \theta^2, \\ &\frac{\partial u_i}{\partial x_i} = 0, \\ &\frac{\partial \theta}{\partial t} + u_i \frac{\partial \theta}{\partial x_i} = \frac{k_f}{(\rho_0 c_p)_f} \Delta\theta - \beta w, \end{aligned} \tag{2.2.1}$$

and,

$$\begin{aligned} &0 = -\frac{1}{\rho_0}\frac{\partial \pi^m}{\partial x_i} - \frac{\nu}{K} u_i^m - 2\bar{\alpha} g k_i (4 - \overline{T}^m)\theta^m + \bar{\alpha} g k_i \theta_m^2, \\ &\frac{\partial u_i^m}{\partial x_i} = 0, \\ &(\rho_0 c_p)^* \frac{\partial \theta^m}{\partial t} + (\rho_0 c_p)_f u_i^m \frac{\partial \theta^m}{\partial x_i} = k^* \Delta\theta^m - (\rho_0 c_p)_f \beta_m w^m, \end{aligned} \tag{2.2.2}$$

where $w = u_3$ and $w^m = u_3^m$.

To non-dimensionalise the above equations let,

$$u_i = U u_i^*, \qquad x_i = d x_i^*, \qquad \pi = P\pi^*, \qquad \theta = T^{\#}\theta^*, \qquad t = \mathcal{T} t^*,$$

$$u_i^m = U^m u_i^{m*}, \qquad x_i^m = d_m x_i^*, \qquad \pi^m = P^m \pi^{m*}, \qquad \theta^m = T^{m\#}\theta^{m*}, \qquad t = \mathcal{T}^m t^{m*},$$

where the starred quantities are dimensionless and the fluid and porous scalings are given by,

$$U = \frac{\nu}{d}, \qquad P = \frac{\rho_0 \nu U}{d}, \qquad T^{\#} = U\sqrt{\frac{\nu}{g\bar{\alpha}\lambda d}}, \qquad \mathcal{T} = \frac{d^2}{\nu},$$

$$U^m = \frac{\nu}{d_m}, \qquad P^m = \frac{\rho_0 \nu U^m}{d_m}, \qquad T^{m\#} = \nu\sqrt{\frac{Pr_m}{g\bar{\alpha}d_m K}}, \qquad \mathcal{T}^m = \frac{d_m^2}{\nu},$$

where $\lambda = k_f/(\rho_0 c_p)_f$, $Pr_m = \nu/\lambda_m$ and $\lambda_m = k^*/(\rho_0 c_p)_f$. In addition the fluid and porous Rayleigh numbers Ra and Ra_m are defined by

$$Ra = R^2 = \frac{g\bar{\alpha}d^5\beta^2}{\nu\lambda}, \qquad Ra_m = R_m^2 = \frac{Pr_m g\bar{\alpha}K d_m^3 \beta_m^2}{\nu^2}. \tag{2.2.3}$$

We also define the Darcy number $\delta = \sqrt{K}/d_m$, the Prandtl number $Pr = \nu/\lambda$, and $G_m = (\rho_0 c_p)^*/(\rho_0 c_p)_f$.

Then, omitting the stars, equations (2.2.1) and (2.2.2) can be rewritten in terms of non-dimensional variables as,

$$\begin{aligned}
&\frac{\partial u_i}{\partial t} + u_j\frac{\partial u_i}{\partial x_j} = -\frac{\partial \pi}{\partial x_i} + \Delta u_i + 2R(z-\xi)k_i\theta + Prk_i\theta^2,\\
&\frac{\partial u_i}{\partial x_i} = 0,\\
&Pr\left(\frac{\partial \theta}{\partial t} + u_i\frac{\partial \theta}{\partial x_i}\right) = \Delta\theta - Rw,
\end{aligned} \tag{2.2.4}$$

and,

$$\begin{aligned}
&\delta^2\frac{\partial \pi^m}{\partial x_i} = -u_i^m + 2R^m(z-\xi_m)k_i\theta^m + Pr_m k_i\theta_m^2,\\
&\frac{\partial u_i^m}{\partial x_i} = 0,\\
&Pr_m\left(G_m\frac{\partial \theta^m}{\partial t^m} + u_i^m\frac{\partial \theta^m}{\partial x_i}\right) = \Delta\theta^m - R^m w^m.
\end{aligned} \tag{2.2.5}$$

Equations (2.2.4) hold in the region $\{(x,y)\in\mathbb{R}^2\}\times\{z\in(0,1)\}\times\{t>0\}$ while (2.2.5) hold on $\{(x,y)\in\mathbb{R}^2\}\times\{z\in(-1,0)\}\times\{t^m>0\}$. The interface is $z=0$, the lower porous surface is now $z=-1$ and $z=1$ is the (upper) fluid surface.

2.3 Linearised Instability Theory

The linearised perturbation equations are derived from (2.2.4) and (2.2.5) by discarding quadratic terms. Since the resulting system is linear we may seek solutions of the form $u_i = u_i(\mathbf{x})e^{\sigma t}$, $\theta = \theta(\mathbf{x})e^{\sigma t}$, $\pi = \pi(\mathbf{x})e^{\sigma t}$, $u_i^m = u_i^m(\mathbf{x})e^{\sigma t}$, $\theta^m = \theta^m(\mathbf{x})e^{\sigma t}$, and $\pi^m = \pi^m(\mathbf{x})e^{\sigma t}$. This gives rise to an eigenvalue problem for the growth rate σ. In fact, there are an infinite number of eigenvalues σ_i, which may be ordered so that

$\sigma_1 \geq \sigma_2 \geq \ldots$. If $\sigma_1 > 0$ then instability occurs. The associated eigenfunction $\{u_i^{(1)}, \theta^{(1)}, \pi^{(1)}, u_i^{m(1)}, \theta^{m(1)}, \pi^{m(1)}\}$ yields the solution at the onset of instability. In particular, $\{u_i^{(1)}, u_i^{m(1)}\}$ yield the streamline curves which are included in section 2.7, to visualise the flow patterns. Likewise, the functions $\{\theta^{(1)}, \theta^{m(1)}\}$ yield the isotherm patterns.

The time scaling $t^m = t/\omega$ is introduced, then (2.2.4) and (2.2.5) yield the non-dimensional linearised perturbation equations

$$\begin{aligned} &\sigma u_i = -\pi_{,i} + \Delta u_i - 2R(\xi - z)\theta k_i, \\ &u_{i,i} = 0, \\ &\sigma Pr\theta = \Delta\theta - Rw, \end{aligned} \tag{2.3.1}$$

$$\begin{aligned} &\delta^2 \pi^m_{,i} = -u^m_i - 2R^m(\xi_m - z)\theta^m k_i, \\ &u^m_{i,i} = 0, \\ &\sigma\omega Pr_m G_m \theta^m = \Delta\theta^m - R^m w^m. \end{aligned} \tag{2.3.2}$$

The method of solution for these equations follows the work of Chandrasekhar [15]. The pressures π and π^m are eliminated by taking curlcurl of $(2.3.1)_1$ and $(2.3.2)_1$. The third component of the resulting equations are retained to find

$$\sigma\Delta w = \Delta^2 w - 2RM(z)\Delta^*\theta, \tag{2.3.3}$$

and

$$0 = \Delta w^m + 2R^m M^m(z)\Delta^*\theta^m, \tag{2.3.4}$$

where

$$M(z) = \xi - z, \qquad M^m(z) = \xi_m - z,$$

and Δ^* is the horizontal Laplacian,

$$\Delta^* = \frac{\partial^2}{\partial x^2} + \frac{\partial^2}{\partial y^2}.$$

A normal mode representation of w, θ, w^m and θ^m in (2.3.3), $(2.3.1)_3$, (2.3.4), and $(2.3.2)_3$ is now employed by setting,

$$\begin{aligned} w &= W(z)f(x,y), \qquad & \theta &= \Theta(z)f(x,y), \\ w^m &= W^m(z)f^m(x,y), \qquad & \theta^m &= \Theta^m(z)f^m(x,y), \end{aligned}$$

where $f(x,y)$ and $f^m(x,y)$ are horizontal plan forms which satisfy

$$\Delta^* f = -a^2 f, \qquad \Delta^* f^m = -a_m^2 f^m.$$

The plan forms reflect the horizontal shape of convection cells at the onset of instability. Bénard [7,8] demonstrated experimentally, that for a horizontal layer of fluid heated from below the ensuing motion at the onset of convection has a stationary cellular structure. The cells become equal and align themselves forming a regular horizontal pattern. Typically, the convection cells are hexagonal for which

$$f(x,y) = \cos\frac{1}{2}a(\sqrt{3}x + y) + \cos\frac{1}{2}a(\sqrt{3}x - y) + \cos ay,$$

cf. Straughan [94] and Drazin & Reid [24]. The wavenumber a is a measure of the "width" of the convection cell to the depth, d. In this way the cells may be periodically repeated in a pattern which tiles the (x,y) plane. The plan form in the porous medium has the same shape although $a = \hat{d}a_m$.

The fourth order equation (2.3.3), can be written as two second order equations by regarding $A = (D^2 - a^2)W$ as an independent variable where $D^2 = d^2/dz^2$. Using this and the normal mode representation of w, θ, w^m and θ^m in $(2.3.1)_3$, (2.3.3), $(2.3.2)_3$ and (2.3.4), results in having to solve five coupled second order equations to determine the critical growth rate σ, namely,

$$\begin{aligned} &(D^2 - a^2)W = A, \\ &(D^2 - a^2)A + 2RM(z)a^2\Theta = \sigma A, \\ &(D^2 - a^2)\Theta - RW = \sigma Pr\Theta, \end{aligned} \tag{2.3.5}$$

$$\begin{aligned} &(D^2 - a_m^2)W^m - 2R^m M^m(z)a_m^2\Theta^m = 0, \\ &(D^2 - a_m^2)\Theta^m - R^m W^m = \sigma\omega Pr_m G_m \Theta^m, \end{aligned} \tag{2.3.6}$$

where (2.3.5) hold on $z \in (0,1)$ while (2.3.6) hold on $z \in (-1,0)$. Coupling is through the boundary conditions.

2.4 Boundary Conditions

The upper surface of the water ($z = d$) is open to the atmosphere (tangential stress free) and held fixed at some constant temperature $T_U > 0°\text{C}$. Hence for an incompressible

fluid we have the boundary conditions

$$w = 0, \qquad w_{,zz} = 0, \qquad \theta = 0, \qquad \text{at} \quad z = d. \tag{2.4.1}$$

Condition $(2.4.1)_2$ is derived from the fact that an incompressible fluid at a free surface satisfies

$$u_{,x} + v_{,y} + w_{,z} = 0, \qquad \text{and} \qquad u_{,z} = v_{,z} = 0.$$

The lower boundary of the porous medium ($z = -d_m$) is held fixed and has temperature $T_L = 0°\text{C}$. Hence the lower boundary conditions are

$$w^m = 0, \qquad \theta^m = 0, \qquad \text{at} \quad z = -d_m. \tag{2.4.2}$$

At the interface $z = 0$, continuity of the normal components of velocity, temperature and heat flux are required, so

$$w = w^m, \qquad \theta = \theta^m, \qquad \lambda_f \frac{\partial \theta}{\partial z} = \lambda_m \frac{\partial \theta^m}{\partial z_m}. \tag{2.4.3}$$

Two additional conditions on $z = 0$ are needed. The first of these is continuity of normal stress, cf. Straughan [92],

$$\pi^m = \pi - 2\mu \frac{\partial w}{\partial z}. \tag{2.4.4}$$

For the second we employ a Beavers-Joseph boundary condition,

$$\frac{\partial u^\beta}{\partial z} = \frac{\alpha}{\sqrt{K}}(u^\beta - \hat{d} u_m^\beta), \qquad \beta = 1, 2, \tag{2.4.5}$$

where α is a coefficient depending on the fluid and porous medium under consideration. Further details of the last condition and alternatives are given in Nield & Bejan [73] and Straughan [93]. Condition (2.4.5) relates tangential stress to the relative velocity at the interface.

Using the relevant scalings the boundary and interface conditions can be written in non-dimensional form as:

$$\theta = w = w_{,zz} = 0, \qquad \text{on} \quad z = 1, \tag{2.4.6}$$

$$\theta^m = w^m = 0, \qquad \text{on} \quad z = -1, \tag{2.4.7}$$

and

$$
\begin{aligned}
&w^m = \frac{w}{\hat{d}}, \qquad \theta^m = \frac{\delta}{\sqrt{\hat{d}^3 \epsilon_T}}\theta, \qquad \frac{\partial \theta^m}{\partial z} = \delta\sqrt{\frac{\epsilon_T}{\hat{d}^5}}\frac{\partial \theta}{\partial z}, \\
&\hat{d}^2\pi^m = \pi - 2w_{,z}, \\
&\frac{\partial u^\beta}{\partial z} = \frac{\hat{d}\alpha}{\delta}(u^\beta - \hat{d}u_m^\beta), \qquad \beta = 1,2, \qquad \text{on} \quad z = 0.
\end{aligned} \tag{2.4.8}
$$

The boundary conditions (2.4.6)-(2.4.8) are now written in terms of their normal mode expansions to yield,

$$\Theta = W = A = 0, \qquad \text{on} \quad z = 1, \tag{2.4.9}$$

$$\Theta^m = W^m = 0, \qquad \text{on} \quad z = -1, \tag{2.4.10}$$

and

$$
\begin{aligned}
&W = \hat{d}W^m, \qquad \Theta^m = \frac{\delta}{\sqrt{\hat{d}^3\epsilon_T}}\Theta, \qquad D\Theta^m = \delta\sqrt{\frac{\epsilon_T}{\hat{d}^5}}D\Theta, \\
&2a^2DW - DA - \frac{\hat{d}^2}{\delta^2}DW^m = -\sigma DW, \\
&a^2W + A = \frac{\hat{d}\alpha}{\delta}(DW - \hat{d}\,DW^m), \qquad \text{on} \quad z = 0.
\end{aligned} \tag{2.4.11}
$$

Thus our goal is to solve (2.3.5) and (2.3.6) subject to the boundary conditions (2.4.9)-(2.4.11). Before describing the numerical method of solution note some useful relations, namely

$$\omega = \frac{\mathcal{T}}{\mathcal{T}_m} = \hat{d}^2, \qquad Pr_m = \epsilon_T Pr, \qquad R = \frac{1}{\delta}\sqrt{\frac{\hat{d}^5}{\epsilon_T^3}}R^m.$$

2.5 Numerical Method

In this section two variants of the Chebyshev tau method, the D and D^2 techniques are presented, cf. Dongarra *et al.* [23] and appendix A.1. Apart from numerical accuracy, the Chebyshev tau method enables us to calculate as many eigenvalues as we need which is useful in cases when the eigenvalues of interest are changing in parameter space. The eigenfunctions can also be calculated very easily via this method. The implementation of a Chebyshev tau method has several other advantages which are discussed in detail in Straughan [93].

The Chebyshev tau D^2 technique is used to find the majority of the numerical results presented here so this is considered first. In Dongarra *et al.* [23] the authors also discussed the D and D^4 methods. The power of D refers to the highest derivative being discretized. Dongarra *et al.* recommended the D^2 alternative as it has better growth rate properties than the D^4 case, whereas it makes more efficient use of the QZ algorithm than the D method, which requires matrices twice as large. We concentrate on the D^2 method, as recommended, but also include a description of the D method for completeness as the results obtained in the D method are used to independently check those of the D^2 case.

2.5.1 The Chebyshev tau D^2 method

Before implementing the Chebyshev tau D^2 method (2.3.5), (2.3.6), and (2.4.9)-(2.4.11) must be transformed to the Chebyshev domain $(-1,1)$. To do this let $\hat{z} = 2z - 1$ and $\hat{z}_m = -2z_m - 1$ in (2.3.5) and (2.3.6) respectively. Similarly conditions (2.4.9)-(2.4.11) are transformed by making the appropriate substitution for the fluid and porous terms. Then the fluid surface $z = 1$ becomes $\hat{z} = 1$ and the porous surface $z_m = -1$ becomes $\hat{z}_m = 1$ while the interface $z = 0 = z_m$ is transformed to $\hat{z} = -1 = \hat{z}_m$. Hence the eigenvalue problem (2.3.5)-(2.3.6) on the Chebyshev domain $(-1,1)$ (dropping the hats) is

$$\begin{aligned}
&(4D^2 - a^2)W = A,\\
&(4D^2 - a^2)A + 2RM(z)a^2\Theta = \sigma A,\\
&(4D^2 - a^2)\Theta - RW = \sigma Pr\Theta,\\
&(4D^2 - a_m^2)W^m - 2R^m M^m(z)a_m^2\Theta^m = 0,\\
&(4D^2 - a_m^2)\Theta^m - R^m W^m = \sigma\omega Pr_m G_m \Theta^m.
\end{aligned} \tag{2.5.1}$$

The corresponding boundary conditions are

$$\Theta = W = A = \Theta^m = W^m = 0, \qquad \text{on} \quad z = 1, \tag{2.5.2}$$

and the interfacial terms,

$$
\begin{aligned}
&W = \hat{d}W^m, \qquad \Theta^m = \frac{\delta}{\sqrt{\hat{d}^3\epsilon_T}}\Theta, \qquad -D\Theta^m = \delta\sqrt{\frac{\epsilon_T}{\hat{d}^5}}D\Theta, \\
&2a^2DW - DA + \frac{\hat{d}^2}{\delta^2}DW^m = -\sigma DW, \\
&a^2W + A = \frac{2\hat{d}\alpha}{\delta}(DW + \hat{d}\,DW^m), \qquad \text{on} \quad z = -1,
\end{aligned}
\tag{2.5.3}
$$

where $z \in (-1, 1)$, $M = \xi - 1/2 - z/2$ and $M^m = \xi_m + 1/2 + z/2$.

The five quantities W, A, Θ, W_m and Θ_m are regarded as being independent variables and expanded as Chebyshev series, i.e.

$$
\begin{aligned}
&W = \sum_{n=0}^{N+2} W_n T_n(z), \qquad A = \sum_{n=0}^{N+2} A_n T_n(z), \qquad \Theta = \sum_{n=0}^{N+2} \Theta_n T_n(z), \\
&W_m = \sum_{n=0}^{N+2} W_n^m T_n(z), \qquad \Theta^m = \sum_{n=0}^{N+2} \Theta_n^m T_n(z).
\end{aligned}
\tag{2.5.4}
$$

The series above are truncations of an infinite series. Due to the truncation, the tau method argues that rather than solving (2.5.1) one instead solves

$$
\begin{aligned}
&(4D^2 - a^2)W - A = \tau_1 T_{N+1} + \tau_2 T_{N+2}, \\
&(4D^2 - a^2)A + 2RM(z)a^2\Theta - \sigma A = \tau_3 T_{N+1} + \tau_4 T_{N+2}, \\
&(4D^2 - a^2)\Theta - RW - \sigma Pr\Theta = \tau_5 T_{N+1} + \tau_6 T_{N+2}, \\
&(4D^2 - a_m^2)W^m - 2R^m M^m(z)a_m^2\Theta^m = \tau_7 T_{N+1} + \tau_8 T_{N+2}, \\
&(4D^2 - a_m^2)\Theta^m - R^m W^m - \sigma\omega Pr_m G_m \Theta^m = \tau_9 T_{N+1} + \tau_{10} T_{N+2},
\end{aligned}
$$

where $\tau_1, \ldots, \tau_{10}$, the tau coefficients, maybe used to measure the error associated with the truncation of (2.5.4), cf. Dongarra *et al.* [23]. For our purposes, it is not necessary to calculate the tau coefficients as it is sufficient in practice to simply observe convergence of the eigenvectors to assess accuracy.

Equations (2.5.1)-(2.5.3) can be expressed as a generalised matrix eigenvalue problem of the form

$$
A\mathbf{x} = \sigma B\mathbf{x}. \tag{2.5.5}
$$

To illustrate this more clearly, and establish the form of the matrices A and B we take the inner product of each equation in (2.5.1) with some Chebyshev polynomial T_k (cf.

appendix A.1). The Chebyshev polynomials have the following orthogonality property,

$$(T_n, T_k) = \int_{-1}^{1} \frac{T_n(x)T_k(x)}{\sqrt{1-x^2}} dx = \frac{\pi}{2} c_k \delta_{nk}. \tag{2.5.6}$$

where

$$c_k = \begin{cases} 2 & \text{if } k = 0, \\ 1 & \text{if } k > 0. \end{cases}$$

This is exploited as follows. Consider $(2.5.1)_1$, taking inner products with some T_k we find,

$$(4D^2W, T_k) - (a^2W, T_k) - (A, T_k) = 0,$$

which can be expanded using (2.5.4), (2.5.6), and the fact that the derivative of a Chebyshev polynomial is a linear combination of lower order Chebyshev polynomials to yield,

$$\sum_{n=0}^{N+2} 4D^2W_n - a^2W_k - A_k = 0. \tag{2.5.7}$$

Similarly an entirely analogous argument can be applied to $(2.5.1)_2$ to deduce that,

$$\sum_{n=0}^{N+2} 4D^2A_n - a^2A_k + (2RM(z)a^2\Theta, T_k) = \sigma A_k. \tag{2.5.8}$$

The third term of (2.5.8) can be written as,

$$(2RM(z)a^2\Theta, T_k) = 2Ra^2(\xi - 1/2)(\Theta, T_k) - Ra^2(z\Theta, T_k). \tag{2.5.9}$$

To expand $(z\Theta, T_k)$ note the following,

$$\begin{aligned} z\Theta &= T_1 \sum_{n=0}^{N+2} \theta_n T_n = \sum_{n=0}^{N+2} \left(\frac{\theta_n}{2} (T_{1+n} + T_{|1-n|}) \right) \\ &= \theta_0 T_1 + \frac{1}{2}\theta_1(T_0 + T_2) + \ldots + \frac{1}{2}\theta_{N+2}(T_{N+1} + T_{N+3}). \end{aligned}$$

So, taking inner products with T_0, T_1 and T_k for $k = 2, \ldots, N+2$, yields,

$$\theta_1 = \frac{2}{\pi}(z\Theta, T_0), \quad \theta_0 + \frac{\theta_2}{2} = \frac{2}{\pi}(z\Theta, T_1), \quad \frac{\theta_{k-1}}{2} + \frac{\theta_{k+1}}{2} = \frac{2}{\pi}(z\Theta, T_k),$$

which can be expressed in matrix form as,

$$\begin{pmatrix} 0 & \frac{1}{2} & 0 & 0 & \ldots & 0 \\ 1 & 0 & \frac{1}{2} & 0 & \ldots & 0 \\ 0 & \frac{1}{2} & 0 & \frac{1}{2} & \ldots & 0 \\ \vdots & & \ddots & & & \vdots \\ 0 & & & \frac{1}{2} & 0 & \frac{1}{2} \\ 0 & & & 0 & \frac{1}{2} & 0 \end{pmatrix} \begin{pmatrix} \theta_0 \\ \theta_1 \\ \theta_2 \\ \vdots \\ \vdots \\ \theta_{N+2} \end{pmatrix} = \begin{pmatrix} \frac{1}{\pi}(z\Theta, T_0) \\ \frac{2}{\pi}(z\Theta, T_1) \\ \frac{2}{\pi}(z\Theta, T_2) \\ \vdots \\ \vdots \\ \frac{2}{\pi}(z\Theta, T_{N+2}) \end{pmatrix} \tag{2.5.10}$$

Let the coefficient matrix in (2.5.10) be denoted by Z. Then expressing (2.5.7) and (2.5.8) in matrix form and applying an entirely similar argument to $(2.5.1)_3$, $(2.5.1)_4$, and $(2.5.1)_5$ we can write (2.5.1) as the eigenvalue problem,

$$\begin{pmatrix} 4D^2 - a^2 I & -I & 0 & 0 & 0 \\ 0 & 4D^2 - a^2 I & * & 0 & 0 \\ -RI & 0 & 4D^2 - a^2 I & 0 & 0 \\ 0 & 0 & 0 & 4D^2 - a_m^2 I & \# \\ 0 & 0 & 0 & -R^m I & 4D^2 - a_m^2 I \end{pmatrix} \begin{pmatrix} W \\ A \\ \Theta \\ W^m \\ \Theta^m \end{pmatrix}$$

$$= \sigma \begin{pmatrix} 0 & 0 & 0 & 0 & 0 \\ 0 & I & 0 & 0 & 0 \\ 0 & 0 & PrI & 0 & 0 \\ 0 & 0 & 0 & 0 & 0 \\ 0 & 0 & 0 & 0 & \omega Pr_m G_m I \end{pmatrix} \begin{pmatrix} W \\ A \\ \Theta \\ W^m \\ \Theta^m \end{pmatrix}$$

where I is the identity matrix,

$$* = 2Ra^2(\xi - \frac{1}{2})I - Ra^2 Z, \qquad \# = -2R^m a_m^2(\xi^m + \frac{1}{2})I - R^m a_m^2 Z,$$

and,

$$W = (W_0, W_1, \ldots, W_{N+2})^T, \quad A = (A_0, A_1, \ldots, A_{N+2})^T,$$
$$\Theta = (\theta_0, \theta_1, \ldots, \theta_{N+2})^T, \quad W^m = (W_0^m, W_1^m, \ldots, W_{N+2}^m)^T,$$
$$\Theta^m = (\theta_0^m, \theta_1^m, \ldots, \theta_{N+2}^m)^T.$$

The operator D^2 is written in matrix form (cf. Dongarra *et al.* [23] and appendix A.1) and the $m(N+2)$ and $m(N+3)$ rows of the matrix blocks in the system above, $m = 1, \ldots, 5$, are replaced with the discrete forms of the boundary conditions. The boundary conditions (2.5.2) and (2.5.3) are realised with the aid of the relations $T_n(\pm 1) = (\pm 1)^n$ and $T_n'(\pm 1) = (\pm 1)^{n-1} n^2$. This results in the generalised $5(N+3) \times 5(N+3)$ matrix eigenvalue problem of the form

$$A\mathbf{x} = \sigma B\mathbf{x}. \tag{2.5.11}$$

This generalised matrix eigenvalue problem is solved for the eigenvalues $\sigma^{(n)}$, $n = 1, 2, \ldots$, and the eigenfunctions $\mathbf{x}^{(n)}$ with the aid of the QZ algorithm, cf. Moler & Stewart [62], which we employed via the NAG routine F02BJF.

2.5.2 The Chebyshev tau D method

In the previous section the transformed eigenvalue problem (2.5.1)-(2.5.3) was written as a system of 2nd order equations. To implement a Chebyshev tau D method the system is rewritten in terms of first order equations only,

$$\begin{aligned}
&2DW - A_1 = 0, \quad 2DA_1 - A_2 = 0, \quad 2DA_2 - A_3 = 0,\\
&2D\Theta - B = 0, \quad 2D\Theta^m - C = 0, \quad 2DW^m - E = 0,\\
&2DA_3 - 2a^2A_2 + a^4W + 2RMa^2\Theta = \sigma(A_2 - a^2W),\\
&2DB - a^2\Theta - RW = \sigma Pr\Theta,\\
&2DE - a_m^2W^m - 2R^mM^ma_m^2\Theta^m = 0,\\
&2DC - a_m^2\Theta^m - R^mW^m = \sigma\omega Pr_mG_m\Theta^m.
\end{aligned} \tag{2.5.12}$$

The boundary conditions are now given by

$$\Theta = W = A_2 = \Theta^m = W^m = 0, \qquad \text{on} \quad z = 1, \tag{2.5.13}$$

and the interfacial conditions by,

$$\begin{aligned}
&W = \hat{d}W^m, \qquad \Theta^m = \frac{\delta}{\sqrt{\hat{d}^3\epsilon_T}}\Theta, \qquad C = \delta\sqrt{\frac{\epsilon_T}{\hat{d}^5}}B,\\
&-3a^2A_1 + A_3 + \frac{\hat{d}^2}{\delta^2}E = \sigma A_1,\\
&A_2 = \frac{\hat{d}\alpha}{\delta}(A_1 - \hat{d}\,E), \qquad \text{on} \quad z = -1.
\end{aligned} \tag{2.5.14}$$

Using arguments entirely analogous to those used in the D^2 case, (2.5.12) can be written as the generalised eigenvalue problem,

$$\begin{pmatrix}
2D & -I & 0 & \cdots & & & & & & 0\\
0 & 2D & -I & 0 & \cdots & & & & & 0\\
0 & 0 & 2D & -I & 0 & \cdots & & & & 0\\
a^4I & 0 & -2a^2I & 2D & * & 0 & \cdots & & & 0\\
0 & 0 & 0 & 0 & 2D & -I & 0 & \cdots & & 0\\
-RI & 0 & 0 & 0 & -a^2I & 2D & 0 & 0 & 0 & 0\\
0 & \cdots & & & 0 & 0 & 2D & I & 0 & 0\\
0 & \cdots & & & 0 & a_m^2I & 2D & R^mI & 0 & \\
0 & \cdots & & & & 0 & 0 & 2D & I & \\
0 & \cdots & & & & & \# & a_m^2I & 2D &
\end{pmatrix}
\begin{pmatrix} W\\ A_1\\ A_2\\ A_3\\ \Theta\\ B\\ \Theta^m\\ C\\ W^m\\ E \end{pmatrix}$$

$$= \sigma \begin{pmatrix} 0 & 0 & \cdots & 0 \\ 0 & 0 & 0 & \cdots & 0 \\ 0 & 0 & 0 & 0 & \cdots & 0 \\ -a^2 I & 0 & I & 0 & 0 & \cdots & 0 \\ 0 & \cdots & 0 & 0 & 0 & \cdots & 0 \\ 0 & \cdots & PrI & 0 & 0 & \cdots & 0 \\ 0 & \cdots & 0 & 0 & 0 & 0 & 0 \\ 0 & \cdots & -\omega Pr_m G_m I & 0 & 0 & 0 \\ 0 & \cdots & 0 & 0 & 0 \\ 0 & \cdots & 0 & 0 \end{pmatrix} \begin{pmatrix} W \\ A_1 \\ A_2 \\ A_3 \\ \Theta \\ B \\ \Theta^m \\ C \\ W^m \\ E \end{pmatrix}$$

where $* = 2Ra^2(\xi - 1/2)I - Ra^2 Z$ and $\# = 2R_m a_m^2(\xi_m + 1/2)I + R_m a_m^2 Z$. Z is defined as in the D^2 case and the operator D is written in matrix form (cf. Dongarra *et al.* [23] and appendix A.1).

The $m(N+2)$ rows of the matrix blocks, $m = 1, \ldots, 10$, are replaced with the discrete forms of the 10 boundary conditions (2.5.13) and (2.5.14). This results in the $10(N+3) \times 10(N+3)$ (twice as large as the D^2 case) generalised matrix eigenvalue problem of the form

$$A\mathbf{x} = \sigma B\mathbf{x}. \tag{2.5.15}$$

Again this is solved for the eigenvalues $\sigma^{(n)}$, $n = 1, 2, \ldots$, and the eigenfunctions $\mathbf{x}^{(n)}$ with the aid of the QZ algorithm. The results of the D method were then used as an independent check of those in the D^2 case.

2.6 Computational Results

In this section computational results obtained by varying the three parameters $\hat{d}, T_U$, and δ are reported. Other parameter variations for the non-penetration case are considered in Straughan [93]. The novelty of the results presented here is due to the penetration effect and we highlight this. The Chebyshev tau method allows us to obtain highly accurate results with very few polynomials. In our computations we employed 30 polynomials. It is curious to note that for the parameter values selected we always find the critical

eigenvalue $\sigma^{(1)}$ to be real. The spectrum is such that $\sigma^{(1)} \in \mathbb{R}$ although other eigenvalues further down the list may occur as complex conjugate pairs. The validity of all eigenvalues was checked by carefully controlling the convergence of each eigenvector. This is important since spurious eigenvalues are often found in problems of this nature. Spurious eigenvalues are numbers which may appear in the eigenvalue list but are not solutions to the eigenvalue problem. Practical checks as to whether an eigenvalue is spurious involve changing the number of polynomials or examining the convergence of the associated eigenvector. If an eigenvalue is spurious then changing the number of polynomials is accompanied by a significant change in the "eigenvalue", and the components of the eigenvector are not observed to converge. An inspiring account of how spurious eigenvalues may arise in hydrodynamic stability problems is given by Dawkins *et al.* [22]. All the eigenvalues we computed, including the complex conjugate pairs, are believed to be solutions of the problem.

We find that the streamlines and isotherms at the onset of convection may display striking patterns with a many cellular structure. This effect can only be seen by carefully computing streamline patterns or by careful analysis of the eigenfunction. The many cellular structure is not obvious from the eigenfunction with the naked eye (see e.g. figure 2.18). Due to the highly sensitive streamline structure observed we note that it is essential to employ a highly accurate numerical technique like the Chebyshev tau D^2 one to detect such fine detail.

In our computations we discover striking differences with the findings of Straughan [92, 93] and Chen & Chen [17]. These papers typically found that the neutral curves showed the instability pattern changed from being dominated by the porous medium to being dominated by the fluid layer for $\hat{d}$ in the region of 0.1. In Straughan [93] the parameter α in the boundary condition (2.4.5) was found to play an important role in that if $\alpha > 0.8$ the porous medium dominates the instability. However, for many fluids and porous media, α lies in the range 0.1 to 0.8 and then the changeover is of order $\hat{d} = 0.1$ ($\hat{d} = \mathrm{O}(0.1)$) . In this work we discover that the changeover point also depends strongly on the upper temperature of the fluid layer, T_U. Thus the penetrative convection effect is very important. For example, with $T_U = \mathrm{O}(8°\mathrm{C})$ the changeover occurs for $\hat{d} = \mathrm{O}(1)$ whereas when $T_U = \mathrm{O}(4°\mathrm{C})$ the changeover is in the region $\hat{d} = \mathrm{O}(0.1)$.

We also observe that penetrative convection in the fluid overlying a porous medium situation is very different from penetrative convection in a single fluid layer, or penetrative convection in a layer of saturated porous material. The interface in the two layer situation plays an important role. For example, in the one layer fluid or porous problem true penetrative convection, i.e. the formation of two convection cells in the vertical, occurs only when $T_U > 6.4°\text{C}$ and three cells form only when $T_U > \text{O}(21°\text{C})$, cf. Straughan [91]. However in the two layer porous-fluid problem with $\hat{d} = 0.4$ we already see two fluid cells when $T_U = 5°\text{C}$ and when $T_U = 6°\text{C}$ three cells have formed.

We stress that we have not seen the penetrative convection problem studied in the fluid overlying a porous medium problem and the numerical findings are quite striking and very different from anything we have seen in previous works on penetrative convection, or in convection in a porous-fluid layer system. We also stress that our results can only be observed with a highly accurate numerical method and we strongly advocate the use of the Chebyshev tau D^2 method for this and related problems.

2.7 Numerical Findings

In this section a selection of our numerical findings are presented. We point out that these are a small amount of the many graphs computed. The idea is to present a representative selection highlighting some of the novel features we have found. Throughout all calculations we select $Pr = 6$ (the Prandtl number for water) and fix the parameters ϵ_T, G_m and α at the values $0.7, 10$ and 0.1 respectively, cf. Straughan [93].

2.7.1 Variation of the neutral curves with $\hat{d}$, T_U and δ

In figures 2.2-2.4 we present the linear instability neutral curves, i.e., the porous Rayleigh number against porous wavenumber curves such that $\sigma = 0$, for various values of $\hat{d}, T_u$ and δ. Since the time representations of $u_i, \theta, \pi, u_i^m, \theta^m$ and π^m are of the form $e^{\sigma t}$, it is clear that above the neutral curves ($\sigma > 0$) the system is unstable. For a fixed wavenumber a_m, one finds a value for Ra_m. Since all values of a_m are allowed, we let a_m vary from $0 \to \infty$ and the minimum value of Ra_m yields the critical value above which instability will commence.

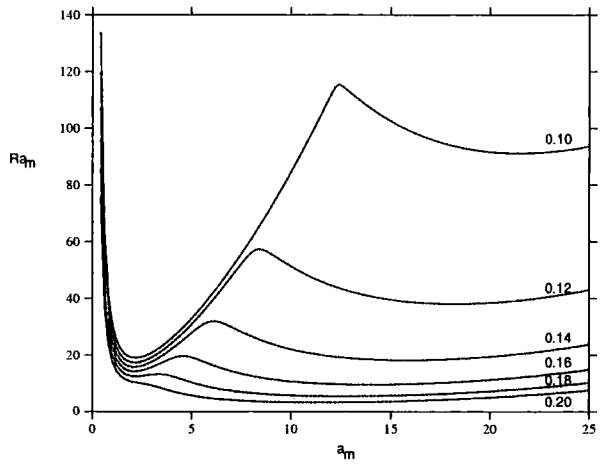

Figure 2.2: Neutral instability curves, Ra_m against a_m. $T_U = 4°C$, $\delta = 0.002$, $\hat{d}$ varies as shown on graph.

In figure 2.2 we fix T_U and δ at 4°C and 0.002 respectively and vary $\hat{d}$. The bi-modal nature of the neutral curves is clearly seen. Of course, with an upper temperature of 4°C the whole layer has a tendency to be unstable and penetrative convection will not be witnessed. This is analogous to the computations of Straughan [93] and we expect to find the switch from porous to fluid dominated convection with $\hat{d}$ in the range we have. In fact, the absolute minimum on each curve represents where instability commences. Thus, for $\hat{d} = 0.16, 0.18, 0.2$, the minimum of the curve lies on the fluid dominated part with a_m larger (narrower convection cells confined mostly in the fluid) whereas for $\hat{d} = 0.1, 0.12, 0.14$, the minimum of the curve is in the porous dominated part with a_m smaller (wider convection cells, with convection occurring strongly in the porous medium).

In figure 2.3 we fix $\hat{d}$ and δ at 0.4 and 0.002 respectively and show the neutral curves for T_U varying from 5°C through to 5.4°C. Note that for $T_U = 5°C$ to 5.3°C the fluid dominates the convection pattern with large wavenumbers but when $T_U = 5.4°C$ the pattern changes and convection is driven by the porous medium with a corresponding smaller wavenumber.

In figure 2.4 we fix $\hat{d}$ and T_U at 1 and 8.2°C respectively and show the neutral curves for δ varying from 0.001 to 0.01. We note that for $\delta = 0.001$ and 0.002 the fluid dominates the convection pattern with large wavenumbers but when δ is increased to 0.003 the pattern changes and convection is driven by the porous medium with a corresponding

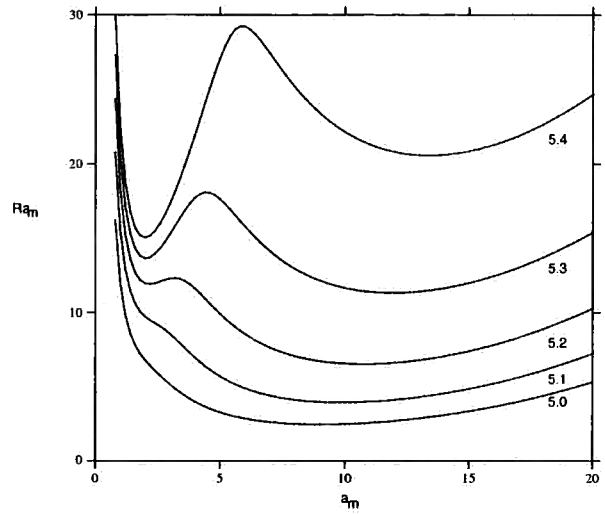

Figure 2.3: Neutral instability curves, Ra_m against a_m. $\delta = 0.002$, $\hat{d} = 0.4$, $T_U(°\mathrm{C})$ varies as shown on graph.

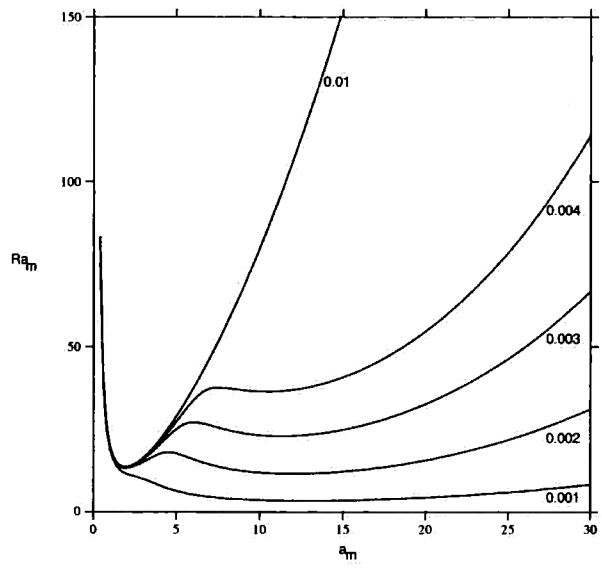

Figure 2.4: Neutral instability curves, Ra_m against a_m. $T_U = 8.2°\mathrm{C}$, $\hat{d} = 1$, δ varies as shown on graph.

smaller wavenumber.

Having computed and inspected several more instability curves, table 2.1 was constructed. Table 2.1 illustrates the range in which T_U must be to see the interchange where instability moves from fluid to porous (or porous to fluid) dominated convection. An approximate value, T_U^{sw}, at which this occurs is listed. Clearly the smaller $\hat{d}$ the lower the value of T_U^{sw} (as expected from figures 2.2-2.3). In fact it can be seen from table 2.1 that $\hat{d}$ and T_U^{sw} are essentially proportional. A change of 0.2 in $\hat{d}$ corresponds to an approximate change of 1°C in T_U^{sw}.

$\hat{d}$	Range of T_U (°C)	Approximate value of T_U^{sw} (°C)
2.00	$13.05 < T_U^{sw} \lessapprox 13.10$	13.10
1.80	$12.10 \lessapprox T_U^{sw} < 12.15$	12.10
1.60	$11.15 \lessapprox T_U^{sw} < 11.20$	11.15
1.40	$10.15 < T_U^{sw} \lessapprox 10.20$	10.20
1.20	$9.20 \lessapprox T_U^{sw} < 9.25$	9.20
1.00	$8.20 < T_U^{sw} \lessapprox 8.25$	8.25
0.50	$5.80 \lessapprox T_U^{sw} < 5.85$	5.80
0.40	$5.30 < T_U^{sw} \lessapprox 5.35$	5.35
0.30	$4.80 < T_U^{sw} \lessapprox 4.85$	4.85
0.20	$4.35 < T_U^{sw} \lessapprox 4.40$	4.40
0.18	$4.25 < T_U^{sw} \lessapprox 4.30$	4.30
0.16	$4.15 \lessapprox T_U^{sw} < 4.20$	4.15
0.14	$3.90 < T_U^{sw} \lessapprox 3.95$	3.95

Table 2.1: The range and approximate value of T_U (°C) in which a switch in dominance occurs for $\hat{d}$ varying, $\delta = 0.002$.

Figures 2.2-2.4 show respectively, that as $\hat{d}$ increases the system becomes less stable (the instability curves shift down), and as T_U and δ increase the system becomes more stable (the instability curves shift up). It can be concluded then from table 2.1, and the neutral curves presented above, that the onset of convection, and indeed which layer dominates it, depends strongly upon $\hat{d}, T_U$ and δ (for ϵ_T, G_m, Pr and α fixed).

2.7.2 Streamline and isotherm patterns

The neutral curves already show that a variety of interesting behaviour is found when penetrative convection is combined with the porous-fluid convection problem. However, it is by looking at the streamline patterns that the structure of the cell patterns can clearly be seen.

In the governing model and the plan form of the normal mode expansion, it was assumed that a convection cell must be three dimensional. Reproducing three dimensional streamlines is very difficult. Instead we choose to simplify the problem by concentrating on a two dimensional roll cell, cf. McKay & Straughan [53]. To ensure continuity at $z = 0$ and show graphically the effect on the flow of varying $\hat{d}$, we must first dimensionalise the eigenfunctions found via the Chebyshev tau D^2 method. We do this as follows.

Case 1: $\hat{d} < 1 \quad (d < d_m)$

Fix $d_m = U_m = T^{m\#} = 1$ then

$$\begin{aligned} w &= \frac{1}{\hat{d}} w^*, \qquad x = \hat{d}x^*, \qquad w_m = W_m^*, \qquad x_m = x_m^*, \\ \theta &= \frac{\delta}{\sqrt{\epsilon_T \hat{d}^3}} \theta^*, \qquad \theta^m = \theta^{m*}. \end{aligned} \tag{2.7.1}$$

Case 2: $\hat{d} \geq 1 \quad (d \geq d_m)$

Fix $d = U = T^{\#} = 1$ then

$$\begin{aligned} w &= w^*, \qquad x = x^*, \qquad w_m = \hat{d} W_m^*, \qquad x_m = \frac{1}{\hat{d}} x_m^*, \\ \theta &= \theta^*, \qquad \theta^m = \frac{\sqrt{\epsilon_T \hat{d}^3}}{\delta} \theta^{m*}, \end{aligned} \tag{2.7.2}$$

where the starred quantities denote non-dimensional terms.

We choose the planform for a two dimensional roll cell to be

$$g_c(x) = \cos a_c x, \qquad x \in \left[-\frac{\pi}{a_c}, \frac{\pi}{a_c} \right],$$

where

$$a_c = \frac{a}{d} = \frac{a_m}{d_m}.$$

This takes into account that although the fluid and porous regions have different length scales, once redimensionalised, both regions may be represented by a single plan-form.

We seek a stream function $\psi(x,z)$ satisfying

$$-\psi_{,x} = w, \qquad \psi_{,z} = u \qquad \text{for} \qquad z \in [0,d],$$
$$-\psi_{,x} = w^m, \qquad \psi_{,z} = u^m \qquad \text{for} \qquad z \in [-d_m,0),$$

where $x \in [-\pi/a_c, \pi/a_c]$ and

$$w\left(\pm\frac{\pi}{2a_c},z\right) = w^m\left(\pm\frac{\pi}{2a_c},z\right) = w(x,d) = w^m(x,-d_m) = 0,$$
$$u\left(\pm\frac{\pi}{a_c},z\right) = u^m\left(\pm\frac{\pi}{a_c},z\right) = u(0,z) = u^m(0,z) = 0.$$

Then the normal mode expansion gives,

$$w = W(z)\cos a_c x, \qquad z \in [0,d]\,;$$
$$w^m = W^m(z)\cos a_c x, \qquad z \in [-d_m,0].$$

Hence the stream function is chosen to be

$$\psi(x,z) = \begin{cases} -\frac{1}{a_c}W(z)\sin a_c x, & z \in [0,d], \\ -\frac{1}{a_c}W^m(z)\sin a_c x, & z \in [-d_m,0). \end{cases}$$

The streamlines are given by the lines in the (x,z) plane where $\psi(x,z) \equiv$ constant.

In the remaining figures of this chapter, it is the number of cells in the vertical direction and the width of cells in the horizontal direction that are of interest. Throughout all figures, the porous-fluid interface is at $z = 0$, and the eigenfunctions are all normalised before plotting. Note that only one isotherm graph is presented since the isotherms were found to be not dissimilar to the equivalent streamline graphs.

In figures 2.5-2.9 we highlight the streamline patterns for the situation for which figure 2.3 yields the neutral curves i.e. $\hat{d}$ and δ are held fixed at 0.4 and 0.002, respectively. The lower dashed line marks the interface, $z = 0$, and the upper dashed line, the conduction solution at 4°C. When $T_U = 5$°C (figure 2.5) two convection cells already exist in the vertical direction, and are almost exclusively confined to the fluid. The evidence of a second cell in the fluid indicates that penetrative convection is already occurring. It must be remembered that water has a density maximum at approximately 4°C. Therefore, since the temperature at the interface, $T_0 = 3.18$°C, there is an unstable layer between the porous interface and the conduction solution at 4°C. It is only in this layer and the

saturated medium below that instability can be initiated. When convection commences, the (stable) fluid above is brought into motion and a second cell forms. As T_U is increased to 5.3°C (figure 2.6), the convective motion begins to penetrate into the porous medium, and a third cell is seen in the fluid. Since the upper temperature has increased, T_0 has increased as well (3.37°C), and the depth of the layer between the 4°C line and the interface is smaller than that seen in figure 2.5. Thus a third cell is formed since the (stable) fluid above adjusts itself accordingly to accommodate the smaller (unstable) depth. Once T_U reaches 5.4°C (figure 2.7) the convection pattern changes to much wider cells (the bi-modal effect cf. figure 2.3). In fact, we see one cell wholly in the fluid and one cell spanning the fluid and porous medium with circulation in each media. By the time $T_U = 5.8$°C (figure 2.8), again we have one large cell in the fluid and one cell in which the fluid is circulating between the lower part of the fluid layer and the whole of the porous medium. Upon increasing T_U further to 6°C (figure 2.9) the structure of figure 2.8 is maintained in the porous-fluid region, but now a third cell has formed at the top of the fluid layer. Again this is due to the fact that the unstable layer in the fluid is of smaller depth than that seen in figure 2.8, and the (stable) fluid above has adjusted itself accordingly. Thus the penetrative effect is inducing the formation of further convection cells.

In figures 2.10-2.16 we concentrate on $\hat{d} = 1$, i.e., the fluid and porous medium depths are the same, and fix $\delta = 0.002$. Figure 2.10 shows the streamlines when $T_U = 8$°C while figure 2.11 shows the equivalent isotherms. Observe that there are six vertical convection cells with little movement in the porous medium. Figure 2.12 displays the streamlines for $T_U = 8.1$°C. Observe that now there are seven vertical convection cells in this case and again little movement in the porous medium. Figure 2.13 displays the streamlines for $T_U = 8.2375$°C, and in this case we see eight vertical convection cells and yet again little movement in the porous medium. The increase in the number of cells with an increase of T_U is due to the penetrative effect as previously explained. As T_U increases, the depth of the unstable layer decreases and the fluid adjusts itself, forming a layered convection cell structure which is stable for a given upper temperature.

Figures 2.14, 2.15 and 2.16 show what happens to the streamlines when T_U is increased further to 8.25°C, 8.4°C and 9.6°C respectively. There is a switch from con-

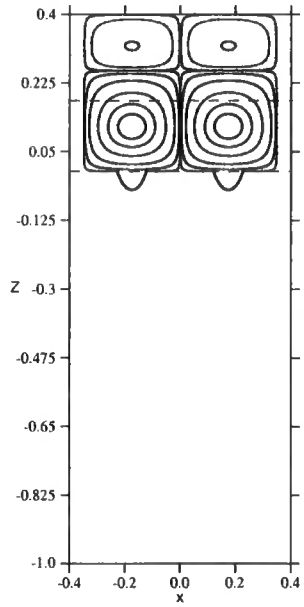

Figure 2.5: Streamline plot, $T_U = 5°C$, $T_0 = 3.18°C$, $Ra_m = 2.458$, $a_m = 9$, $\hat{d} = 0.4$, $\delta = 0.002$.

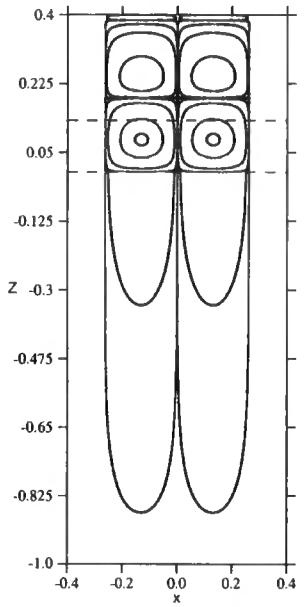

Figure 2.6: Streamline plot, $T_U = 5.3°C$, $T_0 = 3.37°C$, $Ra_m = 11.331$, $a_m = 12$, $\hat{d} = 0.4$, $\delta = 0.002$.

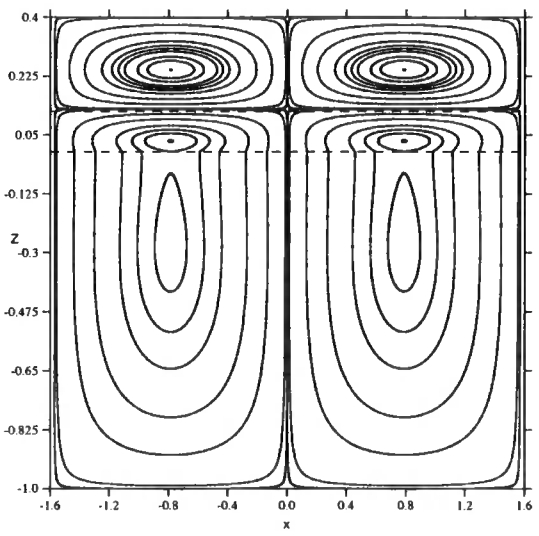

Figure 2.7: Streamline plot, $T_U = 5.4°C$, $T_0 = 3.4°C$, $Ra_m = 15.042$, $a_m = 2$, $\hat{d} = 0.4$, $\delta = 0.002$.

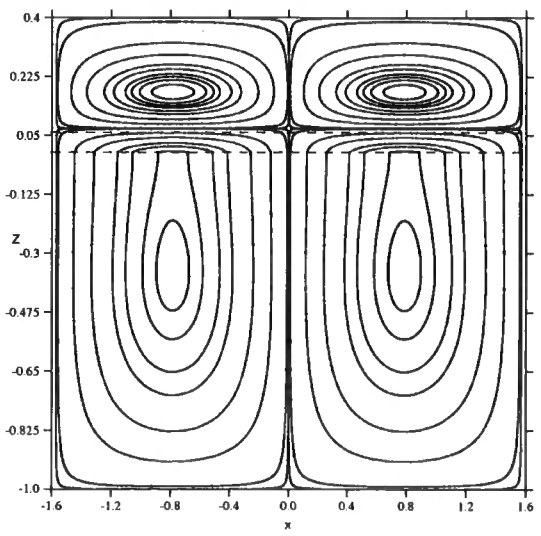

Figure 2.8: Streamline plot, $T_U = 5.8°C$, $T_0 = 3.69°C$, $Ra_m = 19.620$, $a_m = 2$, $\hat{d} = 0.4$, $\delta = 0.002$.

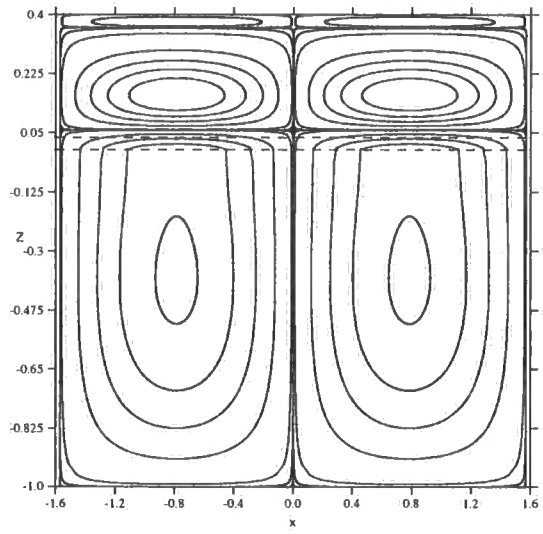

Figure 2.9: Streamline plot, $T_U = 6°C$, $T_0 = 3.8°C$, $Ra_m = 21.833$, $a_m = 2$, $\hat{d} = 0.4$, $\delta = 0.002$.

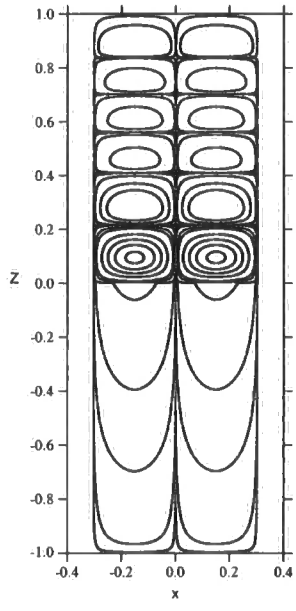

Figure 2.10: Streamline plot, $T_U = 8°C$, $T_0 = 3.29°C$, $Ra_m = 5.723$, $a_m = 10.4$, $\hat{d} = 1$, $\delta = 0.002$.

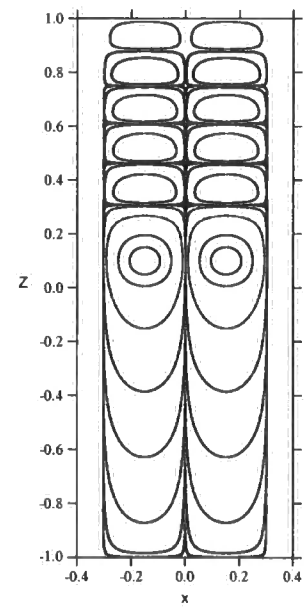

Figure 2.11: Isotherm, $T_U = 8°C$, $T_0 = 3.29°C$, $Ra_m = 5.723$, $a_m = 10.4$, $\hat{d} = 1$, $\delta = 0.002$.

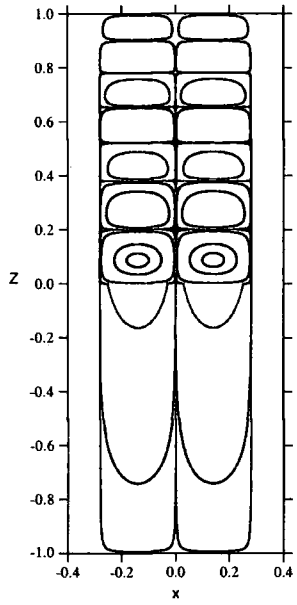

Figure 2.12: Streamline plot, $T_U = 8.1°C$, $T_0 = 3.3°C$, $Ra_m = 8.065$, $a_m = 11.2$, $\hat{d} = 1$, $\delta = 0.002$.

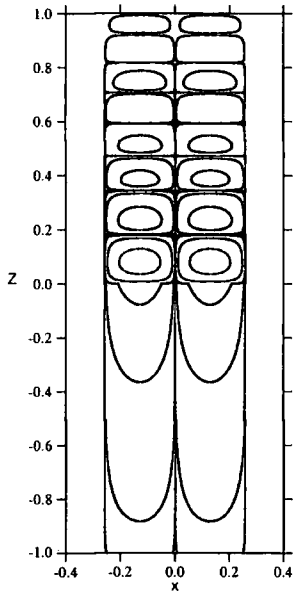

Figure 2.13: Streamline plot, $T_U = 8.2375°C$, $T_0 = 3.39°C$, $Ra_m = 13.296$, $a_m = 12.2$, $\hat{d} = 1$, $\delta = 0.002$.

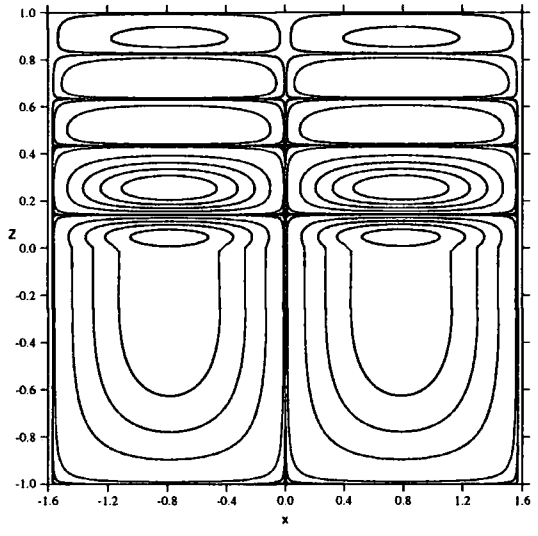

Figure 2.14: Streamline plot, $T_U = 8.25°C$, $T_0 = 3.4°C$, $Ra_m = 13.875$, $a_m = 2$, $\hat{d} = 1$, $\delta = 0.002$.

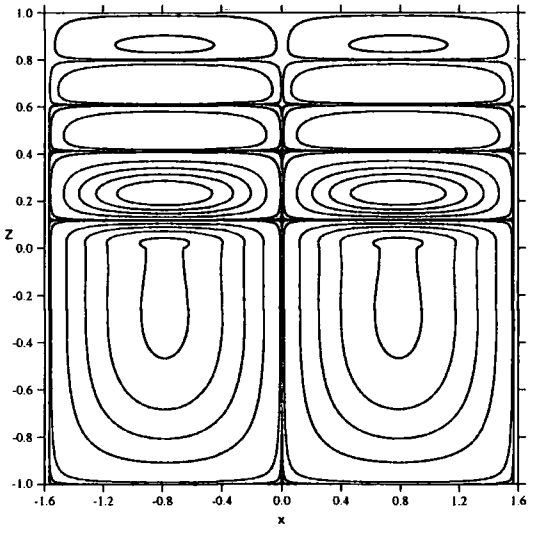

Figure 2.15: Streamline plot, $T_U = 8.4°C$, $T_0 = 3.46°C$, $Ra_m = 15.258$, $a_m = 2$, $\hat{d} = 1$, $\delta = 0.002$.

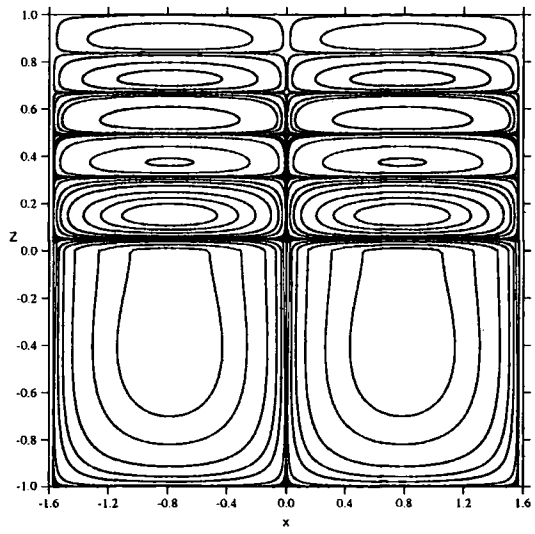

Figure 2.16: Streamline plot, $T_U = 9.6°C$, $T_0 = 3.95°C$, $Ra_m = 24.503$, $a_m = 2$, $\hat{d} = 1$, $\delta = 0.002$.

vection dominated by the fluid to that dominated by the porous medium between $T_U = 8.2375°C$ and $8.25°C$. In figures 2.14-2.16 the porous medium has clearly begun to influence the convection and much wider cells are seen. Since the cells are wider, less form in the vertical direction. Indeed in figures 2.14 and 2.15 we see one cell spanning the porous-fluid region with four further cells in the fluid. By the time the upper temperature is increased to $T_U = 9.6°C$ (figure 2.16), one cell still spans the porous-fluid region but now a further five cells are observed in the fluid. Again this is due to the fact that the unstable layer in the fluid is of smaller depth to that seen in figure 2.15 and the (stable) fluid above has adjusted itself accordingly.

In figures 2.17-2.20 the highly sensitive nature of the streamline structure is illustrated further. We fix $\hat{d} = 2$ and present both the streamlines and corresponding eigenfunctions for $T_U = 13°C$ and $13.2°C$. From observing the eigenfunction with the naked eye it is not immediately evident what the corresponding cellular structure looks like, hence a streamline plot is necessary and it is essential to employ a highly accurate numerical technique to detect such fine detail. It would appear that for $T_U = 13°C$ we find 21 cells in the vertical direction, in the fluid. Whereas for $T_U = 13.2°C$ the porous medium influences the convection pattern to yield wider cells, with one cell spanning the porous medium and fluid and a further 15 cells in the fluid above.

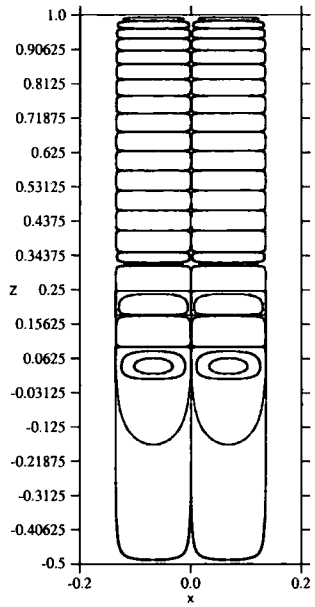

Figure 2.17: Streamline plot, $T_U = 13°C$, $T_0 = 3.37°C$, $Ra_m = 10.470$, $a_m = 11.6$, $\hat{d} = 2$, $\delta = 0.002$.

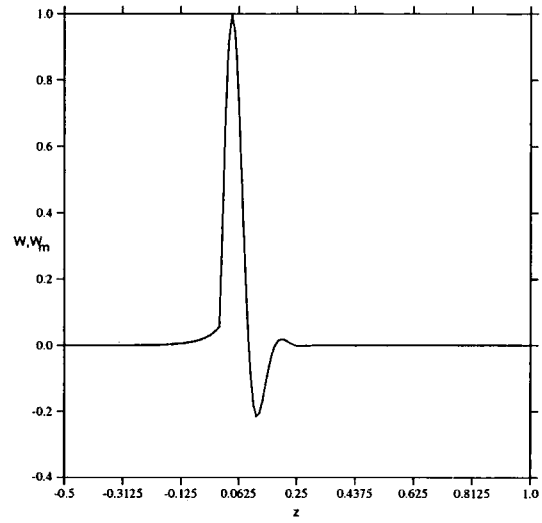

Figure 2.18: W eigenfunction, $T_U = 13°C$, $T_0 = 3.37°C$, $Ra_m = 10.470$, $a_m = 11.6$, $\hat{d} = 2$, $\delta = 0.002$.

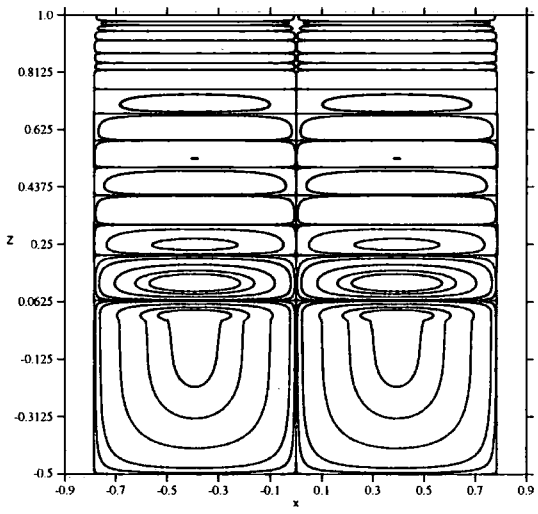

Figure 2.19: Streamline plot, $T_U = 13.2°C$, $T_0 = 3.42°C$, $Ra_m = 13.686$, $a_m = 2$, $\hat{d} = 2$, $\delta = 0.002$.

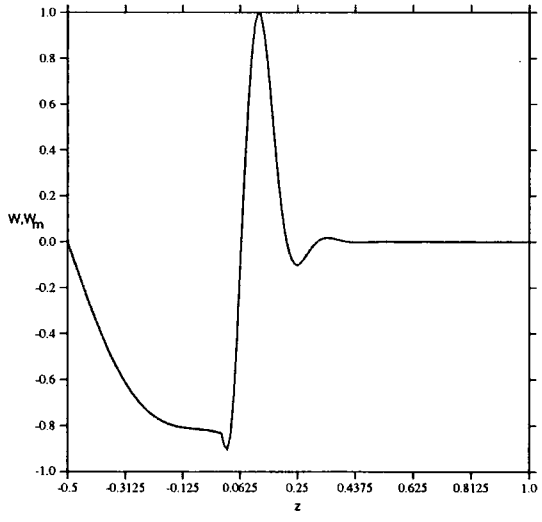

Figure 2.20: W eigenfunction, $T_U = 13.2°C$, $T_0 = 3.42°C$, $Ra_m = 13.686$, $a_m = 2$, $\hat{d} = 2$, $\delta = 0.002$.

Computing complex streamlines like those illustrated above can be quite time consuming. If we wish to simply count the number of convection cells without computing the streamlines then a quick alternative is to closely inspect the eigenfunction. Every sign change in the eigenfunction represents a cell in the system. To ensure that all sign changes are seen the eigenfunction must be computed at a sufficiently large number of points. The eigenfunction at the critical Rayleigh number and wave number for $T_U \approx T_U^{sw}$, was computed at 5000 points and inspected to construct table 2.2.

$\hat{d}$	$T_U \lessapprox T_U^{sw}$ (Fluid dominant)	$T_U \gtrapprox T_U^{sw}$ (Porous dominant)
2.00	21	16
1.80	21	11
1.60	20	10
1.40	17	8
1.20	13	6
1.00	8	5
0.50	3	3
0.40	3	2
0.30	2	2
0.20	1	1
0.18	1	1
0.16	1	1
0.14	1	1

Table 2.2: The number of convection cells in the two layer system, $\hat{d}$ varying, $\delta = 0.002$, $T_U \approx T_U^{sw}$.

Table 2.2 illustrates how many cells are present just before and just after there is a switch in dominance. Observe that as $\hat{d}$ increases the number of convection cells increases too. For $\hat{d}$ suitably large ($\geqslant 1$) there are more cells present when the fluid dominates the convection than there are when the porous medium does. This is to be expected since the cells are wider when the porous medium dominates convection.

2.7.3 Effect of permeability

It has already been shown in figures 2.5-2.19, that the porous medium has a strong effect on the streamline patterns as T_U is varied. We now fix $\hat{d} = 1$ and $T_U = 8.2°\text{C}$ and vary the permeability. In practice, a value of permeability often gives rise to $\delta = \sqrt{K}/d_m = \text{O}(0.002)$, cf. Straughan [93], and so the findings of figures 2.5-2.19 are expected to be representative. However, we feel it worthwhile to compute directly the effect of varying K. Values of $\delta = 2 \times 10^{-3}, 3 \times 10^{-3}$ and 10^{-2} are used to generate figures 2.21, 2.22 and 2.23. Clearly, a striking difference is noticed. When $\delta = 2 \times 10^{-3}$ there are eight cells in the fluid region with hardly any movement in the porous medium. When δ is increased to 3×10^{-3} the higher permeability induces motion in the porous medium and the total number of cells decreases to five with a much wider cell structure being observed. On increasing δ further to 10^{-2} only three cells are observed and the increased permeability allows the porous medium to play a stronger role in the convection process.

2.8 Concluding Remark

Straughan [93] argued that there is a need for additional experiments to measure the coefficient α in the boundary condition (2.4.5). If one wishes to model convection in porous-fluid systems which occur in real life for example, patterned ground formation under water (cf. Krantz *et al.* [44], McKay & Straughan [53]) or fast sea ice melting in the Arctic shelf (cf. Bogorodskii & Nagurnyi [9]), then our calculations indicate that since penetrative convection coupled with a porous-fluid layer system is so sensitive, there is a need for much more accurate experimental data in this area also.

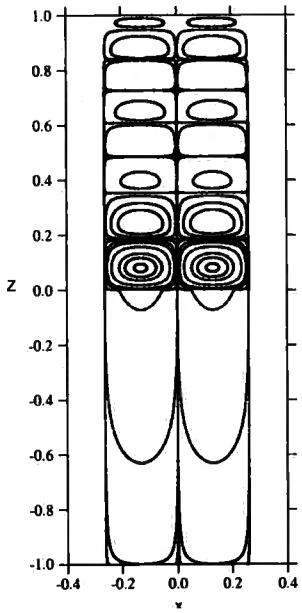

Figure 2.21: Streamline plot, $T_U = 8.2°C$, $T_0 = 3.38°C$, $Ra_m = 11.561$, $a_m = 12$, $\hat{d} = 1$, $\delta = 0.002$.

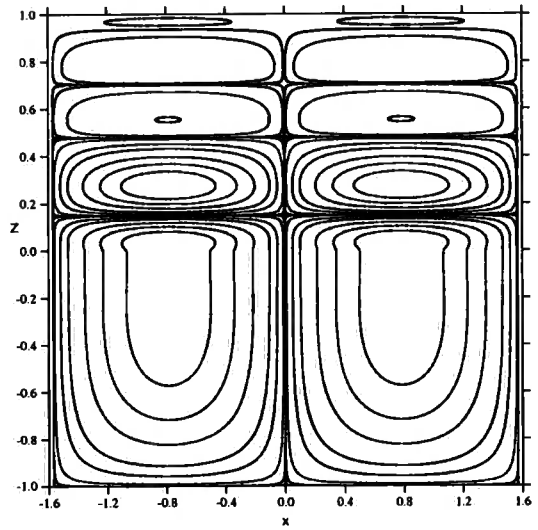

Figure 2.22: Streamline plot, $T_U = 8.2°C$, $T_0 = 3.38°C$, $Ra_m = 13.614$, $a_m = 2$, $\hat{d} = 1$, $\delta = 0.003$.

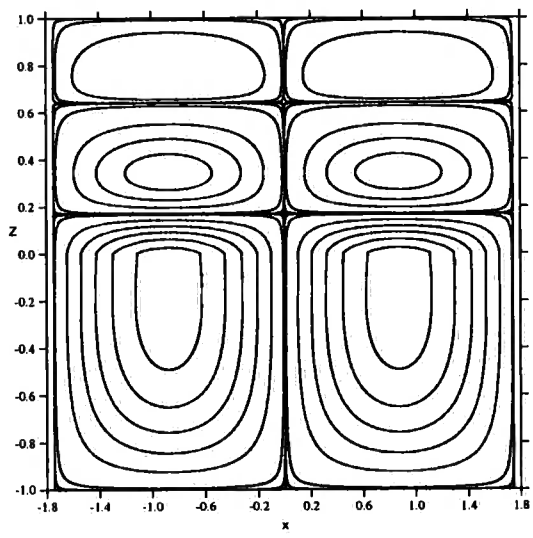

Figure 2.23: Streamline plot, $T_U = 8.2°C$, $T_0 = 3.38°C$, $Ra_m = 13.331$, $a_m = 1.8$, $\hat{d} = 1$, $\delta = 0.01$.

Chapter 3

Penetrative Convection in a Superposed Porous-Fluid Layer via Internal Heating

The purpose of this chapter is to provide an alternative model to that given in chapter 2. In this instance we concentrate on the superposed two layer system but model penetrative convection via internal heating as opposed to a quadratic equation of state. An internal heat source (or sink) can give rise to a situation where one part of a layer is naturally convecting while the other wishes to remain stable. Hence a heat source (sink) is capable of inducing penetrative convection. Many references to work in which convection is described via internal heating can be found in Straughan [91]. One of the most significant contributions, from which great advancement has been made, is that of Roberts [83]. Roberts modelled convection in a horizontal layer of fluid cooled from above, thermally insulated from below and heated uniformly by an internal source. Matthews [60], motivated by convection in an ice covered lake subject to solar radiation, presented a model for the onset of penetrative convection in a fluid layer via internal heating. Matthews employed a cubic temperature profile maintained by a linear internal heat source. Similarly penetrative convection in a porous layer can be described by internal heating, see for example Straughan & Walker [96] and chapter 4. Applications of penetrative convection via internal heating include convection within the Earth's mantle, cf. McKenzie *et al.* [54], cumulus convection, cf. Krishnamurti [45] and Larson [46,47], and convection of stellar

and planetary interiors and atmospheres, cf. Ghosal & Spiegel [34], Schubert *et al.* [88], and Zhang & Schubert [107, 108]. In this chapter, penetrative convection in the coupled porous-fluid system is dealt with via internal heating in both layers. We believe this is the first time penetrative convection in such a system has been modelled this way.

It is found that the instability of the two layer system and the size of the ensuing convection cells are very sensitive to change in the strength of the heat sinks. The sink in the fluid is shown to have a destabilising effect on the system whereas that in the porous can be stabilising or destabilising depending on the form of the steady state temperature profile and the strength of the sink in the fluid layer. A strong interplay between the two sinks is clearly seen and discussed in detail in section 3.5. A selection of streamlines are presented which exhibit novel behaviour when the strength of the sinks are varied.

It is shown that the linearised forms of the model presented here and that given in chapter 2 are mathematically adjoint in some instance. When this is the case it is found that the two models yield the same critical instability thresholds. Hence the results given here confirm the validity of those in chapter 2. However it is also shown that when the two models are adjoint the corresponding eigenfunctions are not the same. From a physical point of view the two models under consideration are very different and we stress this fact. Further discussion of this can be found in section 3.6 and a similar result is encountered in chapter 4 where the effect of penetrative convection on an anisotropic porous medium is investigated by internal heating and a quadratic equation of state.

An outline of this chapter is as follows. In the first two sections the governing system and corresponding equations are described and the non-dimensional perturbation equations derived. The boundary conditions are then discussed and a linear instability analysis is given. A brief description of the numerical method is then provided. An analytical and numerical discussion of the effect of the heat sinks on the stability of the system is presented next. A comparison is then made between the model presented here and that given in chapter 2. The two are shown to be mathematically adjoint in some instance and the eigenvalues and corresponding eigenfunctions are computed and discussed in this case. Finally a further array of streamlines are presented which show that contrary to intuition, the initiating convection cell is not necessarily the strongest one.

3.1 Governing Equations

Consider a fluid occupying the three dimensional layer $\{(x,y) \in \mathbb{R}^2\} \times \{z \in (0,d)\}$ saturating a porous medium superposed below $\{(x,y) \in \mathbb{R}^2\} \times \{z \in (-d_m, 0)\}$. The interface between the saturated porous medium and the fluid is at $z = 0$, see figure 2.1. Suppose the density has a linear temperature dependence of the form

$$\rho = \rho_0\big[1 - \bar{\alpha}(T - T_r)\big], \tag{3.1.1}$$

where ρ, T, and $\bar{\alpha}$ are density, temperature, and thermal expansion coefficient respectively, and ρ_0 and T_r are constant reference values. Then the governing equations for the fluid can be expressed by the Navier-Stokes equations, with a Boussinesq approximation,

$$\begin{aligned}
&\frac{\partial v_i}{\partial t} + v_j\frac{\partial v_i}{\partial x_j} = -\frac{1}{\rho_0}\frac{\partial p}{\partial x_i} + \nu\Delta v_i + \bar{\alpha}gTk_i,\\
&\frac{\partial v_i}{\partial x_i} = 0,\\
&\frac{\partial T}{\partial t} + v_i\frac{\partial T}{\partial x_i} = \frac{k_f}{(\rho_0 c_p)_f}\Delta T + 2Q.
\end{aligned} \tag{3.1.2}$$

Equations $(3.1.2)_2$ and $(3.1.2)_3$ are the incompressibility condition and balance of energy, respectively. The Q term in the energy equation $(3.1.2)_3$ is some (constant) internal heat source or sink and it's inclusion allows the model to describe penetrative convection in the fluid layer (see section 3.5). Equations (3.1.2) are assumed to hold for time $t > 0$, in the spatial domain $\{(x,y) \in \mathbb{R}^2, z \in (0,d)\}$. In these equations v_i, t, x_i, p, and T are velocity, time, displacement, pressure and temperature, and ν, g, k_f, c_p are kinematic viscosity, gravity, thermal conductivity and specific heat at constant pressure. Standard indicial notation and the Einstein summation convention are employed throughout. Subscript (or superscript) f or m denotes fluid or porous medium, respectively. The symbol Δ is the Laplace operator and $\mathbf{k} = (0,0,1)^T$.

In the porous medium the motion of the fluid is described by Darcy flow with the buoyancy force again given by (3.1.1); therefore

$$\begin{aligned}
&0 = -\frac{1}{\rho_0}\frac{\partial p^m}{\partial x_i} - \frac{\nu}{K}v_i^m + \bar{\alpha}gT_mk_i,\\
&\frac{\partial v_i^m}{\partial x_i} = 0,\\
&\frac{(\rho_0 c_p)^*}{(\rho_0 c_p)_f}\frac{\partial T_m}{\partial t} + v_i^m\frac{\partial T_m}{\partial x_i} = \frac{k^*}{(\rho_0 c_p)_f}\Delta T_m + 2Q^m.
\end{aligned} \tag{3.1.3}$$

These equations hold on $\{(x,y) \in \mathbb{R}^2\} \times \{z \in (-d_m, 0)\} \times \{t > 0\}$, and the variables v_i^m, p_m, T_m are velocity, pressure and temperature in the porous medium. K is the permeability and Q^m is some (constant) internal heat source or sink in the porous layer. Starred quantities are defined in terms of fluid and porous variables as

$$S^* = \phi S_f + (1-\phi) S_m,$$

where ϕ is the porosity and S stands for a physical variable such as thermal conductivity k.

To establish what values of Q yield a source or sink, consider the integral form of the energy balance equation $(3.1.2)_3$, namely,

$$\frac{d}{dt}\int_V T dV + \int_V v_i \frac{\partial T}{\partial x_i} dV = \frac{k_f}{(\rho_0 c_p)_f} \int_V \frac{\partial}{\partial x_i}\left(\frac{\partial T}{\partial x_i}\right) dV + 2\int_V Q dV, \qquad (3.1.4)$$

where V is some periodic cell in the fluid layer $z \in (0,d)$. Using the divergence theorem, (3.1.4) can be rewritten as

$$\frac{d}{dt}\int_V T dV + \oint_{\partial V} n_i v_i T dA = \frac{k_f}{(\rho_0 c_p)_f} \oint_{\partial V} n_i \frac{\partial T}{\partial x_i} dA + 2\int_V Q dV,$$

where n_i is the unit normal to V and ∂V the boundary of V. Note that, in the absence of any heat flux and velocity a positive value of Q will give rise to an increase in temperature of the layer and similarly, a negative value of Q will give rise to a decrease. Hence a positive value of Q represents an internal heat source and a negative value of Q an internal heat sink. An entirely analogous argument applied to $(3.1.3)_3$ reveals that a positive value of Q_m represents an internal heat source in the porous layer and a negative value of Q_m an internal heat sink.

The temperatures on the upper and lower boundaries are held fixed at values T_U ($>$ 0°C) and 0°C respectively. The steady state solution to equations (3.1.2) and (3.1.3), denoted by $(\bar{u}_i, \bar{T}, \bar{p})$, $(\bar{u}_i^m, \bar{T}^m, \bar{p}^m)$, is obtained from

$$\bar{u}_i = 0, \qquad \bar{T}'' = -\frac{2Q}{\lambda}, \qquad 0 \le z \le d, \qquad (3.1.5)$$

$$\bar{u}_i^m = 0, \qquad \bar{T}_m'' = -\frac{2Q_m}{\lambda_m}, \qquad -d_m \le z \le 0, \qquad (3.1.6)$$

where $\lambda = k_f/(\rho_0 c_p)_f$ and $\lambda_m = k^*/(\rho_0 c_p)_f$. The hydrostatic pressures $\bar{p}$ and $\bar{p}^m$ may be found from $(3.1.2)_1$ and $(3.1.3)_1$ respectively, but since $\bar{p}$ and $\bar{p}^m$ are eliminated from

our analysis later on, we do not include a derivation of them here. Integrating $\bar{T}''$ and $\bar{T}_m''$ twice, and imposing the boundary conditions it can be deduced that

$$\bar{T}(z) = -\frac{Qz^2}{\lambda} + \left(\frac{T_U - T_0}{d} + \frac{Qd}{\lambda}\right) z + T_0, \tag{3.1.7}$$

$$\bar{T}^m(z) = -\frac{Q_m z^2}{\lambda_m} + \left(\frac{T_0}{d_m} - \frac{Q_m d_m}{\lambda_m}\right) z + T_0. \tag{3.1.8}$$

The temperature at the interface, T_0, can be found by requiring continuity of temperature at $z = 0$ and continuity of the heat flux, viz.

$$\lambda \frac{d\bar{T}}{dz} = \lambda_m \frac{d\bar{T}_m}{dz} \qquad \text{at} \quad z = 0. \tag{3.1.9}$$

If we define $\epsilon_T = \lambda/\lambda_m$ and $\mathcal{E} = \epsilon_T/(\epsilon_T + \hat{d})$ then from (3.1.9) one obtains the relation,

$$T_0 = \mathcal{E}\left(T_U + \frac{Qd^2}{\lambda} + \frac{Q_m d_m^2 \hat{d}}{\lambda_m \epsilon_T}\right). \tag{3.1.10}$$

3.2 Perturbation Equations

To study the instability of the basic solutions $(3.1.5)_1$, $(3.1.6)_1$, (3.1.7) and (3.1.8), perturbations (u_i, θ, π), (u_i^m, θ_m, π_m) to these solutions are introduced and we set,

$$v_i = \bar{u}_i + u_i, \quad T = \bar{T} + \theta, \quad p = \bar{p} + \pi,$$
$$v_i^m = \bar{u}_i^m + u_i^m, \quad T_m = \bar{T}_m + \theta_m, \quad p_m = \bar{p}_m + \pi_m.$$

The perturbation equations which arise from (3.1.2) and (3.1.3) are,

$$\begin{aligned}
&\frac{\partial u_i}{\partial t} + u_j \frac{\partial u_i}{\partial x_j} = -\frac{1}{\rho_0}\frac{\partial \pi}{\partial x_i} + \nu \Delta u_i + \bar{\alpha} g \theta k_i, \\
&\frac{\partial u_i}{\partial x_i} = 0, \\
&\frac{\partial \theta}{\partial t} + u_i \frac{\partial \theta}{\partial x_i} = \lambda \Delta \theta - w\left[\frac{T_U - T_0}{d} + \frac{Q}{\lambda}(d - 2z)\right],
\end{aligned} \tag{3.2.1}$$

and,

$$\begin{aligned}
&0 = -\frac{1}{\rho_0}\frac{\partial \pi^m}{\partial x_i} - \frac{\nu}{K} u_i^m + \bar{\alpha} g \theta_m k_i, \\
&\frac{\partial u_i^m}{\partial x_i} = 0, \\
&G_m \frac{\partial \theta^m}{\partial t} + u_i^m \frac{\partial \theta^m}{\partial x_i} = \lambda_m \Delta \theta^m - w^m\left[\frac{T_0}{d_m} - \frac{Q_m}{\lambda_m}(d_m + 2z)\right],
\end{aligned} \tag{3.2.2}$$

where $w = u_3$, $w^m = u_3^m$ and $G_m = (\rho_0 c_p)^*/(\rho_0 c_p)_f$.

To non-dimensionalise the above equations the fluid scalings of time, velocity, pressure, and temperature are taken as,

$$\mathcal{T} = \frac{d^2}{\nu}, \qquad U = \frac{\nu}{d}, \qquad P = \frac{\rho_0 \nu U}{d}, \qquad T^{\#} = \frac{U}{\lambda}\sqrt{\frac{-Q\nu d}{g\bar{\alpha}}}.$$

The respective porous scalings are,

$$\mathcal{T}^m = \frac{d_m^2}{\nu}, \qquad U^m = \frac{\nu}{d_m}, \qquad P^m = \frac{\rho_0 \nu U^m}{d_m}, \qquad T^{m\#} = \frac{U_m}{\lambda_m}\sqrt{\frac{-Q_m \nu d_m^3}{g\bar{\alpha}K}}.$$

To ensure that $T^{\#}$, $T^{m\#}$ are real we impose $Q, Q_m < 0$, i.e. we deal explicitly with a heat sink in both layers. The length scales in the fluid and porous domains are d and d_m, respectively. In addition the fluid and porous Rayleigh numbers Ra and Ra_m are defined by

$$Ra = R^2 = \frac{-Qg\bar{\alpha}d^5}{\nu\lambda^2}, \qquad Ra_m = R_m^2 = \frac{-Q_m g\bar{\alpha}K d_m^3}{\nu\lambda_m^2}.$$

The Darcy number is defined to be $\delta = \sqrt{K}/d_m$ and the fluid and porous Prandtl numbers are defined as $Pr = \nu/\lambda$, $Pr^m = \nu/\lambda_m$ respectively.

In terms of the non-dimensional variables, equations (3.2.1) and (3.2.2) become,

$$\begin{aligned} &\frac{\partial u_i}{\partial t} + u_j\frac{\partial u_i}{\partial x_j} = -\frac{\partial \pi}{\partial x_i} + \Delta u_i + R\theta k_i, \\ &\frac{\partial u_i}{\partial x_i} = 0, \\ &Pr\left(\frac{\partial \theta}{\partial t} + u_i\frac{\partial \theta}{\partial x_i}\right) = \Delta\theta + Rf(z)w, \end{aligned} \tag{3.2.3}$$

and,

$$\begin{aligned} &\delta^2\frac{\partial \pi^m}{\partial x_i} = -u_i^m + R^m\theta^m k_i, \\ &\frac{\partial u_i^m}{\partial x_i} = 0, \\ &Pr_m\left(G_m\frac{\partial \theta^m}{\partial t^m} + u_i^m\frac{\partial \theta^m}{\partial x_i}\right) = \Delta\theta^m + R^m f^m(z)w^m, \end{aligned} \tag{3.2.4}$$

where $f(z) = 1 - 2z + (T_U - T_0)\lambda/Qd^2$ and $f^m(z) = T_0\lambda_m/Q_m d_m^2 - 2z - 1$. Equations (3.2.3) hold in the region $\{(x,y) \in \mathbb{R}^2\} \times \{z \in (0,1)\} \times \{t > 0\}$ while (3.2.4) hold on $\{(x,y) \in \mathbb{R}^2\} \times \{z \in (-1,0)\} \times \{t^m > 0\}$. The interface is $z = 0$ while the lower porous surface is now $z = -1$ and $z = 1$ is the (upper) fluid surface.

3.3 Linearised Instability Theory and Boundary Conditions

The obtain linearised perturbation equations all quadratic terms in (3.2.3) and (3.2.4) are discarded. The resulting system is linear so solutions can be sought of the form $u_i = u_i(\mathbf{x})e^{\sigma t}$, $\theta = \theta(\mathbf{x})e^{\sigma t}$, $\pi = \pi(\mathbf{x})e^{\sigma t}$, $u_i^m = u_i^m(\mathbf{x})e^{\sigma t}$, $\theta^m = \theta^m(\mathbf{x})e^{\sigma t}$, and $\pi^m = \pi^m(\mathbf{x})e^{\sigma t}$. This yields an eigenvalue problem for the growth rate σ. The eigenvalues σ_i, are ordered so that $\sigma_1 \geq \sigma_2 \geq \ldots$. If $\sigma_1 > 0$ then instability occurs. The associated eigenfunction $\{u_i^{(1)}, u_i^{m(1)}\}$ yields the streamline curves which are included in sections 3.5.3, 3.5.4, and 3.6, to visualise the flow patterns at the onset of instability.

The time scale $t^m = t/\omega$ is introduced, then (3.2.3) and (3.2.4) yield the linearised perturbation equations

$$\begin{aligned} \sigma u_i &= -\pi_{,i} + \Delta u_i + R\theta k_i, \\ u_{i,i} &= 0, \\ \sigma Pr\theta &= \Delta\theta + Rf(z)w, \end{aligned} \tag{3.3.1}$$

and,

$$\begin{aligned} \delta^2 \pi_{,i}^m &= -u_i^m + R^m \theta^m k_i, \\ u_{i,i}^m &= 0, \\ \sigma\omega Pr_m G_m \theta^m &= \Delta\theta^m + R^m f^m(z) w^m. \end{aligned} \tag{3.3.2}$$

The boundary conditions required for the case where the upper surface is open to the atmosphere (tangential stress free) are, in non-dimensional form,

$$\text{on} \quad z = 1, \qquad \theta = w = w_{,zz} = 0\,; \tag{3.3.3}$$

$$\text{on} \quad z = -1, \qquad \theta^m = w^m = 0. \tag{3.3.4}$$

Continuity of the normal components of velocity, temperature, and heat flux, across the interface $z = 0$, leads to the conditions

$$w^m = \frac{w}{\hat{d}}, \qquad \theta^m = \frac{\delta}{\epsilon_T}\sqrt{\frac{\hat{A}}{\hat{d}}}\,\theta, \qquad \frac{\partial\theta^m}{\partial z} = \delta\sqrt{\frac{\hat{A}}{\hat{d}^3}}\,\frac{\partial\theta}{\partial z}, \tag{3.3.5}$$

where $\hat{d} = d/d_m$ and $\hat{A} = Q/Q_m$. In addition at $z = 0$, continuity of normal stress is required,

$$\hat{d}^2\pi^m = \pi - 2w_{,z}, \tag{3.3.6}$$

and the Beavers-Joseph boundary condition is employed,

$$\frac{\partial u^\beta}{\partial z} = \frac{\hat{d}\alpha}{\delta}(u^\beta - \hat{d}u_m^\beta), \qquad \beta = 1, 2, \tag{3.3.7}$$

where α is a coefficient depending on the fluid and porous medium under consideration.

The pressures π and π^m are eliminated by taking curlcurl of $(3.3.1)_1$ and $(3.3.2)_1$. The third component of the resulting equations is retained to yield

$$\sigma\Delta w = \Delta^2 w + R\Delta^*\theta, \tag{3.3.8}$$

and

$$0 = \Delta w^m - R^m\Delta^*\theta^m. \tag{3.3.9}$$

where Δ^* is the horizontal Laplacian,

$$\Delta^* = \frac{\partial^2}{\partial x^2} + \frac{\partial^2}{\partial y^2}.$$

Next a normal mode representation of w, θ, w^m and θ^m is used in (3.3.8), $(3.3.1)_3$, (3.3.9), and $(3.3.2)_3$ by setting,

$$w = W(z)g(x, y), \qquad \theta = \Theta(z)g(x, y),$$
$$w^m = W^m(z)g^m(x, y), \qquad \theta^m = \Theta^m(z)g^m(x, y),$$

where $g(x, y)$ and $g^m(x, y)$ are horizontal plan forms which satisfy,

$$\Delta^* g = -a^2 g, \qquad \Delta^* g^m = -a_m^2 g^m,$$

where a and a_m are the wave numbers associated with convection cells in the fluid and porous medium, respectively.

The fourth order equation (3.3.8) can be written as two second order equations by regarding $A = (D^2 - a^2)W$ as an independent variable, where $D^2 = d^2/dz^2$. This yields five coupled second order equations to determine the critical growth rate σ, namely,

$$\begin{aligned}
&(D^2 - a^2)W = A, \\
&(D^2 - a^2)A - Ra^2\Theta = \sigma A, \\
&(D^2 - a^2)\Theta + Rf(z)W = \sigma Pr\Theta,
\end{aligned} \tag{3.3.10}$$

$$
\begin{aligned}
&(D^2 - a_m^2)W^m + R^m a_m^2 \Theta^m = 0, \\
&(D^2 - a_m^2)\Theta^m + R^m f^m(z) W^m = \sigma\omega Pr_m G_m \Theta^m,
\end{aligned}
\tag{3.3.11}
$$

where (3.3.10) hold on $z \in (0,1)$ while (3.3.11) hold on $z \in (-1,0)$. Coupling is through the boundary conditions.

The boundary conditions (3.3.3)-(3.3.7) are reduced to yield,

$$\Theta = W = A = 0, \qquad \text{on} \quad z = 1, \tag{3.3.12}$$

$$\Theta^m = W^m = 0, \qquad \text{on} \quad z = -1, \tag{3.3.13}$$

and,

$$
\begin{aligned}
&W = \hat{d} W^m, \qquad \Theta^m = \frac{\delta}{\epsilon_T}\sqrt{\frac{\hat{A}}{\hat{d}}}\,\Theta, \qquad D\Theta^m = \delta\sqrt{\frac{\hat{A}}{\hat{d}^3}}\,D\Theta, \\
&2a^2 DW - DA - \frac{\hat{d}^2}{\delta^2} DW^m = -\sigma DW, \\
&a^2 W + A = \frac{\hat{d}\alpha}{\delta}(DW - \hat{d}\, DW^m), \qquad \text{on} \quad z = 0.
\end{aligned}
\tag{3.3.14}
$$

Hence, our goal is to solve (3.3.10) and (3.3.11) subject to the boundary conditions (3.3.12)-(3.3.14). Before describing the numerical method we note the useful relations,

$$\omega = \frac{\mathcal{T}}{\mathcal{T}_m} = \hat{d}^2, \qquad Pr_m = \epsilon_T Pr, \qquad Ra = \frac{\hat{A}\hat{d}^5}{\epsilon_T^2 \delta^2} Ra_m.$$

3.4 The Chebyshev tau D^2 Method

To solve the eigenvalue problem (3.3.10)-(3.3.14) the Chebyshev tau D^2 method was employed. It was implemented in an entirely analogous fashion to that described in section 2.5.1. The five quantities W, A, Θ, W_m and Θ_m are regarded as independent variables and expanded as Chebyshev series, i.e.

$$
\begin{aligned}
&W = \sum_{n=0}^{N+2} W_n T_n(z), \qquad A = \sum_{n=0}^{N+2} A_n T_n(z), \qquad \Theta = \sum_{n=0}^{N+2} \Theta_n T_n(z), \\
&W_m = \sum_{n=0}^{N+2} W_n^m T_n(z), \qquad \Theta^m = \sum_{n=0}^{N+2} \Theta_n^m T_n(z).
\end{aligned}
$$

Equations (3.3.10), (3.3.11), and the operator D^2 are then written in matrix form cf. Dongarra *et al.* [23] and chapter 2. The boundary conditions (3.3.12)-(3.3.14) are imposed by

removing the $m(N+2)$ and $m(N+3)$ rows of the resulting matrix, $m = 1, \ldots, 5$, and replacing them by the discrete forms of the boundary conditions. The boundary conditions were realised with the aid of the relations $T_n(\pm 1) = (\pm 1)^n$ and $T_n'(\pm 1) = (\pm 1)^{n-1} n^2$. This results in a generalised $5(N+3) \times 5(N+3)$ matrix eigenvalue problem of the form

$$A\mathbf{x} = \sigma B\mathbf{x}.$$

This was solved for the eigenvalues $\sigma^{(n)}$, $n = 1, 2, \ldots$, and the eigenfunctions $\mathbf{x}^{(n)}$ with the aid of the QZ algorithm which we employed via the NAG routine F02BJF as before.

3.5 Discussion of the Model and Numerical Results

Recall from section 3.1 that the steady state temperature profiles in the fluid and porous layers, and the temperature at the interface are given by

$$\bar{T}(z) = -\frac{Qz^2}{\lambda} + \left(\frac{T_U - T_0}{d} + \frac{Qd}{\lambda}\right) z + T_0, \tag{3.5.1}$$

$$\bar{T}^m(z) = -\frac{Q_m z^2}{\lambda_m} + \left(\frac{T_0}{d_m} - \frac{Q_m d_m}{\lambda_m}\right) z + T_0, \tag{3.5.2}$$

$$T_0 = \mathcal{E}\left(T_U + \frac{Qd^2}{\lambda} + \frac{Q_m d_m^2 \hat{d}}{\lambda_m \epsilon_T}\right). \tag{3.5.3}$$

Differentiating (3.5.1) and (3.5.2) yields the turning points for $\bar{T}$ and $\bar{T}^m$,

$$z_{tp} = \frac{d}{2}\left[(T_U - T_0)\hat{\epsilon} + 1\right], \qquad z_{tp}^m = \frac{d_m}{2}\left[T_0 \hat{\epsilon}_m - 1\right], \tag{3.5.4}$$

where $\hat{\epsilon} = \lambda/Qd^2$ and $\hat{\epsilon}_m = \lambda_m/Q_m d_m^2$. Since $Q, Q_m < 0$ the turning points are both minimum points ($\bar{T}'', \bar{T}_m'' > 0$). To investigate what type of steady state temperature

profile can be obtained we begin by using (3.5.3) and (3.5.4) to derive the identities,

$$z_{tp} > 0 \quad \Leftrightarrow \quad T_U < -\frac{1}{\hat{\epsilon}} + \frac{1}{\hat{\epsilon}_m}, \tag{3.5.5}$$

$$z_{tp} < 0 \quad \Leftrightarrow \quad T_U > -\frac{1}{\hat{\epsilon}} + \frac{1}{\hat{\epsilon}_m}, \tag{3.5.6}$$

$$z^m_{tp} > -d_m \quad \Leftrightarrow \quad T_U < -\frac{1}{\hat{\epsilon}} - \frac{1}{\hat{\epsilon}_m}\left(\frac{2\hat{d}}{\epsilon_T} + 1\right), \tag{3.5.7}$$

$$z^m_{tp} < -d_m \quad \Leftrightarrow \quad T_U > -\frac{1}{\hat{\epsilon}} - \frac{1}{\hat{\epsilon}_m}\left(\frac{2\hat{d}}{\epsilon_T} + 1\right), \tag{3.5.8}$$

$$T_0 > 0 \quad \Leftrightarrow \quad T_U > -\frac{1}{\hat{\epsilon}} - \frac{1}{\hat{\epsilon}_m}\frac{\hat{d}}{\epsilon_T}, \tag{3.5.9}$$

$$T_0 < 0 \quad \Leftrightarrow \quad T_U < -\frac{1}{\hat{\epsilon}} - \frac{1}{\hat{\epsilon}_m}\frac{\hat{d}}{\epsilon_T}. \tag{3.5.10}$$

Equations (3.5.5), (3.5.3) and $(3.5.4)_2$ can be used to derive the relation

$$z_{tp} > 0 \quad \Leftrightarrow \quad z^m_{tp} > 0 \quad \Rightarrow \quad T_0 < 0.$$

Similarly (3.5.6), (3.5.3) and $(3.5.4)_2$ yield

$$z_{tp} < 0 \quad \Leftrightarrow \quad z^m_{tp} < 0 \quad \Leftrightarrow \quad T_0 > \frac{1}{\hat{\epsilon}_m}.$$

Hence only the following 4 types of steady state temperature profile are possible.

Case 1: The whole system is stable.

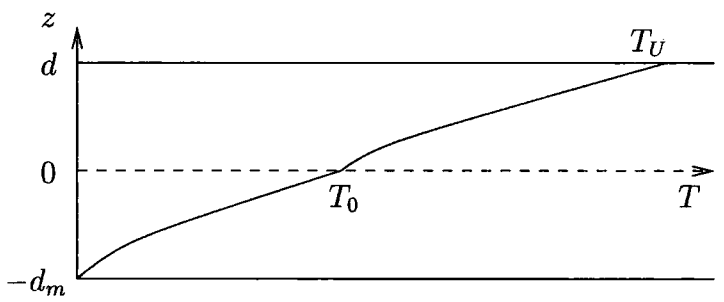

Figure 3.1: Steady state temperature profile, depth z against temperature T. $z_{tp} < 0$, $z^m_{tp} < -d_m$.

If $z^m_{tp} < -d_m$, then (3.5.8) implies that $T_0 > 0$ and $z_{tp} < 0$, and a profile like that displayed in figure 3.1 is obtained. Recall that density is a linearly, decreasing function of temperature (see (3.1.1)) i.e., the warmer the fluid the lighter it is. Hence for the profile

given in figure 3.1 the system is always stable.

Case 2: There is an unstable region in the porous layer, $T_0 > 0$.

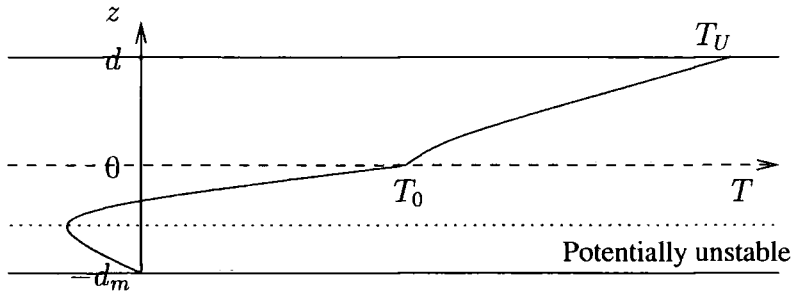

Figure 3.2: Steady state temperature profile, depth z against temperature T, $z_{tp} < 0$, $-d_m < z_{tp}^m < 0, T_0 > 0$.

The profile given in figure 3.2 can be obtained by imposing (3.5.7) and (3.5.9) (note (3.5.6) follows automatically). Fluid at the turning point z_{tp}^m, is colder and hence heavier than that at the base $z = -d_m$. Therefore there is a potentially unstable region between the turning point and the base of the porous layer.

Case 3: There is an unstable region in the porous layer, $T_0 < 0$.

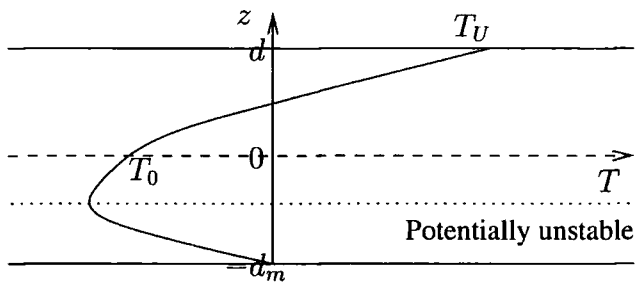

Figure 3.3: Steady state temperature profile, depth z against temperature T. $z_{tp} < 0$, $-d_m < z_{tp}^m < 0, T_0 < 0$.

The profile given in figure 3.3 can be obtained by imposing (3.5.6) and (3.5.10) (note (3.5.7) follows automatically). Again there is a potentially unstable layer between the turning point and the base since the fluid at the turning point is colder and heavier than that at $z = -d_m$.

Case 4: There is an unstable region in the fluid and underlying porous layer, $T_0 < 0$.

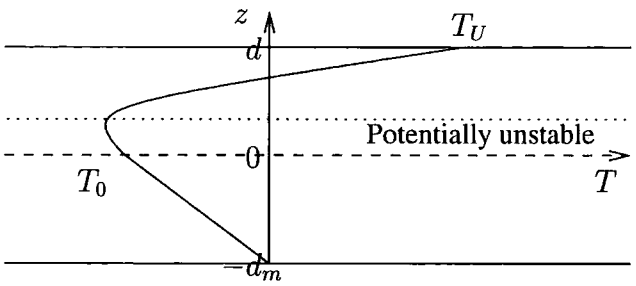

Figure 3.4: Steady state temperature profile, depth z against temperature T, $z_{tp} > 0$, $z_{tp}^m > 0$, $T_0 < 0$.

If $z_{tp} > 0$ then (3.5.5) implies that $T_0 < 0$ and $z_{tp}^m > 0$, and a profile like that displayed in figure 3.4 is obtained. Fluid at the turning point z_{tp}, is heavier than that below and hence there is a potentially unstable layer in the lower fluid region and underlying porous medium (everywhere beneath the dotted line).

From the four cases presented above it is clear that penetrative convection is possible in cases 2, 3, and 4. Hence it is these cases that are of interest in the following analysis. It is evident from the steady state temperature profiles that the position of the turning point determines the stability characteristics of the system. To investigate what effect Q and Q_m have on the system we assume that d, d_m, λ, λ_m and ϵ_T are all fixed. Then $\hat{\epsilon} \propto 1/Q$ and $\hat{\epsilon}_m \propto 1/Q_m$, and we consider what effect $\hat{\epsilon}$ and $\hat{\epsilon}_m$ have on the turning points z_{tp}, z_{tp}^m.

3.5.1 Stability characteristics of Q

Eliminating T_0, (3.5.4) can be rewritten as

$$z_{tp} = \frac{d(1-\mathcal{E})}{2}\left[\hat{\epsilon}\left(T_U - \frac{1}{\hat{\epsilon}_m}\right) + 1\right], \tag{3.5.11}$$

$$z_{tp}^m = \frac{d_m\mathcal{E}}{2}\left[\hat{\epsilon}_m\left(T_U + \frac{1}{\hat{\epsilon}}\right) - 1\right]. \tag{3.5.12}$$

By inspection of (3.5.11) it can be seen that as $\hat{\epsilon}$ gets less negative, z_{tp} increases for fixed $\hat{\epsilon}_m$. In other words as the heat sink Q gets stronger the system becomes more unstable. Similarly by inspection of (3.5.12), as $\hat{\epsilon}$ gets less negative, z_{tp}^m increases for fixed $\hat{\epsilon}_m$ ($\hat{\epsilon}_m/\hat{\epsilon}$ gets more positive). So again as Q gets stronger, the system becomes more unstable.

Hence Q is destabilising in cases 2, 3, and 4, i.e. the stronger the heat sink in the fluid layer the more unstable the system. Physically this makes sense in all three cases.

Consider case 2, fluid at the interface is warmer and lighter than that at the bottom of the porous medium. The lighter the fluid at the interface, the more stable the system. If the heat sink in the fluid is made stronger, the temperature at the interface will decrease and the fluid there will become colder. Hence the heat sink is destabilising in this instance. In case 3, fluid at the interface is colder (and hence heavier) than that at the base of the porous medium. Therefore if the heat sink in the fluid layer is made stronger, the temperature at the interface decreases and the difference between the fluid density at the interface and that at the base of the porous medium increases. Since the fluid at the interface is heavier than that at the base this is clearly destabilising. In case 4, fluid at the interface is heavier than that at the top of the fluid layer. Therefore the whole of the fluid layer is potentially stable. However if there is fluid within the layer that is colder than that at the interface then there is a potentially unstable layer between the interface and the colder fluid. The stronger the heat sink in the fluid, the more likely this is (for fixed Q_m). Hence a heat sink in the fluid is destabilising in this instance also.

To be in keeping with chapter 2, we suppose that the saturating fluid is water and unless otherwise stated take, $Pr = 6$, $\epsilon_T = 0.7$, $G_m = 10$, $\alpha = 0.1$ and $\delta = 0.002$. In figure 3.5 the neutral curves for $T_U, \hat{d}$ and $\hat{\epsilon}_m$ fixed at $9°\mathrm{C}, 1$ and -0.0728 respectively, with $\hat{\epsilon}$ varying are presented. As $\hat{\epsilon}$ becomes less negative (Q becomes stronger) the neutral curves shift down and the system becomes more unstable. This is expected and in agreement with the analytical work presented above. Q clearly has a destabilising effect. Moreover, the neutral curves exhibit a bimodal nature like that first seen in Chen & Chen [17]. For $\hat{\epsilon} = -0.05, -0.0275$ the minimum of the curve occurs at $a_m \approx 2$ whereas for $\hat{\epsilon} = -0.025, -0.015$, $a_m \approx 12, 8.5$, respectively. Therefore as $\hat{\epsilon}$ becomes less negative the shape of the convection cells switches from wide (smaller a_m) to narrow (larger a_m). Hence, as Q gets stronger convection switches from porous to fluid dominated. So not only does Q dramatically effect the onset of convection it also effects the nature of the ensuing convection cells. To illustrate this more clearly consider the corresponding streamlines presented in the next section.

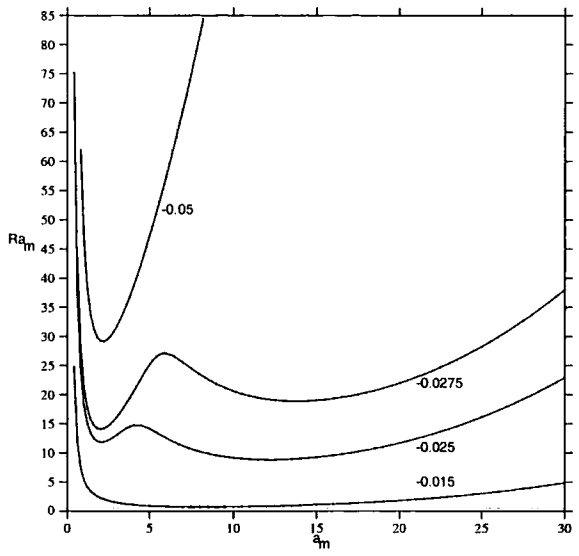

Figure 3.5: Neutral instability curves, Ra_m against a_m. $T_U = 9°\text{C}$, $\hat{d} = 1$, $\hat{\epsilon}_m = -0.0728$, $\hat{\epsilon}$ varies as shown on graph.

3.5.2 Variation of the streamlines with Q

In this section the streamlines at criticality, corresponding to figure 3.5 are presented i.e. T_U, $\hat{d}$ and $\hat{\epsilon}_m$ are fixed at $9°\text{C}, 1$ and -0.0728 respectively, and $\hat{\epsilon}$ is varied from -0.05 to -0.015. Throughout all figures the porous-fluid interface is at $z = 0$, and the dashed line marks the turning point of the steady state solution. Everywhere below the dashed line is potentially unstable and everywhere above it is stable.

When $\hat{\epsilon} = -0.05$ (figure 3.6) there is one cell bridging the porous-fluid interface and a further five cells are seen in the fluid above. The cell bridging the interface is the initiating cell. It is situated mainly below the unstable dashed line and hence drives convection. The five cells in the (stably stratified) fluid above are counter cells, a result of penetrative convection. Note that the centre of the driving cell is situated above the dashed line. This somewhat curious behaviour is a result of the resistance to movement the porous medium offers. This is explained in more detail in section 3.6 where an example in which the driving cell is not as strong as the counter cell above is given.

As Q is made stronger (figure 3.7) the initiating cell moves up slightly and only four counter cells are seen in the fluid above. This is due to the fact that Q is destabilising. The depth of the unstable layer has increased and hence the driving cell becomes deeper.

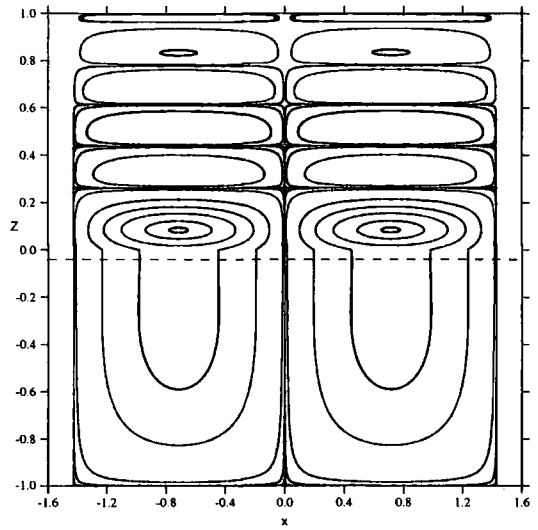

Figure 3.6: Streamline plot from the Q model, $T_U = 9°C$, $\hat{d} = 1$, $\delta = 0.002$, $\hat{\epsilon} = -0.05$, $\hat{\epsilon}_m = -0.0728$, $Ra_m = 29.155$, $a_m = 2.2$.

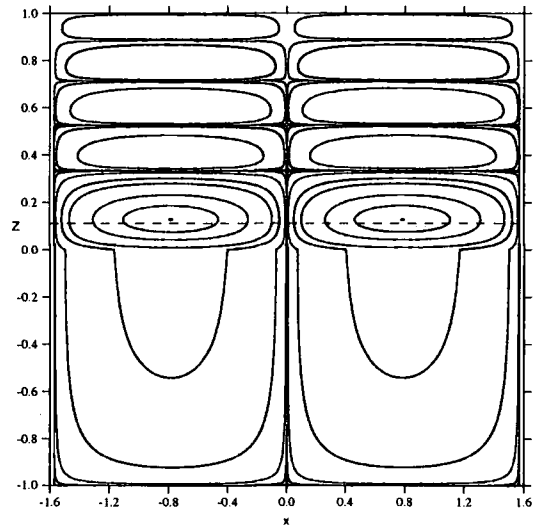

Figure 3.7: Streamline plot from the Q model, $T_U = 9°C$, $\hat{d} = 1$, $\delta = 0.002$, $\hat{\epsilon} = -0.0275$, $\hat{\epsilon}_m = -0.0728$, $Ra_m = 14.112$, $a_m = 2$.

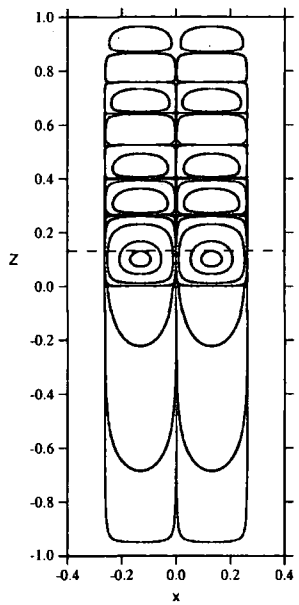

Figure 3.8: Streamline plot from the Q model, $T_U = 9°C$, $\hat{d} = 1$, $\delta = 0.002$, $\hat{\epsilon} = -0.025$, $\hat{\epsilon}_m = -0.0728$, $Ra_m = 8.839$, $a_m = 12$.

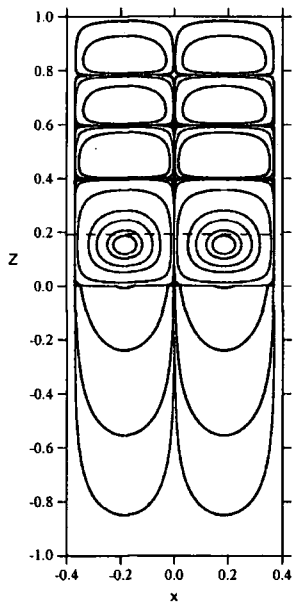

Figure 3.9: Streamline plot from the Q model, $T_U = 9°C$, $\hat{d} = 1$, $\delta = 0.002$, $\hat{\epsilon} = -0.015$, $\hat{\epsilon}_m = -0.0728$, $Ra_m = 0.713$, $a_m = 8.5$.

The stably stratified fluid above is shallower and so fewer counter cells form within it. As the strength of Q is increased again (figure 3.8) the size of the convection cells changes to much narrower cells (the bimodal effect cf. figure 3.5). In this instance there are seven cells almost completely confined to the fluid layer with slight movement into the porous medium. An increase in the strength of Q has clearly resulted in a switch in dominance from porous to fluid dominated convection. If Q is made even stronger (figure 3.9) there is even less movement in the porous medium, just four cells are seen in the fluid layer and the driving cell becomes deeper. Again this is due to the fact that an increase in the strength of Q results in an increase in the depth of the unstable layer. Hence the initiating cell gets deeper and the counter cells above adjust themselves accordingly (for a fixed upper temperature) resulting in fewer counter cells.

In summary, figures 3.6-3.9 have shown that the onset and nature of convection are very sensitive to change in the strength of Q. As the strength of the heat sink in the fluid layer is increased, the fluid layer plays a much stronger role in the convection pattern. Convection switches from porous to fluid dominated, the number of counter cells in the system decreases (for a given mode of dominance) and the depth of the driving cell increases.

3.5.3 Stability characteristics of Q_m

By inspection of (3.5.11) it can be seen that as $\hat{\epsilon}_m$ gets less negative, z_{tp} decreases for fixed $\hat{\epsilon}$ ($-\hat{\epsilon}/\hat{\epsilon}_m$ gets more negative). Therefore when the turning point is in the fluid layer (case 4), the stronger Q_m the more stable the system. This can be explained as follows. In case 4, there is fluid within the fluid layer which is heavier than that at the interface. There is a potentially unstable layer therefore between the interface and the colder fluid above. The stronger the heat sink in the porous medium the colder the fluid at the interface (for fixed Q), and the smaller is the density difference between fluid at the interface and the colder fluid above. Hence the heat sink in the porous medium is stabilising in this instance.

To investigate whether Q_m is stabilising or destabilising when the turning point is in the porous layer is slightly more complicated. Inspection of (3.5.12) reveals that the effect of $\hat{\epsilon}_m$ depends on the sign of $(T_U + 1/\hat{\epsilon})$. Suppose $(T_U + 1/\hat{\epsilon}) < 0$, then as $\hat{\epsilon}_m$ gets less negative, z_{tp}^m decreases (for fixed $\hat{\epsilon}$). So in this case Q_m is stabilising. On the other hand

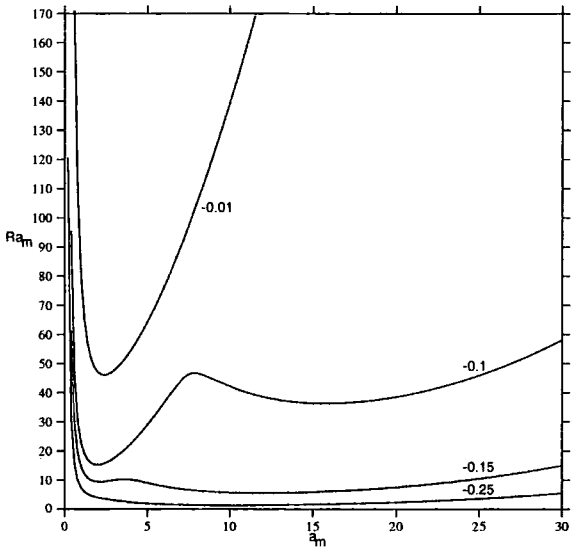

Figure 3.10: Neutral instability curves, Ra_m against a_m. $T_U = 9°\text{C}$, $\hat{d} = 1$, $\hat{\epsilon} = -0.0357$, $\hat{\epsilon}_m$ varies as shown on graph.

suppose $(T_U + 1/\hat{\epsilon}) > 0$, then as $\hat{\epsilon}_m$ gets less negative, z_{tp}^m increases (for fixed $\hat{\epsilon}$). So in this instance Q_m is destabilising. Note that $(T_U + 1/\hat{\epsilon}) < 0 \Leftrightarrow T_0 < 0$, so Q_m can only be stabilising in case 3 such that $T_U < -1/\hat{\epsilon}$. In all other instances for which the unstable layer is confined to the porous medium i.e. case 2 and case 3 with $T_U > -1/\hat{\epsilon}$, Q_m is destabilising.

To illustrate this curious behaviour more clearly consider figures 3.10-3.13. In figure 3.10 the neutral curves for T_U, $\hat{d}$ and $\hat{\epsilon}$ fixed at 9°C, 1 and -0.0357 respectively, with $\hat{\epsilon}_m$ varying are presented. As $\hat{\epsilon}_m$ becomes less negative the neutral curves shift up. Therefore as Q_m gets stronger the system becomes more stable. This is in agreement with the analysis presented above since $T_U < -1/\hat{\epsilon}$, so we expect an increase in the strength of Q_m to have a stabilising effect on the system. In figure 3.11 the corresponding steady state temperature profiles are displayed. It is clear that as $\hat{\epsilon}_m$ becomes less negative the turning point moves down. Note that the steady state temperature profiles are of type 3 and 4 only. Case 2 cannot be obtained since T_U violates (3.5.9).

In figure 3.12 the neutral curves for T_U, $\hat{d}$ and $\hat{\epsilon}$ fixed at 15°C, 1 and -0.1 respectively, with $\hat{\epsilon}_m$ varying are presented. In this instance $\hat{\epsilon}_m$ has the opposite effect. As $\hat{\epsilon}_m$ becomes less negative the neutral curves shift down. Therefore as Q_m gets stronger the system becomes more unstable. This is in agreement with the analysis presented above since

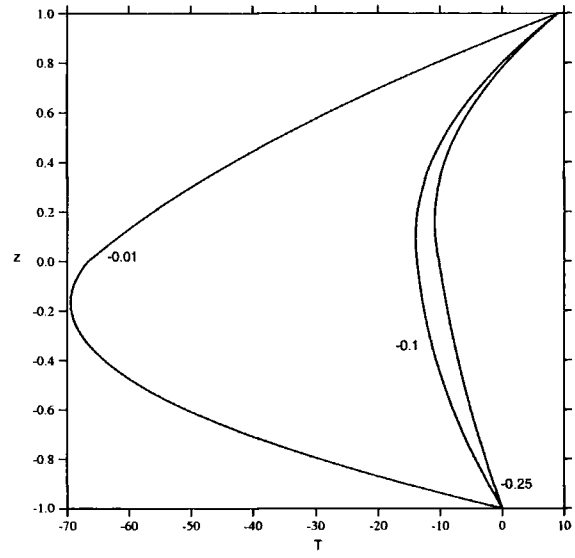

Figure 3.11: Steady state temperature profiles, depth z against temperature T. $T_U = 9°\text{C}$, $\hat{d} = 1$, $\hat{\epsilon} = -0.0357$, $\hat{\epsilon}_m$ varies as shown on graph.

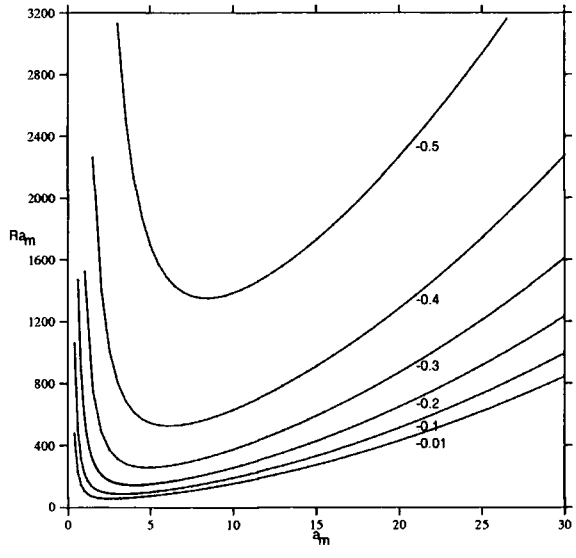

Figure 3.12: Neutral instability curves, Ra_m against a_m. $T_U = 15°\text{C}$, $\hat{d} = 1$, $\hat{\epsilon} = -0.1$, $\hat{\epsilon}_m$ varies as shown on graph.

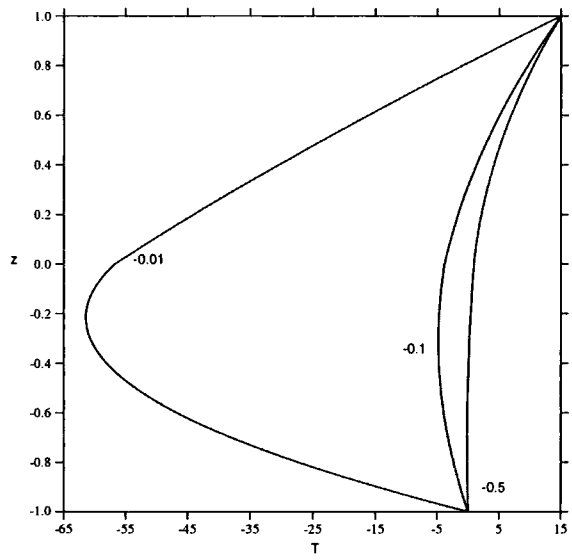

Figure 3.13: Steady state temperature profiles, depth z against temperature T. $T_U = 15°\text{C}$, $\hat{d} = 1$, $\hat{\epsilon} = -0.1$, $\hat{\epsilon}_m$ varies as shown on graph.

$T_U > -1/\hat{\epsilon}$, so we expect an increase in the strength of Q_m to have a destabilising effect on the system. In figure 3.13 the corresponding steady state temperature profiles are displayed. It is clear that as $\hat{\epsilon}_m$ becomes less negative the turning point moves up. Note that the steady state temperature profiles are of type 2 and 3 only. Case 4 cannot be obtained since T_U violates (3.5.5).

It has been shown analytically and in figures 3.12 and 3.13, that in case 2, Q_m is destabilising. This is explained as follows. In case 2 there is fluid within the porous layer which is colder than that at the base of the porous medium. There is a potentially unstable layer therefore between the colder fluid and the base. As the heat sink in the porous medium is made stronger the temperature of the fluid within the porous decreases while that at the base remains fixed. Hence as the heat sink in the porous gets stronger the unstable layer gets deeper (for fixed Q) and the heat sink in the porous medium has a destabilising effect.

To explain the effect of the porous heat sink in case 3 is not so straight forward. For fixed T_U, it has been shown that the effect of the porous heat sink depends strongly upon the strength of the fluid heat sink. If the sink in the fluid is such that $\hat{\epsilon} > -1/T_U$ then the sink in the porous is stabilising. On the other hand if the sink in the fluid is such that $\hat{\epsilon} < -1/T_U$ (weaker) then the sink in the porous is destabilising. To clarify this we

differentiate (3.5.12) with respect to $\hat{\epsilon}_m$ to yield

$$\frac{dz_{tp}^m}{d\hat{\epsilon}_m} = \frac{\mathcal{E} d_m}{2}\left(T_U + \frac{1}{\hat{\epsilon}}\right).$$

This implies that if $\hat{\epsilon} < -1/T_U$ then z_{tp}^m is an increasing function of $\hat{\epsilon}_m$. So as $\hat{\epsilon}_m (< 0)$ increases z_{tp}^m increases as well and Q_m is destabilising. On the other hand if $\hat{\epsilon} > -1/T_U$ then z_{tp}^m is a decreasing function of $\hat{\epsilon}_m$. So as $\hat{\epsilon}_m$ increases z_{tp}^m decreases and in this instance Q_m is stabilising. Clearly $\hat{\epsilon} = -1/T_U$ is a local maximum and the critical point at which Q_m switches from one behaviour to another. The strong interplay between the two heat sinks clearly has a profound effect on the stability characteristics of Q_m and makes a straight forward physical explanation unclear in this case.

In summary, the stability characteristics of Q_m depend strongly on the steady state temperature profile and the strength of Q. In case 2, Q_m is destabilising whereas in case 4 it is stabilising. In case 3, if Q is sufficiently weak ($\hat{\epsilon} < -1/T_U$) then Q_m is destabilising whereas if Q is sufficiently strong ($\hat{\epsilon} > -1/T_U$) it is stabilising. Figures 3.10 and 3.12 both show that as $\hat{\epsilon}_m$ becomes less negative (Q_m stronger) the width of the convection cell switches from narrow (a_m larger) to wide (a_m smaller). Therefore like Q, Q_m has a dramatic effect on both the onset and nature of instability. This is illustrated more clearly in the next section where a selection of streamlines corresponding to figures 3.10 and 3.12 at criticality are presented.

In an entirely analogous analysis to that presented above the effect of varying $\hat{d}$ and T_U can also be investigated. Inspection of (3.5.11) and (3.5.12) imply that $\hat{d}$ and T_U are destabilising and stabilising parameters respectively. This is in agreement with the numerical results of chapter 2.

3.5.4 Variation of the streamlines with Q_m

In this section the streamlines at criticality, corresponding to figures 3.10 and 3.12 are presented. In figures 3.14-3.17, T_U, $\hat{d}$ and $\hat{\epsilon}$ are fixed at 9, 1 and -0.0357 respectively, and $\hat{\epsilon}_m$ is varied from -0.25 to -0.01 (cf. figure 3.10). When $\hat{\epsilon}_m = -0.25$ (figure 3.14) there are six convection cells almost completely confined to the fluid layer with little movement into the porous medium. If Q_m is made stronger (figure 3.15) the convection cells are again mostly confined to the fluid layer but now there are seven cells in total. The increase

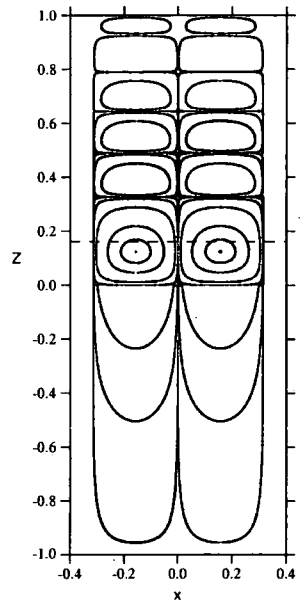

Figure 3.14: Streamline plot from the Q model, $T_U = 9°\text{C}$, $\hat{d} = 1$, $\delta = 0.002$, $\hat{\epsilon} = -0.0357$, $\hat{\epsilon}_m = -0.25$, $Ra_m = 1.317$, $a_m = 10$.

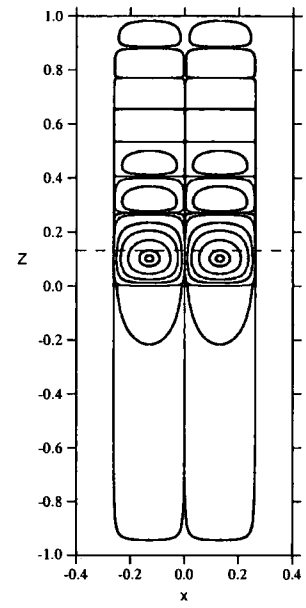

Figure 3.15: Streamline plot from the Q model, $T_U = 9°\text{C}$, $\hat{d} = 1$, $\delta = 0.002$, $\hat{\epsilon} = -0.0357$, $\hat{\epsilon}_m = -0.15$, $Ra_m = 5.534$, $a_m = 12$.

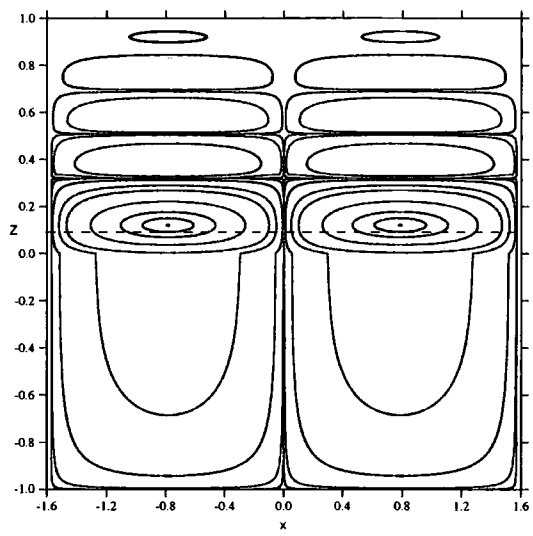

Figure 3.16: Streamline plot from the Q model, $T_U = 9°\text{C}$, $\hat{d} = 1$, $\delta = 0.002$, $\hat{\epsilon} = -0.0357$, $\hat{\epsilon}_m = -0.1$, $Ra_m = 15.262$, $a_m = 2$.

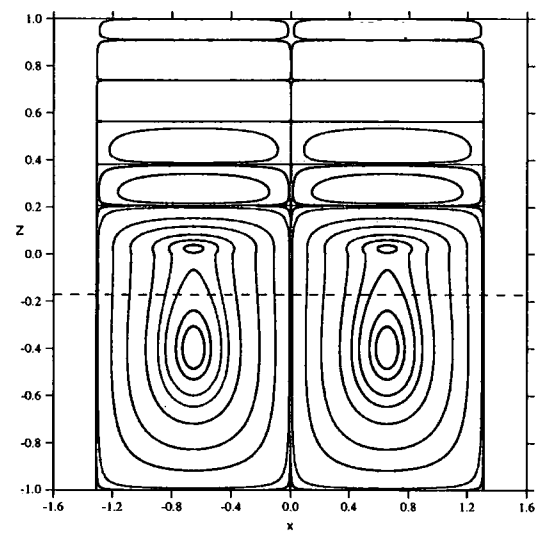

Figure 3.17: Streamline plot from the Q model, $T_U = 9°\text{C}$, $\hat{d} = 1$, $\delta = 0.002$, $\hat{\epsilon} = -0.0357$, $\hat{\epsilon}_m = -0.01$, $Ra_m = 46.107$, $a_m = 2.4$.

in the number of cells is due to the fact that the depth of the unstable layer (everywhere below the dashed line) becomes shallower with an increase in Q_m. Recall that Q_m is stabilising in this instance. The stably stratified fluid above adjusts itself accordingly resulting in an extra counter cell.

If the strength of Q_m is increased further (figure 3.16) the convection pattern changes altogether. The width of the cells becomes wider (the bimodal effect cf. figure 3.10) and the porous medium dominates the convection pattern. In this instance there is one cell bridging the porous-fluid interface and a further four counter cells are seen in the fluid above. When the strength of Q_m is increased again (figure 3.17), the initiating cell still bridges the interface but now the centre of the driving cell is in the porous medium (as opposed to the fluid layer), and there are five counter cells in the fluid above. The shift in the position of the centre of the cell indicates that an increase in the strength of Q_m corresponds to an increase in the dominance of the porous medium. As previously explained the number of counter cells has increased since the unstable layer has become shallower.

Figures 3.14-3.17 clearly show that as the strength of the heat sink in the porous layer is increased, the porous medium plays a much stronger role in the convection pattern. Convection switches from fluid to porous dominated, the number of counter cells in the system increases (for a given mode of dominance) and the depth of the driving cell decreases.

In figures 3.18 and 3.19 we concentrate on the behaviour of the streamlines when Q_m is destabilising. In this instance T_U, $\hat{d}$ and $\hat{\epsilon}$ are fixed at 15, 1 and -0.1 respectively, and $\hat{\epsilon}_m$ varies from -0.5 to -0.01 (cf. figure 3.12). Note that in figure 3.18 penetrative convection is witnessed in the porous medium. This is the first time we have seen such behaviour in the two layer system and we highlight this novel result. The relatively shallow depth of the unstable layer explains the occurrence of penetrative convection in the porous medium. The driving cell in the lower region of the porous medium induces penetrative convection in the stable porous medium and fluid above. It is worth noting however that the counter cells are very weak in comparison to the driving cell. Inspection of the eigenfunction reveals that the strongest counter cell (the one directly above the driving cell) is approximately 200 times weaker than the driving cell below. The counter cells above it

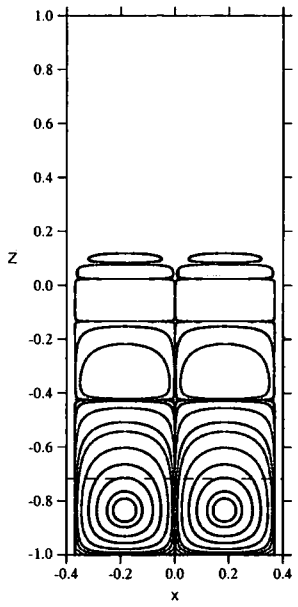

Figure 3.18: Streamline plot from the Q model, $T_U = 15°C$, $\hat{d} = 1$, $\delta = 0.002$, $\hat{\epsilon} = -0.1$, $\hat{\epsilon}_m = -0.5$, $Ra_m = 1352.493$, $a_m = 8.5$.

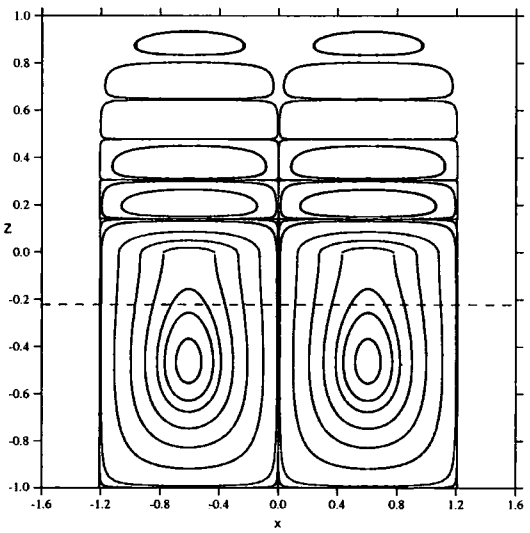

Figure 3.19: Streamline plot from the Q model, $T_U = 15°C$, $\hat{d} = 1$, $\delta = 0.002$, $\hat{\epsilon} = -0.1$, $\hat{\epsilon}_m = -0.01$, $Ra_m = 57.061$, $a_m = 2.6$.

are even weaker again.

In figure 3.19 the strength of Q_m is stronger than that in figure 3.18. In this instance the convection pattern is completely different to that previously illustrated. The cells are wider, the driving cell spans the porous-fluid interface and five counter cells are observed. This shows that an increase in the strength of the heat sink in the porous layer corresponds to increased movement in the porous medium. Note that there is no switch in dominance between the two mediums in this case but the width of the cells does change from narrow to broad with an increase in Q_m (cf. figure 3.12).

3.6 Comparison with the Quadratic Density Model

In chapter 2, penetrative convection in the porous-fluid system was modelled via a quadratic density profile. The governing equations differed in that those of chapter 2 did not include an internal heat sink in either layer. Instead penetrative convection was modelled via a

quadratic density profile of the form

$$\rho = \rho_0\left[1 - \bar{\alpha}(T-4)^2\right].$$

Recall from chapter 2, the non-dimensional linearised perturbation equations (2.3.1) and (2.3.2) (from now on called the T^2 model),

$$\begin{aligned} \sigma u_i &= -\pi_{,i} + \Delta u_i - 2R_{T^2}M(z)\theta k_i, \\ u_{i,i} &= 0, \\ \sigma Pr\theta &= \Delta\theta - R_{T^2}w, \end{aligned} \tag{3.6.1}$$

and,

$$\begin{aligned} \delta^2\pi^m_{,i} &= -u^m_i - 2R^m_{T^2}M^m(z)\theta^m k_i, \\ u^m_{i,i} &= 0, \\ \sigma\omega Pr_m G_m\theta^m &= \Delta\theta^m - R^m_{T^2}w^m, \end{aligned} \tag{3.6.2}$$

where

$$R^2_{T^2} = \frac{g\bar{\alpha}d^3T_U^2(1-\mathcal{E})^2}{\nu\lambda}, \qquad M(z) = \xi - z, \qquad \xi = \frac{4/T_U - \mathcal{E}}{1-\mathcal{E}},$$
$$R^{m2}_{T^2} = \frac{g\bar{\alpha}KPr^m d_m T_U^2\mathcal{E}^2}{\nu^2}, \qquad M^m(z) = \xi_m - z, \qquad \xi_m = \frac{4/T_U - \mathcal{E}}{\mathcal{E}}.$$

From section 3.3 recall the non-dimensional linearised perturbation equations (3.3.1) and 3.3.2) (from now on called the Q model),

$$\begin{aligned} \sigma u_i &= -\pi_{,i} + \Delta u_i + R\theta k_i, \\ u_{i,i} &= 0, \\ \sigma Pr\theta &= \Delta\theta + Rf(z)w, \end{aligned} \tag{3.6.3}$$

and,

$$\begin{aligned} \delta^2\pi^m_{,i} &= -u^m_i + R^m\theta^m k_i, \\ u^m_{i,i} &= 0, \\ \sigma\omega Pr_m G_m\theta^m &= \Delta\theta^m + R^m f^m(z)w^m, \end{aligned} \tag{3.6.4}$$

where

$$f(z) = 1 - 2z + (T_U - T_0)\hat{\epsilon}, \qquad f^m(z) = T_0\hat{\epsilon}_m - 2z - 1.$$

To investigate if and when these two systems are adjoint we follow an analysis similar to the one given in Tracey [99]. First note that, the adjoint A^*, of an $n \times n$ matrix A is defined by the following relation

$$(\mathbf{x}, A\mathbf{y}) = (A^*\mathbf{x}, \mathbf{y}),$$

for all n vectors $\mathbf{x}$ and $\mathbf{y}$. If two systems are adjoint then the eigenvalues of both systems are the same.

Let $\Phi = (\pi, u, v, w, \theta, \pi^m, u^m, v^m, w^m, \theta^m)^T$, where u, u^m and v, v^m are the **i**, **j**-components of $\mathbf{u}$ and $\mathbf{u^m}$ respectively. If we identify θ with $-\theta$ in the heat sink model then the two systems can be written as $A_{T^2}\Phi = \sigma B\Phi$ (quadratic density law) and $A_Q\Phi = \sigma B\Phi$ (heat sink), where the operators A_{T^2}, A_Q, and B are defined by

$$A_{T^2} = \begin{pmatrix}
0 & -\frac{\partial}{\partial x} & -\frac{\partial}{\partial y} & -\frac{\partial}{\partial z} & 0 & \dots & \dots & \dots & \dots & 0 \\
-\frac{\partial}{\partial x} & \Delta & 0 & 0 & 0 & \dots & \dots & \dots & \dots & \vdots \\
-\frac{\partial}{\partial y} & 0 & \Delta & 0 & 0 & \dots & \dots & \dots & \dots & \vdots \\
-\frac{\partial}{\partial z} & 0 & 0 & \Delta & -2R_{T^2}M & \dots & \dots & \dots & \dots & \vdots \\
0 & 0 & 0 & -R_{T^2} & \Delta & \dots & \dots & \dots & \dots & \vdots \\
0 & \dots & \dots & \dots & \dots & 0 & \delta^2\frac{\partial}{\partial x} & \delta^2\frac{\partial}{\partial y} & \delta^2\frac{\partial}{\partial z} & 0 \\
\vdots & \dots & \dots & \dots & \dots & \delta^2\frac{\partial}{\partial x} & 1 & 0 & 0 & 0 \\
\vdots & \dots & \dots & \dots & \dots & \delta^2\frac{\partial}{\partial y} & 0 & 1 & 0 & 0 \\
\vdots & \dots & \dots & \dots & \dots & \delta^2\frac{\partial}{\partial z} & 0 & 0 & 1 & 2R^m_{T^2}M^m \\
0 & \dots & \dots & \dots & \dots & 0 & 0 & 0 & -R^m_{T^2} & \Delta
\end{pmatrix},$$

$$A_Q = \begin{pmatrix}
0 & -\frac{\partial}{\partial x} & -\frac{\partial}{\partial y} & -\frac{\partial}{\partial z} & 0 & \dots & \dots & \dots & \dots & 0 \\
-\frac{\partial}{\partial x} & \Delta & 0 & 0 & 0 & \dots & \dots & \dots & \dots & \vdots \\
-\frac{\partial}{\partial y} & 0 & \Delta & 0 & 0 & \dots & \dots & \dots & \dots & \vdots \\
-\frac{\partial}{\partial z} & 0 & 0 & \Delta & -R & 0 & \dots & \dots & \dots & \vdots \\
0 & 0 & 0 & -Rf(z) & \Delta & \dots & \dots & \dots & \dots & \vdots \\
0 & \dots & \dots & \dots & \dots & 0 & \delta^2\frac{\partial}{\partial x} & \delta^2\frac{\partial}{\partial y} & \delta^2\frac{\partial}{\partial z} & 0 \\
\vdots & \dots & \dots & \dots & \dots & \delta^2\frac{\partial}{\partial x} & 1 & 0 & 0 & 0 \\
\vdots & \dots & \dots & \dots & \dots & \delta^2\frac{\partial}{\partial y} & 0 & 1 & 0 & 0 \\
\vdots & \dots & \dots & \dots & \dots & \delta^2\frac{\partial}{\partial z} & 0 & 0 & 1 & -R^m \\
0 & \dots & \dots & \dots & \dots & 0 & 0 & 0 & R^m f^m(z) & \Delta
\end{pmatrix},$$

$$B = \begin{pmatrix} 0 & 0 & 0 & 0 & 0 & \dots & 0 \\ 0 & 1 & 0 & 0 & 0 & \dots & 0 \\ 0 & 0 & 1 & 0 & 0 & \dots & 0 \\ 0 & 0 & 0 & 1 & 0 & \dots & 0 \\ 0 & 0 & 0 & 0 & Pr & \dots & 0 \\ \vdots & & & & & \ddots & \vdots \\ 0 & \dots & & & & & \omega Pr^m G_m \end{pmatrix}.$$

Now, let $\mathbf{\Phi_1}$ and $\mathbf{\Phi_2}$ be independent. It is not difficult to show that $\langle A_{T^2}\mathbf{\Phi_1}, \mathbf{\Phi_2}\rangle = \langle \mathbf{\Phi_1}, A_Q\mathbf{\Phi_2}\rangle$ iff

$$\begin{aligned} R_{T^2} &= R, \qquad f(z) = 2M(z), \\ R^m_{T^2} &= R^m, \qquad f^m(z) = 2M^m(z). \end{aligned} \tag{3.6.5}$$

Conditions (3.6.5) are satisfied iff

$$\hat{\epsilon} = \frac{-1}{T_U^2(1-\mathcal{E})^2}, \qquad T_0 = T_U + \frac{1-2\xi}{\hat{\epsilon}}, \tag{3.6.6}$$

$$\hat{\epsilon}_m = \frac{-1}{T_U^2\mathcal{E}^2}, \qquad T_0 = \frac{2\xi^m + 1}{\hat{\epsilon}_m}. \tag{3.6.7}$$

Substituting $(3.6.6)_1$ into $(3.6.6)_2$, $(3.6.7)_1$ into $(3.6.7)_2$ and eliminating T_0 we find that

$$T_U = 9°\text{C}.$$

Then choosing $T_U = 9°\text{C}$ and $\hat{\epsilon}, \hat{\epsilon}_m$ such that $(3.6.6)_1$, $(3.6.7)_1$, are satisfied, we have $A_Q^* = A_{T^2}$ (where A_Q^* is the adjoint of A_Q). In this case the two linearised models give rise to the same instability boundary and we expect the two models to yield the same critical eigenvalues. In table 3.1 a comparison of the critical porous Rayleigh numbers and wave numbers obtained from the Q model with $T_U = 9°\text{C}$, and $\hat{\epsilon}, \hat{\epsilon}_m$ satisfying $(3.6.6)_1$, $(3.6.7)_1$, with those from the T^2 model with $T_U = 9°\text{C}$ is made. Very good agreement between the two is seen.

The eigenvalues from the Q and T^2 models are in good agreement when the two are adjoint, the corresponding eigenfunctions however are not. For example consider the W eigenfunctions for the two models when $\hat{d} = 1$, $T_U = 9°\text{C}$ and $\hat{\epsilon}, \hat{\epsilon}_m$ satisfy $(3.6.6)_1$, $(3.6.7)_1$, as illustrated in figure 3.20. Note that in computing the eigenfunctions we have normalised over both W and W_m. The strongest cell therefore is always positive regardless of it's true circulation. Hence we cannot determine the true direction of circulation

$\hat{d}$	$Ra^m_{T^2}$	Ra^m_Q	$a^m_{T^2}$	a^m_Q
0.05	273.311	273.322	5.0	5.0
0.10	225.470	225.631	4.5	4.5
0.50	61.942	62.844	2.5	2.5
1.00	19.902	20.233	2.0	2.0

Table 3.1: The critical porous Rayleigh number and wave number when the two models are adjoint.

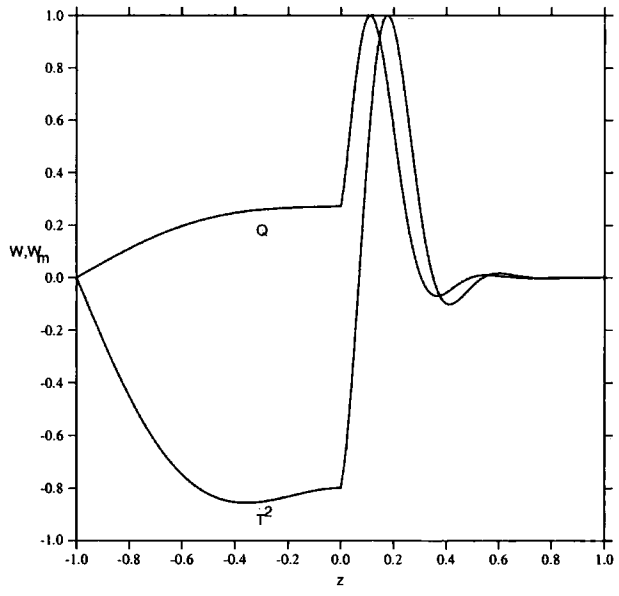

Figure 3.20: W eigenfunctions for the adjoint models, $T_U = 9°\text{C}$, $\hat{d} = 1$.

from the eigenfunction. We can conclude however that wherever a sign change occurs a counter cell is present. Figure 3.20 clearly shows that the eigenfunctions exhibit different behaviour. The main difference between the two is the position of the strongest cell. In the Q model it is the first cell which is the strongest whereas in the T^2 scenario it is the second. To illustrate this more clearly consider the corresponding streamlines given in figures 3.21 and 3.22.

In figure 3.21, $T_U, \hat{d}$ and δ are fixed at $9°\text{C}, 1$ and 0.002 respectively. A streamline plot obtained via the T^2 model at the onset of convection is presented. In this instance the dashed line represents the $4°\text{C}$ conduction solution (below which the fluid is unstable since water has a density maximum at $4°\text{C}$ in this model). The plot shows one cell in the porous medium just bridging the interface, with a further 5 cells in the fluid above. In

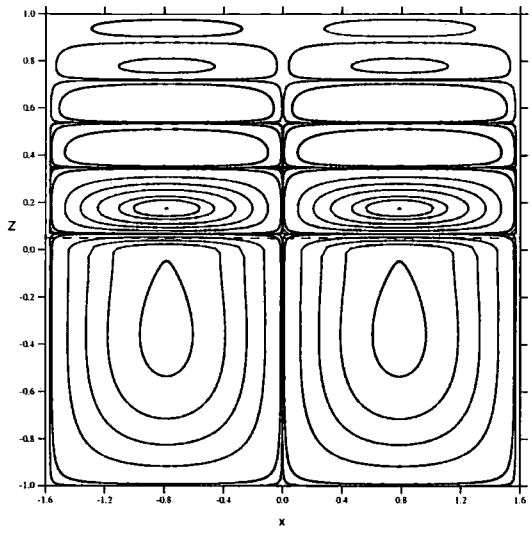

Figure 3.21: Streamline plot from the T^2 model, $T_U = 9°C$, $\hat{d} = 1$, $\delta = 0.002$, $Ra_m = 19.902$, $a_m = 2$.

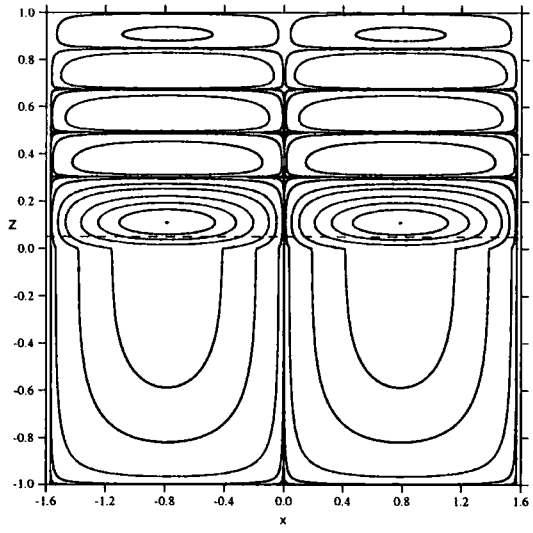

Figure 3.22: Streamline plot from the Q model, $T_U = 9°C$, $\hat{d} = 1$, $\delta = 0.002$, $\hat{\epsilon}, \hat{\epsilon}_m$ take adjoint values, $Ra_m = 20.233$, $a_m = 2$.

figure 3.22, T_U, $\hat{d}$ and δ are also fixed at 9°C, 1 and 0.002 respectively and $\hat{\epsilon}, \hat{\epsilon}_m$ take the adjoint values $(3.6.6)_1$, $(3.6.7)_1$. A streamline plot obtained via the Q model at the onset of instability is presented. In this case the dashed line represents the turning point of the steady state solution (below which the fluid is unstable, see section 3.5). The two unstable layers coincide exactly in the steady states. This can be proved analytically by simply inspecting the steady state solutions of each model and evaluating them at the adjoint values. The plot in figure 3.22 shows one cell bridging the fluid and porous medium with a further 4 cells in the fluid above. Figures 3.21 and 3.22 clearly show that the Q and T^2 models generate different streamlines despite being mathematically adjoint and yielding near exact eigenvalues. The physical processes that determine the depth of the unstable layer (and hence drive convection) are very different in the two models. In the T^2 model it is the fact that density is a quadratic function of temperature whereas in the Q model it is the inclusion of the heat sinks. Hence we cannot expect the streamlines to be the same even when the two models are adjoint. The two models represent very different physical systems and this must be understood in their application and interpretation at the outset.

Figure 3.21 is curious in that the cell which initiates penetrative convection (the lower one confined mostly below the dashed line) is not as strong as the counter cell above. One explanation for this is the resistance to movement the porous medium offers. For

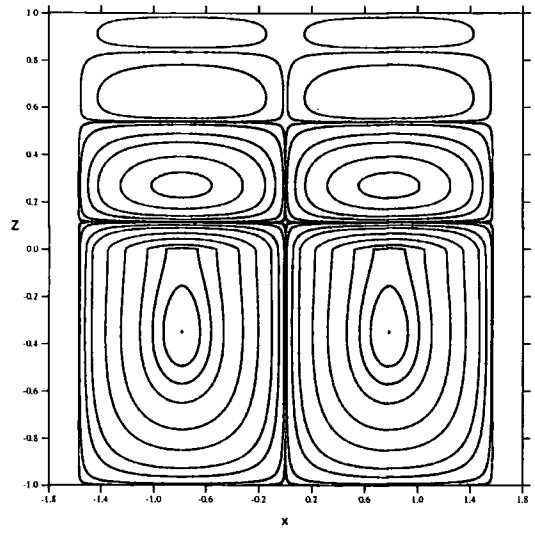

Figure 3.23: Streamline plot from the T^2 model, $T_U = 9°\text{C}$, $\hat{d} = 1$, $\delta = 0.01$, $Ra_m = 18.534$, $a_m = 2$.

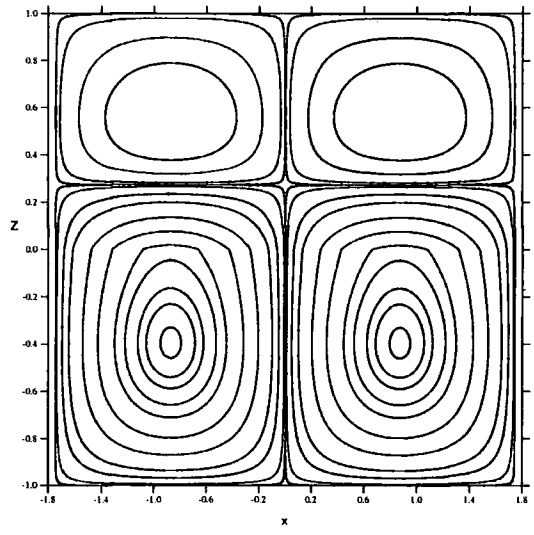

Figure 3.24: Streamline plot from the T^2 model, $T_U = 9°\text{C}$, $\hat{d} = 1$, $\delta = 0.1$, $Ra_m = 18.928$, $a_m = 1.8$.

example if the porous medium were more permeable, the fluid within would be freer to move and we would expect the initiating cell to be stronger. To illustrate this notion more clearly consider figure 3.23. In figure 3.23 a streamline plot generated via the T^2 model for $T_U, \hat{d}$ and δ fixed at $9°\text{C}, 1$, and 0.01 respectively, is presented. Recall that $\delta = \sqrt{K}/d_m$, where K is the permeability of the porous medium. So in figure 3.23 the porous medium is more permeable than that presented in figure 3.21. In figure 3.23 we note that the initiating cell is now the strongest and there are only 3 cells in the fluid above. Clearly the increase in permeability has allowed the lower cell (mainly confined to the porous medium) to dominate the convection pattern. To reinforce this consider what happens when δ is increased further (figure 3.24). In this case $\delta = 0.1$ and the initiating cell is definitely the dominant cell. There is only one cell in the fluid above. Clearly an increase in permeability has allowed the porous medium to have a much stronger role in the convection pattern.

Conversely if the porous medium were made less permeable we would expect the lower (porous dominated) cell to become weaker and the motion in the fluid above to become stronger. Close inspection of the eigenfunction when $\delta = 0.0003$ (keeping $\hat{d} = 1$ and $T_U = 9°\text{C}$) revealed that in this case, there is one cell in the porous medium just bridging the interface with a further 10 counter cells in the fluid above. The lowest counter

cell was the strongest with the initiating cell below having a strength approximately $2/5$ of that above. Hence as predicted, when the porous medium is made less permeable the first counter cell can indeed be stronger than the initiating cell and greater movement is seen within the fluid layer.

If the porous medium is made even less permeable it is found that convective motion is almost completely confined to the fluid layer and the width of the convection cells changes. Inspection of the eigenfunction when $\delta = 0.0002$, revealed that in this instance there were 21 cells in the fluid layer. The initiating cell was the lowest and strongest in the layer, and there was only slight movement into the porous medium. The critical porous wave number was found to be $a_m = 30.6$ and so the cells much narrower than those previously seen. It is worth noting at this point that care must be taken when interpreting data from the neutral instability curves. It is often inferred from the critical mode what the *dominant* layer is. For example if the critical wave number is small, the porous medium is said to dominate convection whereas if it is large the fluid layer is believed to, cf. Chen & Chen [17]. To avoid confusion exactly what is meant by *dominant* must be understood. The *dominant* layer refers to the layer in which instability commences. The layer contains the initiating (driving) cell but as illustrated this may not necessarily be the strongest cell.

Equations (3.6.1)-(3.6.4) clearly show that the Prandtl number Pr, is a parameter of the governing system. However it is worth noting that when Pr was varied from 0.001-1000, no significant difference was seen in the critical eigenvalues obtained from either model.

3.7 Concluding Remarks

In this chapter we have modelled penetrative convection via internal heating for a two layer system in which fluid overlies and saturates a porous medium. It was found that internal heating must be via a sink and a sink was included in both layers. The instability of the system was found to be very sensitive to change in the strength of the sinks. It was shown analytically and numerically that the sink in the fluid layer had a destabilising effect on the system. The effect of the sink in the porous medium however depended upon what type of steady state temperature profile was being considered and on the strength of

the heat sink in the fluid layer. An array of streamlines were presented to illustrate the effects of varying Q and Q_m on the pattern of instability.

The model presented in this chapter was compared to that given in chapter 2. When mathematically adjoint, the two models were shown to yield the same critical instability boundaries but different eigenfunctions. Hence the Q model confirmed the instability boundaries of chapter 2 and a need for caution and understanding, when interpreting physical results was highlighted. Physically, the Q model is very different to the T^2 one and we stress this point.

The linear instability analysis presented here and that given in chapter 2 provide information about the nature and onset of instability. However they do not preclude the possibility of subcritical instabilities. A nonlinear analysis is necessary to assess the validity of the linear work. Straughan & Walker [96] pointed out that a Q model can make a nonlinear energy analysis more straightforward than one involving a quadratic equation of state. In future work it is our intent to develop a nonlinear stability analysis for the two layer problem. It is hoped that the mathematical properties of the Q model can be utilised in this task. The favourable properties of a Q model are discussed in more detail in the following chapter and the possible application to a nonlinear analysis of the two layer system is discussed in chapter 7.

Chapter 4

Penetrative Convection in a Horizontally Isotropic Porous Layer

In this chapter penetrative convection in a horizontally isotropic porous layer is investigated. A horizontally isotropic porous medium is one in which the permeability is the same in all directions in the horizontal plane, but different in the direction of the vertical axis. The effect of anisotropy on convection in porous media is a subject receiving recent attention. For example, Qin & Kaloni [80] studied the onset of Rayleigh-Bénard convection in a porous layer, using Brinkman's equation and anisotropic permeability. In general, they allowed different components of permeability in all three principal directions. However, they do briefly investigate the horizontally isotropic porous medium case as well. Straughan & Walker [96] dealt with a porous medium for which the permeability was transversely isotropic with respect to an inclined axis. They found that the growth rate σ was real in the anisotropic case without penetrative convection as well as in the isotropic case with penetrative convection. In this chapter we show that for a horizontally isotropic medium (anisotropic configuration) the growth rate σ is real even with penetrative convection.

It is our intent to model penetrative convection via internal heating and a quadratic equation of state. For the majority of the analysis we choose to describe penetrative convection by internal heating. The motivation for this choice is the fact that it allows us to perform a non weighted energy analysis to obtain a global stability bound. The system is also modelled via a quadratic density law since the results it produces are easier to in-

terpret physically than those obtained via internal heating. The two models are compared and it is shown that the linearised forms of each are in fact mathematically adjoint and therefore, the instability boundaries which can be obtained from the models are the same, cf. Tracey [99] and chapter 3.

Straughan & Walker [96] dealt primarily with the quadratic density model, however, they also gave a brief development of a model with a uniform heat sink. In this chapter the same configuration is taken, but it is simplified to a horizontally isotropic medium. This model is of physical relevance to real life situations since many geothermal rock/soil structures display anisotropy where the permeability in the vertical direction is different to that in the horizontal plane. An example of such anisotropy is soil lofting due to frost heave. This plays an integral part in the formation of patterned ground, cf. George *et al.* [33]. Another example is the permeability of sea ice, cf. Eicken *et al.* [27]. Possible applications of modelling sea ice as an anisotropic porous medium are discussed at length in chapter 7. Further anisotropy effects can be found in Nield & Bejan [73].

An outline of this chapter is as follows. To begin with an internal heat sink model which allows for penetrative convection in a horizontally isotropic porous medium is introduced. It is then shown that for the linearised system the growth rate σ is real. Using this result an instability boundary is found for the linearised system. After this an energy analysis is performed to obtain a global nonlinear stability bound. The model is then compared with one in which the density is assumed quadratic and it is shown that the two linearised systems are mathematically adjoint. Finally, a presentation and discussion of the numerical results is given in the last section.

4.1 Internal Heat Sink Model

Consider a porous layer saturated with fluid contained between the horizontal planes $z = 0$ and $z = d$. The z direction is denoted by the vector $\mathbf{k}$ with $\mathbf{i}, \mathbf{j}, \mathbf{k}$ being the standard Cartesian basis. Gravity acts in the negative z direction and the upper and lower planes are held fixed at temperatures T_u and T_l respectively, see figure 4.1. The density is assumed to have a linear temperature dependence of the form

$$\rho = \rho_o\big[1 - \alpha(T - T_o)\big], \tag{4.1.1}$$

where ρ, T, and α are density, temperature and thermal expansion respectively, and ρ_o and T_o are constant reference values for the density and temperature respectively.

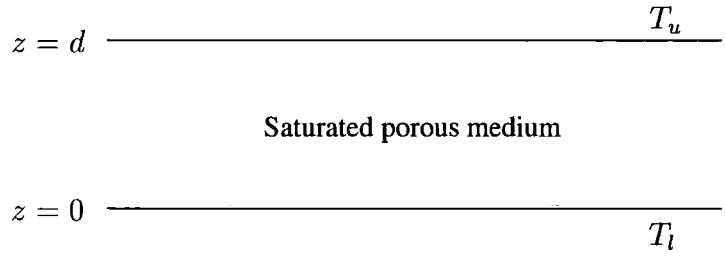

Figure 4.1: Schematic diagram of the governing system.

Attention is restricted to the anisotropic case for which permeability in the **k** direction is different to that in the **i** and **j** directions. Hence the permeability tensor K is chosen to be of the form

$$K = \begin{pmatrix} k_1 & 0 & 0 \\ 0 & k_1 & 0 \\ 0 & 0 & k_2 \end{pmatrix},$$

where clearly k_1 is the permeability in the **i** and **j** directions and k_2 is the permeability in the **k** direction. The inverse permeability tensor M is given by

$$M = K^{-1} = \frac{1}{k_2} \begin{pmatrix} \xi & 0 & 0 \\ 0 & \xi & 0 \\ 0 & 0 & 1 \end{pmatrix},$$

where $\xi = k_2/k_1$ is the anisotropy parameter.

The fluid motion in the porous layer is assumed to satisfy Darcy's law with a Boussinesq approximation,

$$\frac{\partial v_i}{\partial t} = -\frac{1}{\rho_o}\frac{\partial p}{\partial x_i} - \nu M_{ij} v_j - \frac{g\rho(T)k_i}{\rho_o}, \tag{4.1.2}$$

where v_i, t, p, x_i, ν, and g, are velocity, time, pressure, displacement, kinematic viscosity, and gravity respectively. Standard indicial notation and the Einstein summation convention are employed throughout, and as previously mentioned $\mathbf{k} = (0, 0, 1)^T$. We choose to neglect inertia again and henceforth discard the $v_{i,t}$ term in (4.1.2). The constant term in (4.1.1) is absorbed into the pressure by defining a modified pressure $\hat{p}$ to

be $p + g\rho_o(1 + \alpha T_o)z$. Then, dropping the hat and neglecting the inertial term, (4.1.2) becomes

$$p_{,i} = -\mu M_{ij} v_j + \rho_o \alpha g k_i T, \tag{4.1.3}$$

where μ is the dynamic viscosity. Equation (4.1.3) together with the incompressibility condition and the equation of energy balance yield the following system of governing equations

$$\begin{aligned} p_{,i} &= -\mu M_{ij} v_j + \rho_o \alpha g k_i T, \\ v_{i,i} &= 0, \\ T_{,t} + v_i T_{,i} &= \kappa \Delta T + Q. \end{aligned} \tag{4.1.4}$$

Here, κ is the thermal diffusivity, Q is some (constant) internal heat source or sink and Δ is the Laplace operator. The upper and the lower boundaries of the system are assumed fixed, so the boundary conditions $v_3(0) = v_3(d) = 0$, $T(0) = T_l$, $T(d) = T_u$, must be imposed.

Consider the integral form of the energy balance equation $(4.1.4)_3$, namely,

$$\frac{d}{dt}\int_V T dV + \int_V v_i \frac{\partial T}{\partial x_i} dV = \kappa \int_V \frac{\partial}{\partial x_i}\left(\frac{\partial T}{\partial x_i}\right) dV + \int_V Q dV, \tag{4.1.5}$$

where V is some periodic cell in the saturated porous layer $z \in (0, d)$. Using the boundary conditions and divergence theorem, (4.1.5) can be simplified to find

$$\frac{d}{dt}\int_V T dV = \kappa \oint_{\partial V} n_i \frac{\partial T}{\partial x_i} dA + \int_V Q dV,$$

where n_i is the unit normal to V and ∂V the bounding surface of V. Note that, in the absence of any heat flux, a positive value of Q will give rise to an increase in temperature of the layer and similarly, a negative value of Q will yield a decrease. Therefore a positive value of Q represents an internal heat source and a negative value of Q an internal heat sink.

The basic steady state solutions of (4.1.4) in whose stability we are interested, are obtained from

$$\bar{v}_i = 0, \qquad \bar{T}'' = -\frac{Q}{\kappa}.$$

The hydrostatic pressure $\bar{p}$ may be found from $(4.1.4)_1$ but since $\bar{p}$ is eliminated from our analysis later on, a derivation of it is not included here. Integrating $\bar{T}''$ twice yields

$$\bar{T}(z) = -\frac{Q}{2\kappa} z^2 + \left(\frac{T_u - T_l}{d} + \frac{Qd}{2\kappa}\right) z + T_l.$$

For the system to be in a potentially gravitationally unstable state the condition $T_l > T_u > T_{min}$ where T_{min} is the minimum temperature of the fluid is imposed. Furthermore, we take $Q < 0$, i.e. we deal explicitly with the case of a heat sink. In this situation the lower part of the layer has a tendency to be gravitationally unstable whereas the upper part is stable. Hence penetrative convection can arise when the fluid in the unstable layer begins to convect and induce motion in the upper part.

To study the stability of (4.1.4) perturbations to the steady state solutions are introduced as follows

$$v_i = \bar{v}_i + u_i, \qquad T = \bar{T} + \theta, \qquad p = \bar{p} + \pi.$$

The perturbed expressions are then substituted into (4.1.4) and non-dimensionalised with scalings of

$$X = d, \qquad \mathcal{T} = \frac{d^2}{\kappa}, \qquad U = \frac{\kappa}{d}, \qquad P = \mu\kappa, \qquad \left(T^{\#}\right)^2 = -\frac{Qd\mu}{\rho_o \alpha g},$$

for displacement, time, velocity, pressure and temperature respectively. Then (4.1.4) may be written in terms of the non-dimensional perturbation quantities as

$$\begin{aligned} \pi_{,i} &= -M_{ij}u_j + Rk_i\theta, \\ u_{i,i} &= 0, \\ \theta_{,t} + u_i\theta_{,i} &= Rf(z)w + \Delta\theta, \end{aligned} \tag{4.1.6}$$

where

$$f(z) = \frac{1}{2} - \epsilon - z, \qquad \epsilon = -\frac{(T_u - T_l)\kappa}{Qd^2}, \qquad w = u_3, \qquad \mathbf{x} \in \mathbb{R}^2 \times [0,1],$$

and

$$R^2 = -\frac{Q\rho_o \alpha g d^3}{\mu\kappa^2}, \tag{4.1.7}$$

defines the so called Rayleigh number. The boundary conditions for the perturbed variables are

$$w(0) = w(1) = 0, \qquad \theta(0) = \theta(1) = 0. \tag{4.1.8}$$

4.2 Linearised Instability Theory and The Principle of Exchange of Stabilities

Neglecting the nonlinear terms in (4.1.6) and assuming a temporal growth rate like $e^{\sigma t}$ we obtain the linearised system

$$\begin{aligned} \pi_{,i} &= -M_{ij}u_j + Rk_i\theta, \\ u_{i,i} &= 0, \\ \sigma\theta &= Rf(z)w + \Delta\theta. \end{aligned} \tag{4.2.1}$$

To eliminate the pressure in $(4.2.1)_1$, curlcurl of both sides is taken. Then, setting $i = 3$, yields

$$M_{33}\Delta w - M_{jj}u_{j,3j} - R\Delta^*\theta = 0, \tag{4.2.2}$$

where Δ^* is the horizontal Laplacian, $\Delta^* = \partial^2/\partial x^2 + \partial^2/\partial y^2$. Finally, using the incompressibility relation $(4.2.1)_2$ in (4.2.2), system (4.2.1) can be written as follows

$$\begin{aligned} \mathcal{L}w &= R\Delta^*\theta, \\ (\Delta - \sigma)\,\theta &= -Rf(z)w, \end{aligned} \tag{4.2.3}$$

where the operator $\mathcal{L}$ is defined as $\Delta^* + \xi\partial^2/\partial z^2$.

To show that $\sigma \in \mathbb{R}$, let $\sigma = \sigma_r + \sigma_i i$, where σ_r and σ_i are both real. Applying Δ^* to $(4.2.3)_2$ and substituting the expression for $\Delta^*\theta$ from $(4.2.3)_1$, the system can be rewritten as a single fourth order equation in w, namely

$$(\Delta - \sigma)\,\mathcal{L}w = -R^2 f(z)\Delta^* w. \tag{4.2.4}$$

The boundary conditions are $w = w_{,zz} = 0$ for $z \in \{0, 1\}$. Let V now be some periodic cell and introduce the complex L^2-inner product as follows

$$\langle u, v\rangle = \int_V uv^* dV,$$

where the asterisk here denotes complex conjugation. In general, $\langle . \rangle$ will mean integration over V. After multiplying equation (4.2.4) on the right by the conjugate of w and integrating over V, there results

$$\begin{aligned} \xi\left\langle \Delta w_{,zz}, w^*\right\rangle + \left\langle \Delta\Delta^* w, w^*\right\rangle - \sigma\xi\left\langle w_{,zz}, w^*\right\rangle \\ - \sigma\left\langle \Delta^* w, w^*\right\rangle = -R^2\left\langle f(z)\Delta^* w, w^*\right\rangle. \end{aligned}$$

By repeated use of Gauss' theorem and the boundary conditions $w = w_{,zz} = w_{,x} = w_{,y} = 0$ on $z \in \{0, 1\}$, it can be shown that

$$\xi\|\nabla w_{,z}\|^2 + \|\nabla^*\nabla w\|^2 + \sigma\xi\|w_{,z}\|^2 + \sigma\|\nabla^* w\|^2 = R^2 \langle f(z)\nabla^* w, \nabla^* w^* \rangle . \quad (4.2.5)$$

Finally, taking the imaginary part of (4.2.5) yields

$$\sigma_i \left(\xi\|w_{,z}\|^2 + \|\nabla^* w\|^2\right) = 0,$$

which implies that $\sigma_i = 0$. Hence, σ is real and we say that the principle of exchange of stabilities holds. When this holds convection sets in as stationary convection.

Suppose then $\sigma = 0$, equations (4.2.3) yield

$$\begin{aligned} \left(\Delta^* + \xi\frac{\partial^2}{\partial z^2}\right) w &= R\Delta^*\theta, \\ \left(\Delta^* + \frac{\partial^2}{\partial z^2}\right) \theta &= -Rf(z)w. \end{aligned} \quad (4.2.6)$$

Assuming a normal mode representation for w and θ of the form $w = W(z)g(x, y)$ and $\theta = \Theta(z)g(x, y)$, where $g(x, y)$ is a horizontal plan form satisfying $\Delta^* g = -a^2 g$, (4.2.6) becomes

$$\begin{aligned} \left(\xi D^2 - a^2\right) W &= -Ra^2\Theta, \\ \left(D^2 - a^2\right) \Theta &= -Rf(z)W, \end{aligned} \quad (4.2.7)$$

where $D^2 = \partial^2/\partial z^2$ and a is the wavenumber.

This fourth order system for R was solved numerically by two entirely different methods. Firstly the compound matrix method was employed as described in Straughan [94], and appendix A.2. Secondly the Chebyshev-tau QZ-algorithm as advocated by Dongarra *et al.* [23], and outlined in chapter 2 and appendix A.1 was used. Without going into detail, the basics of both routines are now described for the system at hand.

For the compound matrix method, the vector $\mathbf{W}$ is defined as $\mathbf{W} = (W, W', \Theta, \Theta')^T$. Let $\mathbf{W}_1$ and $\mathbf{W}_2$ be independent solutions obtained by replacing the boundary condition at $z = 1$ by the initial conditions $\mathbf{W}_1(0) = (0, 1, 0, 0)^T$ and $\mathbf{W}_2(0) = (0, 0, 0, 1)^T$. We introduce the variables

$$\begin{aligned} y_1 &= W_1W_2' - W_2W_1', & y_2 &= W_1\Theta_2 - W_2\Theta_1, \\ y_3 &= W_1\Theta_2' - W_2\Theta_1', & y_4 &= W_1'\Theta_2 - W_2'\Theta_1, \\ y_5 &= W_1'\Theta_2' - W_2'\Theta_1', & y_6 &= \Theta_1\Theta_2' - \Theta_2\Theta_1'. \end{aligned}$$

Then the compound matrix equations for (4.2.7) are

$$\begin{aligned} y_1' &= -\frac{a^2}{\xi} R y_2, \qquad y_2' = y_3 + y_4, \\ y_3' &= y_5 + a^2 y_2, \qquad y_4' = y_5 + \frac{a^2}{\xi} y_2, \\ y_5' &= a^2 \left(\frac{1}{\xi} y_3 + y_4 \right) + R \left(f(z) y_1 - \frac{a^2}{\xi} y_6 \right), \\ y_6' &= R f(z) y_2. \end{aligned} \tag{4.2.8}$$

This system was numerically integrated subject to the initial condition $y_5(0) = 1$. The value of R was varied such that the condition $y_2(1) = 0$ was satisfied to a predefined accuracy. Furthermore, we minimised over a^2 to find the critical Rayleigh number which is denoted by R_L^2 henceforth.

Chebyshev-tau D and D^2 routines were also implemented to solve (4.2.7). First, the solutions W and Θ are expanded in a series of Chebyshev polynomials

$$W = \sum_{n=0}^{N} w_n T_n(z), \qquad \Theta = \sum_{n=0}^{N} \theta_n T_n(z).$$

The second order differentiation operator obtained from writing out $\partial^2/\partial z^2$ in the Chebyshev representation is denoted by D^2. The boundary conditions for (4.2.7) are imposed by removing rows from the D^2 matrix. Furthermore, let Z denote the Chebyshev matrix represention of the function z (see chapter 2). Then, the resulting generalised eigenvalue problem is

$$\begin{pmatrix} 4\xi D^2 - a^2 I & 0 \\ 0 & 4D^2 - a^2 I \end{pmatrix} \begin{pmatrix} \mathbf{W} \\ \Theta \end{pmatrix} = R \begin{pmatrix} 0 & -a^2 I \\ \epsilon I + \frac{1}{2} Z & 0 \end{pmatrix} \begin{pmatrix} \mathbf{W} \\ \Theta \end{pmatrix}, \tag{4.2.9}$$

where $\mathbf{W} = (w_o, ..., w_N)^T$ and $\Theta = (\theta_o, ..., \theta_N)^T$. The matrix system was solved using the QZ algorithm. The critical Rayleigh number is approximated by the square of the smallest generalised eigenvalue of (4.2.9). A Chebyshev tau D method, as described in chapter 2, was also employed as an independent check. A presentation of the numerical results is delayed until section 4.5. For the moment however, we remark that excellent agreement was found between the three aforementioned numerical methods.

4.3 Global Nonlinear Stability via the Energy Method

Consider the nonlinear system (4.1.6)

$$\begin{aligned} \pi_{,i} &= -M_{ij}u_j + Rk_i\theta, \\ u_{i,i} &= 0, \\ \theta_{,t} + u_i\theta_{,i} &= Rf(z)w + \Delta\theta, \end{aligned} \tag{4.3.1}$$

with boundary conditions

$$u_3(0) = u_3(1) = 0, \qquad \theta(0) = \theta(1) = 0.$$

Multiplying equation $(4.3.1)_1$ by u_i, $(4.3.1)_3$ by θ and integrating both equations over V, yields

$$\begin{aligned} &R\langle\theta w\rangle - \langle M_{ij}u_iu_j\rangle = 0, \\ &\frac{d}{dt}\left(\frac{1}{2}\|\theta\|^2\right) - R\langle f(z)w\theta\rangle + \|\nabla\theta\|^2 = 0. \end{aligned} \tag{4.3.2}$$

Consider the thermal energy of the perturbations

$$E(t) = \frac{1}{2}\|\theta\|^2.$$

Multiplying $(4.3.2)_1$ by some coupling parameter λ (> 0) and adding this expression to $(4.3.2)_2$, the following relation is obtained

$$\frac{dE}{dt} = RI + D,$$

where the sign indefinite and definite terms are respectively,

$$I = \langle (f(z) + \lambda)\, w\theta\rangle, \qquad D = \|\nabla\theta\|^2 + \lambda\langle M_{ij}u_iu_j\rangle.$$

Next, R_E is defined by

$$\frac{1}{R_E} = \max_{\mathcal{H}} \frac{I}{D},$$

where $\mathcal{H}$ is the space of admissible solutions over which we seek a maximum, namely,

$$\mathcal{H} = \{u_i, \theta \in C^2(0,1) | u_3 = \theta = 0 \quad \text{when} \quad z = 0, 1\}.$$

This definition leads to the following relation

$$\frac{dE}{dt} \leq -D\left(\frac{R_E - R}{R_E}\right). \tag{4.3.3}$$

Using Poincaré's inequality (appendix B.1) and the fact that M_{ij} is positive definite, it can be shown that

$$D \geq \pi^2 \|\theta\|^2 = 2\pi^2 E. \tag{4.3.4}$$

Then using (4.3.4) it can be deduced from (4.3.3) that

$$\frac{dE}{dt} \leq -2\pi^2 a E \qquad \Rightarrow \qquad E(t) \leq E(0) e^{-2\pi^2 a t},$$

where $a = (R_E - R)/R_E$. So for all $R < R_E$, $E(t) \to 0$ as $t \to \infty$, where convergence is at least exponential. Hence R_E provides a global nonlinear stability bound.

To find the Euler-Lagrange equations for the maximum, a calculus of variations technique is employed as follows. Suppose θ and u_i are the maximising solutions and consider $\theta + \bar{\epsilon}\eta$ and $u_i + \bar{\epsilon} v_i$, where η and v_i are arbitrary functions which satisfy the same boundary conditions as θ and u_i respectively, and $\bar{\epsilon}$ is some constant. It can be easily shown (cf. (1.5)) that the maximising solution satisfies

$$R_E \delta I - \delta D = 0, \tag{4.3.5}$$

where

$$\delta I = \frac{dI}{d\bar{\epsilon}}\Big|_{\bar{\epsilon}=0}, \qquad \delta D = \frac{dD}{d\bar{\epsilon}}\Big|_{\bar{\epsilon}=0}.$$

Substituting $\theta + \bar{\epsilon}\eta$ and $u_i + \bar{\epsilon} v_i$ into (4.3.5) it can be deduced that

$$\int_V \left[R_E \left(f(z) + \lambda\right)\left(w\eta + v_3\theta\right) - \lambda M_{ij}\left(u_i v_j + v_i u_j\right) + 2\eta\Delta\theta\right] d\mathbf{x} = 0. \tag{4.3.6}$$

Apart from the continuity and boundary conditions they must satisfy, η and v_i are arbitrary functions. Therefore adding the zero term $\int_V \pi_{,i} v_i d\mathbf{x} = 0$ in (4.3.6), and letting $\eta = 0$ in the first instance, and $v_i = 0$ in the second yields the Euler-Lagrange equations

$$\begin{aligned} \pi_{,i} &= R_E \left(f(z) + \lambda\right)\theta k_i - 2\lambda M_{ij} u_j, \\ 2\Delta\theta &= -R_E \left(f(z) + \lambda\right) w. \end{aligned} \tag{4.3.7}$$

The Lagrangian multiplier π in $(4.3.7)_1$ can be eliminated by taking the curlcurl of both sides. Setting $i = 3$ and introducing normal modes yields the system

$$\begin{aligned} 2\lambda\left(\xi D^2 - a^2\right) W &= -R_E \left(f(z) + \lambda\right) a^2 \Theta, \\ 2\left(D^2 - a^2\right)\Theta &= -R_E \left(f(z) + \lambda\right) W, \end{aligned} \tag{4.3.8}$$

with boundary conditions $W = \Theta = 0$, for $z \in \{0, 1\}$.

The compound matrix equations for (4.3.8) are

$$\begin{aligned}
y_1' &= -R_E \frac{a^2(f(z)+\lambda)}{2\lambda\xi} y_2, & y_2' &= y_3 + y_4, \\
y_3' &= y_5 + a^2 y_2, & y_4' &= y_5 + \frac{a^2}{\xi} y_2, \\
y_5' &= a^2\left(\frac{1}{\xi} y_3 + y_4\right) + R_E\left(\frac{f(z)+\lambda}{2} y_1 - \frac{a^2(f(z)+\lambda)}{2\lambda\xi} y_6\right), \\
y_6' &= R_E \frac{f(z)+\lambda}{2} y_2.
\end{aligned}$$

This system was solved in an entirely analogous fashion to (4.2.8), i.e. subject to $y_5(0) = 1$ and $y_2(1) = 0$ and minimised over a^2. This time however, we also maximised over the coupling parameter λ to make R_E as large as possible. When maximising over λ, it is important to have a reasonable initial guess. It is worth noting at this point that it is expedient to put $\hat{u}_j = \sqrt{\lambda} u_j$ and $\hat{\pi}_j = \pi_j/\sqrt{\lambda}$ in (4.3.7). Then, with

$$g(z, \lambda) = \frac{f(z)+\lambda}{\sqrt{\lambda}},$$

the Euler-Lagrange equations become (dropping the hats)

$$\begin{aligned}
\pi_{,i} &= R_E g \theta k_i - 2M_{ij} u_j, \\
2\Delta\theta &= -R_E g w.
\end{aligned} \tag{4.3.9}$$

By employing parametric differentiation it may be shown that

$$\left\langle \left(R_E \frac{\partial g}{\partial \lambda} + g \frac{\partial R_E}{\partial \lambda} \right) \theta w \right\rangle = 0.$$

At the best value of λ, $\partial R_E/\partial\lambda = 0$, so we set $\partial g/\partial\lambda = 0$ to obtain a good guess for λ to be $-\epsilon$ (> 0).

The Chebyshev-tau D^2 system for (4.3.8) is

$$\begin{pmatrix} 8\lambda\xi D^2 - 2\lambda a^2 I & 0 \\ 0 & 8D^2 - 2a^2 I \end{pmatrix} \begin{pmatrix} \mathbf{W} \\ \mathbf{\Theta} \end{pmatrix} = R_E \begin{pmatrix} 0 & a^2\left((\epsilon - \lambda)I + \frac{1}{2}Z\right) \\ (\epsilon - \lambda)I + \frac{1}{2}Z & 0 \end{pmatrix} \begin{pmatrix} \mathbf{W} \\ \mathbf{\Theta} \end{pmatrix}.$$

This system was solved numerically and the results used to check those obtained by the compound matrix method. Again, excellent agreement was found.

4.4 Comparison of the Heat Sink Model with a Quadratic Density Model

An alternative way to model penetrative convection in the porous medium is via a quadratic density profile. Consider a porous medium like before, but now fix the temperature at the lower boundary at 0°C and maintain the temperature at the upper boundary at T_1 (> 0°C). Let the density have a quadratic temperature dependence of the form

$$\rho(T) = \rho_o \left[1 - \alpha \left(T - T_o\right)^2\right].$$

Then the governing equations are, cf. Straughan & Walker [96],

$$\begin{aligned} p_{,i} &= -\mu M_{ij} v_j + \rho_o \alpha g k_i \left(T^2 - 2T_o T\right), \\ v_{i,i} &= 0, \\ T_{,t} + v_i T_{,i} &= \kappa \Delta T. \end{aligned} \tag{4.4.1}$$

The basic steady state solutions of (4.4.1) are

$$\bar{v}_i = 0, \qquad \bar{T} = \beta z,$$

where $\beta = T_1/d$. Introducing perturbations (u_i, θ, π) to the velocity, temperature and pressure and non-dimensionalising with scalings of

$$X = d, \qquad \mathcal{T} = \frac{d^2}{\kappa}, \qquad U = \frac{\kappa}{d}, \qquad P = \mu\kappa, \qquad \left(T^{\#}\right)^2 = \frac{\kappa\mu\beta}{2\alpha\rho_o g T_1},$$

leads to

$$\begin{aligned} \pi_{,i} &= -M_{ij} u_j - R_{T^2} \left(\eta - z\right) k_i \theta + \frac{1}{2}\theta^2 k_i, \\ u_{i,i} &= 0, \\ \theta_{,t} + u_i \theta_{,i} &= -R_{T^2} w + \Delta\theta, \end{aligned} \tag{4.4.2}$$

where $\eta = T_o/T_1$, and the Rayleigh number is defined as

$$R_{T^2}^2 = T_1^2 \, \frac{2\rho_o \alpha g d}{\mu\kappa}.$$

The boundary conditions for this system are $u_3 = \theta = 0$, for $z \in \{0, 1\}$. Since we want to compare this system to the heat sink model, we choose $T_1^2 = -Qd^2/2\kappa$, to give the Rayleigh number the same interpretation as before (see (4.1.7)).

Neglecting the nonlinear terms in (4.4.2) and assuming a temporal growth rate like $e^{\sigma t}$, yields

$$\begin{aligned} \pi_{,i} &= -M_{ij}u_j - R\,(\eta - z)\,k_i\theta, \\ u_{i,i} &= 0, \\ \sigma\theta &= -Rw + \Delta\theta. \end{aligned} \tag{4.4.3}$$

To show that system (4.4.3) is adjoint to that described in (4.2.1) an analysis very similar to the one given by Tracey [99] for a fluid layer is performed.

Let $\mathbf{\Phi} = (\pi, u, v, w, \theta)^{\mathbf{T}}$, where v is the **j**-component of **u**. If we identify θ with $-\theta$ in the heat sink model, the two systems (4.2.1) and (4.4.3) can be written as $A_Q\mathbf{\Phi} = \sigma B\mathbf{\Phi}$ (heat sink) and $A_{T^2}\mathbf{\Phi} = \sigma B\mathbf{\Phi}$ (quadratic density law) respectively, where the operators A_Q and A_{T^2} are defined by

$$A_Q = \begin{pmatrix} 0 & \frac{\partial}{\partial x} & \frac{\partial}{\partial y} & \frac{\partial}{\partial z} & 0 \\ \frac{\partial}{\partial x} & M_{11} & 0 & 0 & 0 \\ \frac{\partial}{\partial y} & 0 & M_{22} & 0 & 0 \\ \frac{\partial}{\partial z} & 0 & 0 & M_{33} & R \\ 0 & 0 & 0 & f(z)R & \Delta \end{pmatrix},$$

$$A_{T^2} = \begin{pmatrix} 0 & \frac{\partial}{\partial x} & \frac{\partial}{\partial y} & \frac{\partial}{\partial z} & 0 \\ \frac{\partial}{\partial x} & M_{11} & 0 & 0 & 0 \\ \frac{\partial}{\partial y} & 0 & M_{22} & 0 & 0 \\ \frac{\partial}{\partial z} & 0 & 0 & M_{33} & (\eta - z)R \\ 0 & 0 & 0 & R & \Delta \end{pmatrix},$$

and

$$B = \begin{pmatrix} 0 & \dots & 0 \\ \vdots & \ddots & \vdots \\ 0 & \dots & I \end{pmatrix}.$$

Now, let $\mathbf{\Phi_1}$ and $\mathbf{\Phi_2}$ be independent. It is not difficult to show that $\langle A_Q\mathbf{\Phi_1}, \mathbf{\Phi_2}\rangle = \langle \mathbf{\Phi_1}, A_{T^2}\mathbf{\Phi_2}\rangle$ iff $f(z) = \eta - z$, i.e. $\epsilon = 1/2 - 4/T_1$. For this choice $A_{T^2} = A_Q^*$ (where A_Q^* is the adjoint of A_Q), implying that the two linearised models have the same eigenvalues and hence give rise to the same instability boundary. Putting $\sigma = 0$ and assuming a

normal mode representation, (4.4.3) can be rewritten as follows

$$\begin{aligned} \left(\xi D^2 - a^2\right) W &= a^2 R(\eta - z)\Theta, \\ \left(D^2 - a^2\right)\Theta &= RW. \end{aligned} \tag{4.4.4}$$

The Chebyshev tau D^2 method applied to (4.4.4) gives the following generalised eigenvalue system

$$\begin{pmatrix} 4\xi D^2 - a^2 I & 0 \\ 0 & 4D^2 - a^2 I \end{pmatrix} \begin{pmatrix} \mathbf{W} \\ \Theta \end{pmatrix} = R \begin{pmatrix} 0 & a^2\left(\left(\eta - \frac{1}{2}\right) I - \frac{1}{2} Z\right) \\ I & 0 \end{pmatrix} \begin{pmatrix} \mathbf{W} \\ \Theta \end{pmatrix}.$$

It was found (as expected) that this system yields exactly the same critical Rayleigh numbers as those obtained from the linear analysis using the heat sink model.

4.5 Numerical Results and Conclusions

In this section, subscript L will be used for results from the linear analysis (section 4.2), while E will indicate results obtained via the energy method (section 4.3). In tables 4.1 and 4.2, results are generated using the compound matrix method and checked via the Chebyshev-tau QZ routine. For the precision used in the tables, no significant difference could be found between the two sets of results and so only a presentation of the results obtained via the compound matrix method is given.

Table 4.1 displays the critical values (R_L, R_E, a_L^2, a_E^2) for the upper temperature, T_1 fixed and the anisotropy parameter ξ varying. T_1 is fixed at 4°C in the quadratic density model, which corresponds to a value of $\epsilon = -1/2$ in the heat sink model. For all values of ξ in the table we found $\lambda \approx 0.54$, which is reasonably close to its estimated value of $-\epsilon$. We conclude from table 4.1 that for this parameter range, the critical values obtained from the linear analysis are very close to those obtained via the energy analysis i.e. the linear instability and nonlinear stability thresholds are very close. Hence the linear results give a good physical representation of what is happening and it is unlikely that subcritical instabilities exist. However it is worth noting at this point that as ξ increases the agreement between the linear and nonlinear results is not as good as it is for smaller values of ξ. We

ξ	R_L	R_E	a_L^2	a_E^2
0.2	6.34800	6.29303	4.58564	4.61381
0.4	7.16423	7.10451	6.46601	6.49883
0.6	7.78941	7.72536	7.91138	7.94873
0.8	8.31594	8.24790	9.13197	9.17390
1.0	8.77950	8.70776	10.2090	10.2555
2.0	10.5962	10.5086	14.4496	14.5197
3.0	11.9886	11.8878	17.7190	17.8129
5.0	14.1946	14.0716	22.9282	23.0691

Table 4.1: Critical parameters of linear instability and nonlinear stability with $T_1 = 4°C$.

also observe that as ξ increases the Rayleigh number increases too. This implies that the system becomes more stable as ξ increases. The most interesting behaviour in table 4.1 however, is that as ξ increases, the wavenumber increases quite rapidly. This suggests that the convection cells are becoming narrower as the permeability in the z direction is increased.

In table 4.2, ξ is kept fixed while ϵ (and thus T_1) is varied. Note that as T_1 increases from 1°C to 8°C, ϵ tends to zero. Physically, as T_1 is increased in the quadratic density model, we could say that in the heat sink model Q becomes stronger, while the boundary conditions remain fixed. The critical Rayleigh number increases with T_1, and thus the system becomes more stable as the upper temperature is increased. This is expected and in good agreement with Straughan & Walker [96]. Note that for ϵ close to zero, the linear results do not agree with the nonlinear results quite so well. In particular, the differences in the wavenumber become larger. We also note, that as T_1 increases the estimated value of λ is not as good.

Figure 4.2 shows the Chebyshev expansion of $W(z)$ for the first 30 polynomials in the isotropic case. The approximation is based on the quadratic density model. We only show profiles obtained with this model because the physical interpretation of the results obtained with the heat sink model was not clear. Although for systems (4.2.7) and (4.4.4) the eigenvalues are the same, the eigenvectors are not (cf. chapter 3). Since the quadratic density model provides a more tangible representation, we present these results and high-

T_1(°C)	ϵ	R_L	R_E	a_L^2	a_E^2	λ
1.0	−3.500000	3.35766	3.35702	9.87671	9.87831	3.50618
2.0	−1.500000	5.12318	5.11797	9.90824	9.91653	1.51434
3.0	−0.833333	6.85262	6.83077	9.99394	10.0177	0.858793
4.0	−0.500000	8.77950	8.70776	10.2090	10.2555	0.541011
5.0	−0.300000	11.1114	10.9037	10.7667	10.7905	0.363036
6.0	−0.166667	14.0823	13.5485	12.3140	11.9279	0.259922
7.0	−0.071429	17.7073	16.6903	16.1375	14.0611	0.201908
8.0	−0.000001	21.7114	20.2574	21.8574	17.3643	0.169258

Table 4.2: Critical parameters of linear instability and nonlinear stability with $\xi = 1$.

light the need for caution when interpreting results found via the heat sink model. For T_1 less than or equal to 6°C, $W(z)$ is positive for all z. In this case there is only one convection cell, the centre of which is located at the maximum of $W(z)$. For T_1 greater than or equal to 7°C however, $W(z)$ changes sign indicating the existence of a counter cell and hence the onset of penetrative convection. As T_1 increases from 7°C to 7.9°C, the boundary layer effect near $z = 0$ and the second cell become stronger.

Figure 4.3 shows the Chebyshev expansion of $\Theta(z)$ for the first 30 polynomials, again in the isotropic quadratic density case. In this instance there is no sign change and the isotherms are in agreement with those presented in Moore & Weiss [63].

In table 4.3 the range in which T_1^{crit}, the temperature at which penetrative convection starts, is for ξ varying is presented. It has already been concluded that the system becomes more stable as both ξ and T_1 increase. The behaviour seen in table 4.3 agrees with this, since it clearly shows that for higher values of ξ a higher value of T_1 is needed for the onset of penetrative convection .

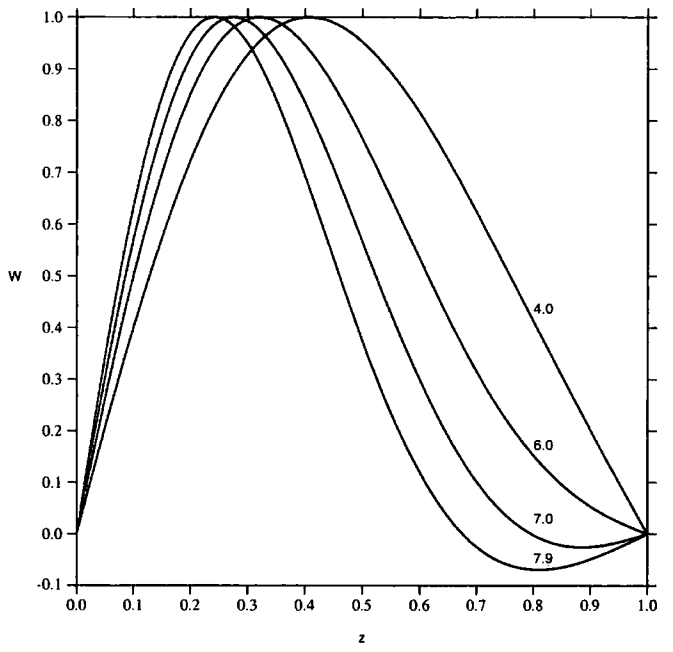

Figure 4.2: Profile of $W(z)$ normalised over the spatial layer, $\xi = 1$, T_u varies as shown on graph.

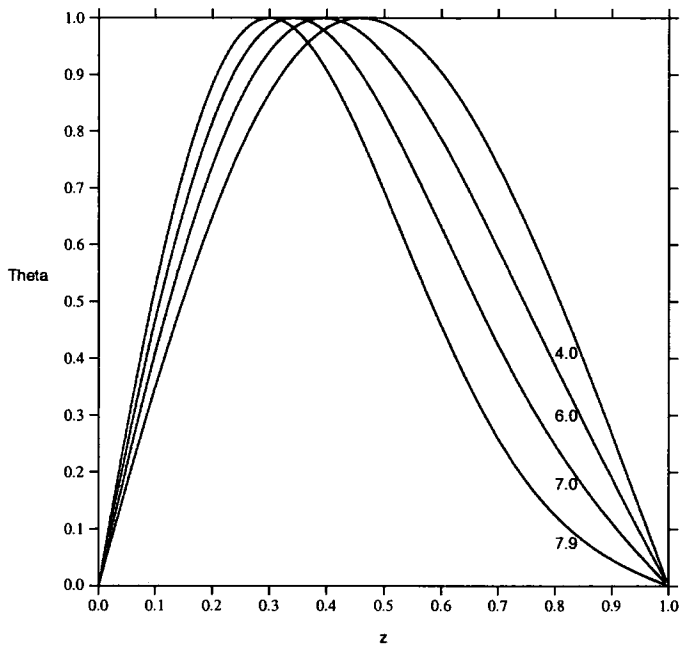

Figure 4.3: Profile of $\Theta(z)$ normalised over the spatial layer, $\xi = 1$, T_u varies as shown on graph.

ξ	Interval for T_1^{crit}
0.25	$(5.90, 5.95)$
0.50	$(6.20, 6.25)$
0.75	$(6.35, 6.40)$
1.00	$(6.45, 6.50)$
1.25	$(6.55, 6.60)$
1.50	$(6.65, 6.70)$
1.75	$(6.70, 6.75)$
2.00	$(6.80, 6.85)$
3.00	$(7.00, 7.05)$
5.00	$(7.30, 7.35)$

Table 4.3: The interval in which T_1 yields penetrative convection.

Chapter 5

A Model for Convection in the Evolution of Under-ice Melt Ponds

In this chapter a model for convection in the evolution of under-ice melt ponds is presented. The evolution of under-ice melt ponds was first explained by Martin & Kauffman [59]. They modelled the phenomenon observed in the summer Arctic, where a layer of fresh water at a temperature of approximately $0°C$, lies under a layer of ice and over a much colder ($\approx -1.6°C$), denser layer of salt water. In this scenario the fresh water layer is convectively unstable since the fresh water diffuses heat to the salt water causing a density inversion. The supercooled water rises to the overlying ice surface at which point it nucleates into thin vertical interlocking ice crystals. These grow down to the salt water interface and then a lateral crystal growth begins and continues until a horizontal ice sheet forms, trapping fresh water above and forming a so called under-ice melt pond.

The formation of under-ice melt ponds are an important factor in sea ice melting. In recent literature much attention has been paid to fast sea ice melting and the factors affecting it. For example Bogorodskii & Nagurnyi [9] showed that under-ice melt ponds favour melting in the lower boundary of sea ice. This has important applications in global and regional climate modelling. Schmittner *et al.* [87] argued that active ice sheets offer an explanation for the forcing mechanism behind rapid warming events. Rahmstorf [81] also remarked that the nonlinear dynamics of ice sheets can cause abrupt climatic change. A comprehensive summary of theoretical glaciology can be found in Hutter [40] and a detailed study of the thermomechanical behaviour of large ice sheets and their relation to

climate variations in Baral *et al.* [4]. Such work and the references therein highlight the need for accurate models. Indeed Clark *et al.* [19] commented that more realistic models of the hydrological cycle (precipitation, run-off, iceberg discharge, sea ice) are urgently needed to understand the role of thermohaline circulation in abrupt climate change.

It is the aim of this chapter to accurately model the first stage in the formation of under-ice melt ponds, i.e. the onset of convection in the unstable fresh water layer. Bogorodskii & Nagurnyi [9] presented a model for the same situation. In their work however they also took into account the layer of melt water overlying the ice layer and treat the system as a unified one. They argued from physical considerations that all layers should lose stability simultaneously and so restricted their attention to solving the problem for the upper layer only and then used a symmetry argument to consider the system as a whole. They found that the major parameters affecting stability were the thickness of the ice and coefficients of heat conductivity. In this chapter we employ a different model and find that $-T_l$, the temperature of the salt water, and τ, the ratio of the heat diffusivity to solute diffusivity, are also major parameters affecting stability.

One of the important aspects in the evolution of under-ice melt ponds is the fact that the layers of fresh water and salt water remain separated. This is due to double diffusion. Density increases with supercooling for solutions with salinity $> 23^\circ/_{\circ\circ}$ but decreases for solutions with salinity $< 23^\circ/_{\circ\circ}$, cf. Martin & Kauffman [59]. The salinty of surface sea water ranges from $26 - 28^\circ/_{\circ\circ}$ in the Arctic to $34^\circ/_{\circ\circ}$ in the Antarctic. Hence for the model in hand, the temperature and salt fields exhibit competing behaviour. It is widely known that the competing effects in double diffusion mean that the linear instability bound does not always capture the physics of instability and subcritical instabilities may arise, cf. Hansen & Yuen [39], Proctor [79], and Shir & Joseph [90]. It is very important therefore, to obtain global nonlinear stability thresholds which guarantee bounds below which convection cannot occur. In this chapter we find both the linear instability and global nonlinear stability thresholds and present the subcritical region bounded by these two limits.

In this chapter we choose a density profile with quadratic temperature dependence and linear concentration dependence. As a result the standard energy technique does not yield a global stability bound. Therefore a weighted technique as introduced in Payne &

Straughan [76] is used. The two competing effects demand two coupling parameters cf. Straughan [94]. We find that the unweighted coupling parameter has a critical value such that the nonlinear stability bound is independent of the salt field.

An outline of this chapter is as follows. We begin by formulating a governing model and describe a density field which allows for thermal convection and double diffusion. We then find an instability bound for the linearised system and a global stability bound for the nonlinear system. Finally we present the numerical results and discuss their implications in modelling under-ice melt ponds.

5.1 Governing Equations

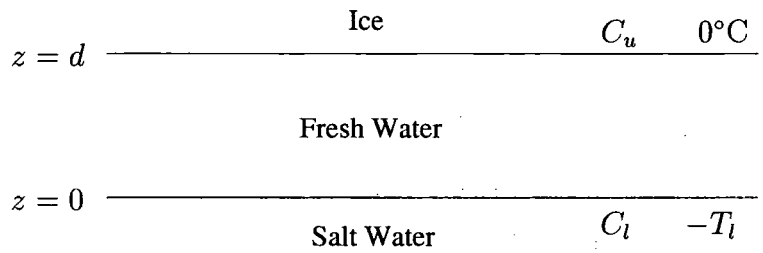

Figure 5.1: Schematic diagram of the governing system.

Consider a layer of water lying in the infinite three-dimensional region $0 < z < d$, sandwiched between a layer of salt water at $z = 0$ and a layer of ice at $z = d$. The upper and lower planes are held fixed at temperatures 0°C and $-T_l (< 0°\text{C})$, and concentrations C_u and C_l respectively, see figure 5.1. Suppose that the layer of water has a salt concentration less than that in the layer of salt water lying below. This system is in a potentially gravitationally unstable state since the warmer water at the upper boundary is denser than that at the lower with respect to temperature. However the water at $z = 0$ is saltier than that at $z = d$ and so denser with respect to the salt field. Hence in this situation we have two competing effects, a temperature gradient which is destabilising and a salt one which is stabilising. The z direction is denoted by the vector $\mathbf{k}$ with $\mathbf{i}, \mathbf{j}, \mathbf{k}$ being the standard Cartesian basis. Gravity acts in the negative z direction and we assume that the density ρ is constant, everywhere except the body force. Then, the Navier-Stokes equation for the

fluid motion are

$$v_{i,t} + v_j v_{i,j} = -\frac{1}{\rho_o} p_{,i} + \nu \Delta v_i - \frac{1}{\rho_o} g\rho(T, C) k_i, \tag{5.1.1}$$

where v_i, t, p, ν, g, T, and C are velocity, time, pressure, kinematic viscosity, gravity, temperature and concentration respectively and ρ the density, is assumed to be of the form

$$\rho(T, C) = \rho_o\big[1 - \alpha(T-4)^2 + A(C - \hat{C})\big], \tag{5.1.2}$$

where α and A are the thermal and solute expansion coefficients respectively, and $\hat{C}$ and ρ_o are some constant reference values. Standard indicial notation and the Einstein summation convention are employed throughout, and $\mathbf{k} = (0, 0, 1)^T$. The constant term in (5.1.2) is absorbed into the pressure by defining a modified pressure $\hat{p}$ to be $p + g\rho_o(1 - 16\alpha - A\hat{C})z$. Then, dropping the hat, (5.1.1) becomes

$$v_{i,t} + v_j v_{i,j} = -\frac{1}{\rho_o} p_{,i} + \nu \Delta v_i + g k_i\big[\alpha(T^2 - 8T) - AC\big]. \tag{5.1.3}$$

Equation (5.1.3) together with the incompressibility condition and the equations of energy and solute balance yield the following system of governing equations

$$\begin{aligned} &v_{i,t} + v_j v_{i,j} = -\frac{1}{\rho_o} p_{,i} + \nu \Delta v_i + g k_i\big[\alpha(T^2 - 8T) - AC\big], \\ &v_{i,i} = 0, \\ &T_{,t} + v_i T_{,i} = \kappa \Delta T, \\ &C_{,t} + v_i C_{,i} = \kappa_c \Delta C, \end{aligned} \tag{5.1.4}$$

where κ and κ_c are thermal diffusivity and solute diffusivity, respectively.

The boundary conditions are

$$\begin{aligned} T &= 0°\text{C}, \qquad C = C_u \qquad \text{at} \quad z = d, \\ T &= -T_l, \qquad C = C_l \qquad \text{at} \quad z = 0, \end{aligned} \tag{5.1.5}$$

where T_l, C_u, C_l are prescribed constant fields and $C_l > C_u$ and $T_l > 0°\text{C}$. Under these conditions, the basic steady state solution of (5.1.4) whose stability is to be investigated, is

$$\bar{v}_i = 0, \qquad \bar{T} = \frac{zT_l}{d} - T_l, \qquad \bar{C} = -\gamma z + C_l,$$

where

$$\gamma = \frac{C_l - C_u}{d} > 0.$$

The hydrostatic pressure $\bar{p}$ may be found from $(5.1.4)_1$ but since $\bar{p}$ is eliminated from our analysis later on, a derivation of it is not included here.

To study the stability of (5.1.4) perturbations to the steady state solutions are introduced as follows

$$v_i = \bar{v}_i + u_i, \qquad T = \bar{T} + \theta, \qquad p = \bar{p} + \pi, \qquad C = \bar{C} + \phi.$$

The perturbed expressions are substituted into (5.1.4) and non-dimensionalised with scalings of

$$X = d, \qquad \mathcal{T} = \frac{d^2}{\nu}, \qquad U = \frac{\nu}{d}, \qquad P = \frac{\rho_o \nu^2}{d^2},$$
$$\left(T^{\#}\right)^2 = \frac{\nu^3}{\kappa \alpha g d^3}, \qquad \left(C^{\#}\right)^2 = \frac{(C_l - C_u)\nu^3}{\kappa_c A g d^3},$$

for displacement, time, velocity, pressure, temperature and concentration respectively. Then (5.1.4) may be rewritten in terms of the non-dimensional perturbation quantities

$$\begin{aligned} &u_{i,t} + u_j u_{i,j} = -\pi_{,i} + \Delta u_i - 2RM(z)\theta k_i + Pr\theta^2 k_i - R_c \phi k_i, \\ &u_{i,i} = 0, \\ &Pr(\theta_{,t} + u_i \theta_{,i}) = \Delta\theta - Rw, \\ &Sc(\phi_{,t} + u_i \phi_{,i}) = \Delta\phi + R_c w, \end{aligned} \tag{5.1.6}$$

where

$$M(z) = \xi - z, \qquad \xi = \frac{T_l + 4}{T_l}, \qquad w = u_3, \qquad \mathbf{x} \in \mathbb{R}^2 \times (0,1),$$

and

$$R^2 = \frac{T_l^2 \alpha g d^3}{\nu \kappa}, \qquad R_c^2 = \frac{A g \gamma d^4}{\kappa_c \nu}, \qquad Pr = \frac{\nu}{\kappa}, \qquad Sc = \frac{\nu}{\kappa_c},$$

define the Rayleigh, solute Rayleigh, Prandtl and Schmidt numbers. The boundary conditions for the perturbed variables are

$$w(0) = w(1) = 0, \qquad \theta(0) = \theta(1) = 0, \qquad \phi(0) = \phi(1) = 0,$$

and it can be deduced from $(5.1.6)_2$ that

$$w_{,z}(0) = w_{,z}(1) = 0.$$

5.2 Linearised Instability Theory

Neglecting the nonlinear terms in (5.1.6) and assuming a temporal growth rate like $e^{\sigma t}$ we obtain the linearised system

$$\begin{aligned} \sigma u_i &= -\pi_{,i} + \Delta u_i - 2RM(z)\theta k_i - R_c\phi k_i, \\ u_{i,i} &= 0, \\ \sigma Pr\theta &= \Delta\theta - Rw, \\ \sigma Sc\phi &= \Delta\phi + R_c w. \end{aligned} \tag{5.2.1}$$

To eliminate the pressure in $(5.2.1)_1$, we take the curlcurl of both sides. Then, setting $i = 3$, we obtain

$$\sigma\Delta w = \Delta^2 w - 2RM(z)\Delta^*\theta - R_c\Delta^*\phi, \tag{5.2.2}$$

where Δ^* is the horizontal Laplacian, $\Delta^* = \partial^2/\partial x^2 + \partial^2/\partial y^2$. Assuming a normal mode representation for w, θ and ϕ, of the form $w = W(z)g(x,y)$, $\theta = \Theta(z)g(x,y)$ and $\phi = \Phi(z)g(x,y)$ where $g(x,y)$ is some horizontal plan form satisfying $\Delta^* g = -a^2 g$, $(5.2.1)_{3,4}$ and (5.2.2) yield

$$\begin{aligned} \sigma(D^2 - a^2)W &= (D^2 - a^2)^2 W + 2RM(z)a^2\Theta + R_c a^2\Phi, \\ \sigma Pr\Theta &= (D^2 - a^2)\Theta - RW, \\ \sigma Sc\Phi &= (D^2 - a^2)\Phi + R_c W, \end{aligned} \tag{5.2.3}$$

where $D^2 = \partial^2/\partial z^2$ and a is the wave number. The corresponding boundary conditions are

$$W = DW = \Theta = \Phi = 0, \qquad \text{for } z \in \{0, 1\}. \tag{5.2.4}$$

This eighth order system for σ was solved by the Chebyshev tau D and D^2 algorithms as discussed in chapter 2 and appendix A.1. Without going into detail, the basics of the D^2 method are now briefly described and the interested reader referred to appendix A.1 and Dongarra *et al.* [23] for further details and an outline of the D method.

In the D^2 method, (5.2.3) is rewritten in terms of 2nd order derivatives only. Letting

$A = (D^2 - a^2)W$, (5.2.3) can be expressed as the four 2nd order equations

$$\begin{aligned}
&(D^2 - a^2)W - A = 0,\\
&(D^2 - a^2)A + 2RM(z)a^2\Theta + R_c a^2\Phi = \sigma A,\\
&(D^2 - a^2)\Theta - RW = \sigma Pr\Theta,\\
&(D^2 - a^2)\Phi + R_c W = \sigma Sc\Phi.
\end{aligned} \tag{5.2.5}$$

This system is then transformed onto the Chebyshev domain $(-1, 1)$ and the solutions W, A, Θ, and Φ treated as independent variables and expanded in a series of Chebyshev polynomials

$$W = \sum_{n=0}^{N} w_n T_n(z), \qquad A = \sum_{n=0}^{N} a_n T_n(z),$$
$$\Theta = \sum_{n=0}^{N} \theta_n T_n(z), \qquad \Phi = \sum_{n=0}^{N} \phi_n T_n(z).$$

The inner product of each equation is taken with some T_k and the orthogonality of the Chebyshev polynomials exploited to obtain the following generalised eigenvalue problem

$$\begin{pmatrix} 4D^2 - a^2 I & -I & 0 & 0 \\ 0 & 4D^2 - a^2 I & * & R_c a^2 I \\ -RI & 0 & 4D^2 - a^2 I & 0 \\ R_c I & 0 & 0 & 4D^2 - a^2 I \end{pmatrix} \begin{pmatrix} \mathbf{W} \\ \mathbf{A} \\ \mathbf{\Theta} \\ \mathbf{\Phi} \end{pmatrix}$$
$$= \sigma \begin{pmatrix} 0 & 0 & 0 & 0 \\ 0 & I & 0 & 0 \\ 0 & 0 & Pr & 0 \\ 0 & 0 & 0 & Sc \end{pmatrix} \begin{pmatrix} \mathbf{W} \\ \mathbf{A} \\ \mathbf{\Theta} \\ \mathbf{\Phi} \end{pmatrix}.$$

Here D^2 is the Chebyshev matrix representation of $\partial^2/\partial z^2$, $* = 2Ra^2(\xi - 1/2)I - Ra^2 Z$, Z is the Chebyshev matrix representation of z, $\mathbf{W} = (w_o, ..., w_N)^T$, $\mathbf{A} = (a_o, ..., a_N)^T$, $\mathbf{\Theta} = (\theta_o, ..., \theta_N)^T$ and $\mathbf{\Phi} = (\phi_o, ..., \phi_N)^T$. The last two rows of each $(N+1) \times (N+1)$ block are removed and replaced by the discrete form of the eight boundary conditions (5.2.4). The resulting system is solved for the eigenvalues $\sigma^{(n)}, n = 1, 2, \ldots$, via the QZ algorithm. A presentation of the numerical results is delayed until section 5.4. For the moment however, we remark that excellent agreement was found between the two aforementioned numerical methods.

5.3 Global Nonlinear Stability via the Weighted Energy Method

Consider the nonlinear system (5.1.6)

$$\begin{aligned} &u_{i,t} + u_j u_{i,j} = -\pi_{,i} + \Delta u_i - 2RM(z)\theta k_i + Pr\theta^2 k_i - R_c \phi k_i, \\ &u_{i,i} = 0, \\ &Pr(\theta_{,t} + u_i \theta_{,i}) = \Delta\theta - Rw, \\ &Sc(\phi_{,t} + u_i \phi_{,i}) = \Delta\phi + R_c w, \end{aligned} \tag{5.3.1}$$

with boundary conditions

$$w(0) = w(1) = 0, \qquad \theta(0) = \theta(1) = 0,$$

$$\phi(0) = \phi(1) = 0, \qquad w_{,z}(0) = w_{,z}(1) = 0.$$

Let V be some periodic cell and denote the L^2-inner product as follows

$$\langle uv \rangle = \int_V uv dV.$$

If the usual energy method is applied to (5.3.1), i.e. multiply equation $(5.3.1)_1$ by u_i, $(5.3.1)_3$ by θ, and $(5.3.1)_4$ by ϕ and then integrate all equations over V, a cubic nonlinearity $\langle w\theta^2 \rangle$ is obtained from $(5.3.1)_1$. To remove the cubic term and hence achieve a global nonlinear stability result, we use a weighted energy technique as described in Payne & Straughan [76].

First, multiply $(5.3.1)_1$ by u_i and integrate over V to obtain

$$\frac{d}{dt}\left(\frac{1}{2}\|\mathbf{u}\|^2\right) = -\|\nabla \mathbf{u}\|^2 - 2R\langle M(z)\theta w \rangle - R_c \langle \phi w \rangle + Pr\left\langle w\theta^2 \right\rangle. \tag{5.3.2}$$

A weight function is then introduced

$$\hat{\mu} = \mu - 2z,$$

where $\mu > 2$ is some constant coupling parameter chosen so that $\hat{\mu} > 0$. Using $(5.3.1)_3$ it can be deduced that

$$\frac{d}{dt}\left(\frac{Pr}{2}\int_V \hat{\mu}\theta^2 dV\right) = -Pr\left\langle w\theta^2 \right\rangle - \int_V \hat{\mu}\theta_{,i}\theta_{,i} dV - R\langle \hat{\mu}\theta w \rangle. \tag{5.3.3}$$

Finally, multiplying $(5.3.1)_4$ by ϕ and integrating over V yields

$$\frac{d}{dt}\left(\frac{1}{2}\|\phi\|^2\right) = -\frac{1}{Sc}\|\nabla\phi\|^2 + \frac{R_c}{Sc}\langle\phi w\rangle. \tag{5.3.4}$$

An energy, E, is defined as

$$E(t) = \frac{1}{2}\|\mathbf{u}\|^2 + \frac{Pr}{2}\int_V \hat{\mu}\theta^2 dV + \frac{\lambda}{2}\|\phi\|^2,$$

where $\lambda > 0$ is some constant coupling parameter. Then

$$\frac{dE}{dt} = I - D,$$

where

$$I = R_c\left(\frac{\lambda}{Sc} - 1\right)\langle\phi w\rangle - R\langle(2M(z) + \hat{\mu})\theta w\rangle,$$
$$D = \|\nabla\mathbf{u}\|^2 + \int_V \hat{\mu}\theta_{,i}\theta_{,i}dV + \frac{\lambda}{Sc}\|\nabla\phi\|^2.$$

Next, define R_E by

$$\frac{1}{R_E} = \max_{\mathcal{H}}\frac{I}{D},$$

where $\mathcal{H}$ is the space of admissible solutions, namely

$$\mathcal{H} = \{u_i, \theta, \phi \in C^2(0,1) | u_3 = \theta = \phi = 0 \quad \text{when} \quad z = 0, 1\}.$$

This definition leads to the following relation

$$\frac{dE}{dt} \leq -D\left(1 - \frac{1}{R_E}\right). \tag{5.3.5}$$

Using the fact that $z \in (0,1)$ we observe that

$$\hat{\mu} = \mu - 2z \quad \Rightarrow \quad \hat{\mu} \geq \mu - 2 \quad \text{and} \quad \frac{\hat{\mu}}{\mu} \leq 1.$$

Therefore using Poincaré's inequality (appendix B.1) and the information above, D can be bounded from below as follows

$$D \geq c_1\|\mathbf{u}\|^2 + c_2\frac{(\mu-2)}{\mu}\int_V \hat{\mu}\theta^2 dV + c_3\frac{\lambda}{Sc}\|\phi\|^2,$$

where c_1, c_2, c_3 are positive constants. It is easy to show then

$$D \geq cE, \tag{5.3.6}$$

where c is some positive constant dependent on μ, λ and Sc. Using (5.3.6), (5.3.5) can be rewritten as

$$\frac{dE}{dt} \leq -acE \quad \Rightarrow \quad E(t) \leq E(0)e^{-act}$$

where $a = 1 - 1/R_E$. So for all $R_E > 1$, $E(t) \to 0$ as $t \to \infty$, where convergence is at least exponential. Therefore, $R_E = 1$ provides a global nonlinear stability threshold.

Setting $R_E = 1$ and using a calculus of variations technique, the Euler-Lagrange equations for the maximum are found to be

$$\begin{aligned} &f(\lambda)R_c\Psi k_i - R\left(2M(z) + \hat{\mu}\right)\theta k_i + 2\Delta u_i = \pi_{,i}, \\ &- R\left(2M(z) + \hat{\mu}\right)w + 2\hat{\mu}\Delta\theta - 4\frac{\partial\theta}{\partial z} = 0, \\ &f(\lambda)R_c w + \frac{2}{Sc}\Delta\Psi = 0, \end{aligned} \tag{5.3.7}$$

where

$$f(\lambda) = \frac{\lambda/Sc - 1}{\sqrt{\lambda}}, \qquad \Psi = \sqrt{\lambda}\phi. \tag{5.3.8}$$

The Lagrange multiplier π in $(5.3.7)_1$ is eliminated by taking the curlcurl of both sides. Then, setting $i = 3$ and introducing normal modes $w = W(z)g(x,y), \theta = \Theta(z)g(x,y)$, and $\Psi = \Phi(z)g(x,y)$ gives

$$\begin{aligned} &2(D^2 - a^2)^2 W + Ra^2\hat{M}(z)\Theta - R_c a^2 f(\lambda)\Phi = 0, \\ &- R\hat{M}(z)W + 2\hat{\mu}(D^2 - a^2)\Theta - 4D\Theta = 0, \\ &f(\lambda)R_c W + \frac{2}{Sc}(D^2 - a^2)\Phi = 0, \end{aligned} \tag{5.3.9}$$

where $\hat{M}(z) = 2M(z) + \hat{\mu}$ and we have boundary conditions $W = DW = \Theta = \Phi = 0$, for $z \in \{0, 1\}$.

This eighth order system was solved numerically by both the compound matrix method and the Chebyshev tau D^2 method. The basics of the two routines are now briefly described for the system in hand.

For the compound matrix method, the vector $\mathbf{W}$ is defined as

$$\mathbf{W} = (W, W', W'', W''', \Theta, \Theta', \Phi, \Phi')^T.$$

Let $\mathbf{W}_1$, $\mathbf{W}_2$, $\mathbf{W}_3$, and $\mathbf{W}_4$ be independent solutions of (5.3.9) obtained by replacing the boundary condition at $z = 1$ by the initial conditions

$$\mathbf{W}_1(0) = (0,0,1,0,0,0,0,0)^T, \quad \mathbf{W}_2(0) = (0,0,0,1,0,0,0,0)^T,$$

$$\mathbf{W}_3(0) = (0,0,0,0,0,1,0,0)^T, \quad \mathbf{W}_4(0) = (0,0,0,0,0,0,0,1)^T.$$

A new seventy vector $\mathbf{Y} = (y_1, \ldots, y_{70})^T$ is formed from the 4×4 minors of the 8×4 solution matrix with columns $\mathbf{W}_1, \mathbf{W}_2, \mathbf{W}_3$, and $\mathbf{W}_4$. Using (5.3.9), seventy first order differential equations in terms of $y_1, \ldots, y_{70}$ are found and numerically integrated from 0 to 1. The boundary conditions on $\mathbf{W}$ are

$$W(0) = \Theta(0) = W^{'}(0) = \Phi(0) = 0,$$
$$W(1) = \Theta(1) = W^{'}(1) = \Phi(1) = 0.$$

We replace the conditions at $z = 1$ by

$$W_1^{''}(0) = W_2^{'''}(0) = \Theta_3^{'}(0) = \Phi_4^{'}(0) = 1.$$

Hence the appropriate initial and final conditions are (given the labelling used)

$$y_{60}(0) = 1, \qquad y_{11}(1) = 0. \tag{5.3.10}$$

R_c is fixed and the eigenvalue R varied until $y_{11}(1) = 0$ is satisfied to some preassigned tolerance. Keeping $a^2, \lambda > 0$, and $\mu > 2$, a golden section search routine was employed to numerically find

$$Ra_E = \max_{\lambda,\mu} \min_{a^2} R^2(a^2, \lambda, \mu). \tag{5.3.11}$$

When maximising over λ and μ, it is important to have initial guesses which are reasonably good. By using parametric differentiation on the Euler-Lagrange equations (5.3.7), fixing λ and varying $\hat{\mu}$ we may show that

$$R(2\xi - \mu) \int_V w\theta dV = 0,$$

and hence deduce an estimate for $\mu = 2\xi$. Similarly if we fix $\hat{\mu}$ and vary λ, parametric differentiation suggests a best value for $\lambda = -Sc$. This is unsatisfactory since we are assuming $\lambda > 0$. It is of interest to note at this point however, that in all numerical calculations we found $\lambda_{crit} = Sc$ (see section 5.4).

Suppose $\lambda = Sc$, then system (5.3.9) looses dependence on Φ and reduces to the sixth order system

$$\begin{aligned} &2(D^2 - a^2)^2 W + Ra^2 \hat{M}(z)\Theta = 0, \\ &-R\hat{M}(z)W + 2\hat{\mu}(D^2 - a^2)\Theta - 4D\Theta = 0, \end{aligned} \tag{5.3.12}$$

with boundary conditions $W = DW = \Theta = 0$, for $z \in \{0, 1\}$. This system was also solved via the compound matrix method and the results used to check the results of the eighth order system (5.3.9) when $\lambda = Sc$ (or $R_c = 0$).

To implement the Chebyshev tau D^2 method we begin by letting $A = (D^2 - a^2)W$. Then the eighth order system (5.3.9) can be rewritten as

$$\begin{aligned} &(D^2 - a^2)W - A = 0, \\ &2(D^2 - a^2)A - R_c a^2 f(\lambda)\Phi = -Ra^2 \hat{M}(z)\Theta, \\ &2\hat{\mu}(D^2 - a^2)\Theta - 4D\Theta = R\hat{M}(z)W, \\ &f(\lambda)R_c W + \frac{2}{Sc}(D^2 - a^2)\Phi = 0, \end{aligned} \tag{5.3.13}$$

with boundary conditions $W = DW = \Theta = \Phi = 0$, for $z \in \{0, 1\}$. To transform (5.3.13) onto the Chebyshev domain $(-1, 1)$, let $\hat{z} = 2z - 1$. Then dropping the hats (5.3.13) yields

$$\begin{aligned} &(4D^2 - a^2)W - A = 0, \\ &2(4D^2 - a^2)A - R_c a^2 f(\lambda)\Phi = -Ra^2 \bar{M}(z)\Theta, \\ &2\bar{\mu}(4D^2 - a^2)\Theta - 8D\Theta = R\bar{M}(z)W, \\ &f(\lambda)R_c W + \frac{2}{Sc}(4D^2 - a^2)\Phi = 0, \end{aligned} \tag{5.3.14}$$

where $\bar{M} = 2\xi + \mu - 2z - 2$, $\bar{\mu} = \mu - z - 1$ and now $z \in (-1, 1)$. Since $\bar{\mu}$ is a function of z we seek the Chebyshev matrix representation of zD^2. To construct this matrix we follow an analysis similar to that for the representation of z as given in section 2.5.1.

To find $(zD^2\Theta, T_k)$, we begin by noting the following,

$$\begin{aligned} zD^2\Theta &= T_1 \sum_{n=0}^{N+2} \theta_n T_n'' = \sum_{n=0}^{N+2} \theta_n T_1 T_n'' \\ &= 4T_1\theta_2 + 12(T_0 + T_2)\theta_3 + (56T_1 + 24T_3)\theta_4 + (60T_0 + 100T_2 + 40T_4)\theta_5 + \ldots. \end{aligned}$$

So, taking inner products with T_0, T_1, $T_2, \ldots, T_{N+2}$, and using the orthogonality of Chebyshev polynomials it can be deduced that,

$$\begin{aligned} &(zD^2\Theta, T_0) = 12\pi\theta_3 + 60\pi\theta_5 + \ldots, \quad (zD^2\Theta, T_1) = 2\pi\theta_2 + 28\pi\theta_4 + \ldots, \\ &(zD^2\Theta, T_2) = 6\pi\theta_3 + 50\pi\theta_5 + \ldots, \end{aligned}$$

which can be expressed in matrix form as,

$$\begin{pmatrix} 0 & 0 & 0 & 12 & 0 & 60 & 0 & \dots & 0 \\ 0 & 0 & 4 & 0 & 56 & 0 & 0 & \dots & 0 \\ 0 & 0 & 0 & 12 & 0 & 100 & 0 & \dots & 0 \\ \vdots & & & \ddots & \ddots & \ddots & & & \\ 0 & & & & & & & & \end{pmatrix} \begin{pmatrix} \theta_0 \\ \theta_1 \\ \theta_2 \\ \vdots \\ \theta_{N+2} \end{pmatrix} = \begin{pmatrix} \frac{1}{\pi}(zD^2\theta, T_0) \\ \frac{2}{\pi}(zD^2\theta, T_1) \\ \frac{2}{\pi}(zD^2\theta, T_2) \\ \vdots \\ \frac{2}{\pi}(zD^2\theta, T_{N+2}) \end{pmatrix} \tag{5.3.15}$$

Let the coefficient matrix in (5.3.15) be denoted by ZD^2 then (5.3.14) can be rewritten as the eigenvalue problem,

$$\begin{pmatrix} 4D^2 - a^2I & -I & 0 & 0 \\ 0 & 2(4D^2 - a^2I) & 0 & -fR_c a^2 I \\ 0 & 0 & * & 0 \\ fR_c I & 0 & 0 & \frac{2}{Sc}(4D^2 - a^2I) \end{pmatrix} \begin{pmatrix} \mathbf{W} \\ \mathbf{A} \\ \mathbf{\Theta} \\ \mathbf{\Phi} \end{pmatrix}$$

$$= R \begin{pmatrix} 0 & 0 & 0 & 0 \\ 0 & 0 & \# & 0 \\ \$ & 0 & 0 & 0 \\ 0 & 0 & 0 & 0 \end{pmatrix} \begin{pmatrix} \mathbf{W} \\ \mathbf{A} \\ \mathbf{\Theta} \\ \mathbf{\Phi} \end{pmatrix},$$

where $* = 2(\mu - 1)(4D^2 - a^2I) - 8D - 8ZD^2 + 2a^2Z$, D is the Chebyshev matrix representation of $\partial/\partial z$, $\# = -a^2(2\xi + \mu - 2)I + 2a^2Z$, and $\$ = (2\xi + \mu - 2)I - 2Z$. This system was solved numerically (via the QZ algorithm) and the results used to check those obtained by the compound matrix method. Excellent agreement was found between the three systems outlined above.

5.4 Numerical Discussion, Results and Conclusions

To be in keeping with Joseph [41] the parameter $\tau = Sc/Pr = \kappa/\kappa_c$ is introduced. Typical values for the thermal and solute diffusivities are $\kappa = 1.33 \times 10^{-3}\text{cm}^2\text{s}^{-1}$ and $\kappa_c = 0.7 \times 10^{-5}\text{cm}^2\text{s}^{-1}$ respectively cf. Unterberg [101], so we restrict our attention to $\tau \in [10^2, 10^3]$. Throughout all calculations we fix $Pr = 13.4$ which is consistent for water at low temperatures.

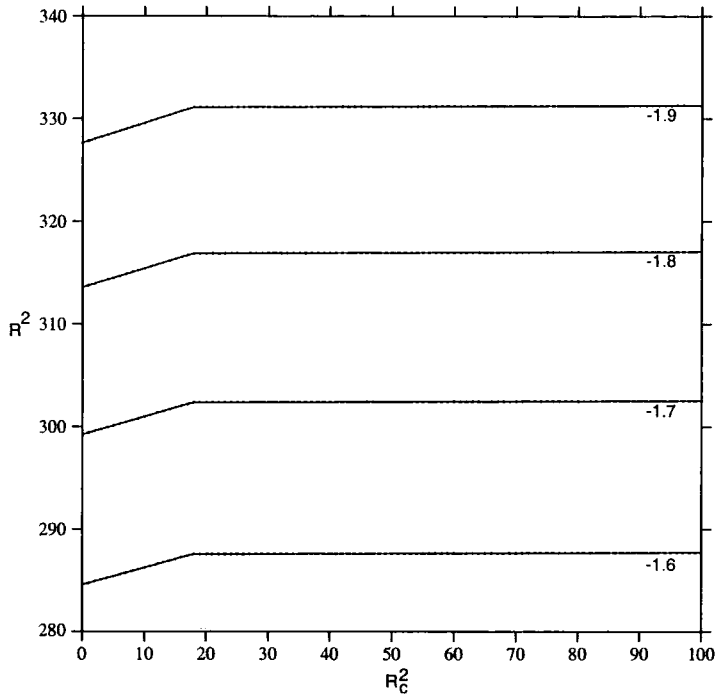

Figure 5.2: A plot of the linear instability curves for R^2 against R_c^2. $\tau = 100$, $a^2 = 9.705432$, $Pr = 13.4$, $-T_l$ varies as shown on graph.

Figure 5.2 displays the linear instability curves for τ and a^2 fixed, and $-T_l$ varying. As $-T_l$ decreases the linear instability curves shift up (a change of $0.1°$C corresponds to a change of approximately 15 in R^2). Note that $R^2 \propto T_l^2$. To see how $-T_l$ effects instability we define a new Rayleigh number $\hat{R}^2 = R^2/T_l^2$. Then inspection of figure 5.2 reveals that as the temperature of the salt water becomes cooler the system becomes more unstable. This is to be expected since the temperature gradient is destabilising.

Figure 5.3 displays the linear instability and nonlinear stability curves for $-T_l$ and a^2 fixed and τ varying. $-T_l$ is fixed at $-1.9°$C and a^2 at the critical value returned from energy theory. To produce the linear instability curves, R_c^2 was fixed and R^2 found such that the real part of the temporal growth rate $\sigma_r = 0$ ($\sigma = \sigma_r + i\sigma_i, \sigma_r, \sigma_i \in \mathbb{R}$). We then tracked through R_c^2 to produce the curves. It is worth noting that for $\tau \leq 10$ the tracking routine ran for a very wide range of starting values for R^2. However for $\tau > 10$ the graphing routine failed to locate the root, $\sigma_r = 0$, unless the two initial guess for R^2 were very close to the actual value. When $R_c^2 = 0$, the critical Rayleigh number is approximately the same for all τ. So to find good starting values for R^2 the graphing routine was initially run for $\tau = 10$ and the results used to provide initial values when

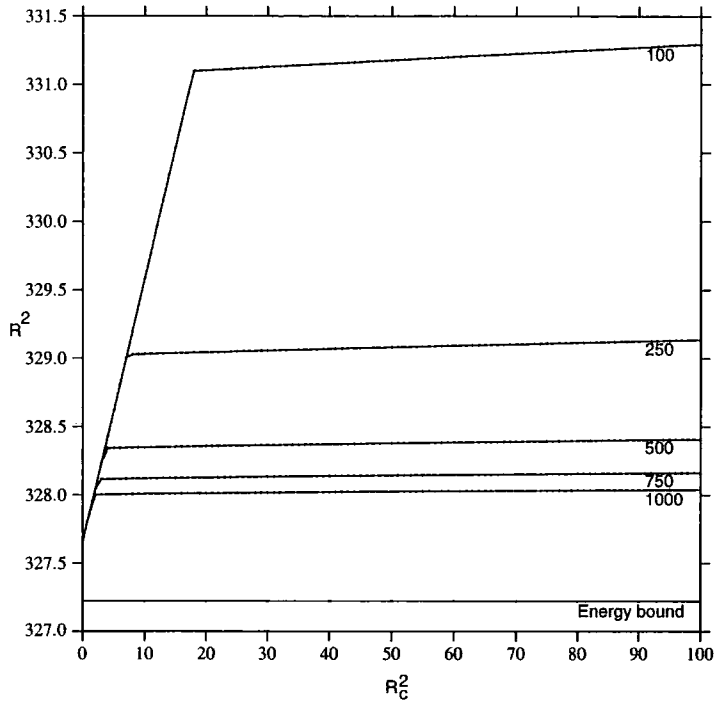

Figure 5.3: A plot of the linear instability curves and the nonlinear stability curve for R^2 against R_c^2. $-T_l = -1.9°\mathrm{C}$, $a^2 = 9.705432$, $Pr = 13.4$, τ varies as shown on graph.

$\tau > 10$.

The behaviour of the linear instability curves is in good agreement with that seen in Joseph [41]. The kink in the curves represents the point at which convection switches from steady convection ($\sigma = 0$) to oscillatory ($\sigma_r = 0, \sigma_i \neq 0$). Note that as τ increases the onset of convection is more likely to be via oscillatory convection as opposed to steady convection. We also note that as τ increases the critical Rayleigh number, for a fixed solute Rayleigh number, decreases. To establish how τ effects the instability of the system we note that $R^2 \propto 1/\tau$ for fixed R_c^2. Hence defining a new Rayleigh number, $\hat{R}^2 = \tau R^2$ and inspecting figure 5.3 shows that, as the thermal diffusivity increases, for fixed solute diffusivity, the system becomes more stable. Again this is to be expected since the temperature gradient is destabilising.

The nonlinear stability bound was produced by integrating the compound matrix equations and then finding the critical Rayleigh number

$$Ra_E = \max_{\lambda,\mu} \min_{a^2} R^2(a^2, \lambda, \mu).$$

We note here that in all calculations we found the critical parameters to be

$$\lambda_{crit} = Sc, \qquad \mu_{crit} \approxeq 2\xi.$$

If $\lambda = Sc$ then, as previously mentioned, the governing system reduces to a sixth order one, independent of the salt field. Hence the global nonlinear stability bound is independent of the salt field. This is in keeping with what Shir & Joseph [90] found for a Boussinesq fluid layer heated and salted from below.

We observe from figure 5.3 that for $R_c = 0$ there is very good agreement between the nonlinear stability and linear instability bounds. We also note that as τ increases the linear and nonlinear results become closer and remark that since the critical Rayleigh numbers are so close (for τ sufficiently large) we expect the linear analysis to have captured the essential physics at the onset of convection. However as τ decreases the agreement between the two thresholds is not so good and we highlight this area as a region of possible subcritical instabilities.

Mulone [64], Lombardo *et al.* [48,49], and Basurto & Lombardo [5] all investigated such regions of subcritical instabilities. In these cases however the density was assumed to be linear in temperature and concentration field. Mulone [64] considered a Boussinesq fluid layer heated and salted from below and showed that when $\tau < 1$ coincidence between linear and nonlinear critical parameters can be found. Lombardo *et al.* [49] and Basurto & Lombardo [5] investigated the situation when $\tau > 1$ and regions of coincidence between linear and nonlinear results were established. Lombardo *et al.* [48] concentrated on the Bénard problem for a mixture with superimposed plane parallel shear flows. They found unconditional stability results for arbitrary τ and small Reynolds numbers, and *conditional* stability results independent of the Reynolds number up to criticality for any Schmidt and Prandtl number. A similar analysis of the subcritical region presented in this chapter proves to be nontrivial. It is stressed that the nonlinear stability bounds derived here and those presented in the next chapter are all unconditional.

Chapter 6

Unconditional Nonlinear Stability for Temperature Dependent Density Flow in a Porous Medium

The object of this chapter is to present a nonlinear stability analysis of thermal convection in a saturated porous layer. The density of the saturating fluid in this instance however is assumed to have a cubic temperature dependence as proposed by Merker *et al.* [61]. Merker *et al.* also formulated a density law with quintic temperature dependence. They compared their two relations to the more commonly used quadratic one, as previously employed, and advocated by Veronis [102]. On the basis of linear theory, Merker *et al.* suggested that their cubic law was about 10% more accurate than the quadratic one, whereas the quintic law yielded an improvement of approximately 3% over the cubic law. McKay & Straughan [52] used the cubic and quintic laws of Merker *et al.* to describe penetrative convection in a fluid layer. They concluded that the cubic density relation was preferable to the quintic model since the quintic model leads to complicated mathematics for relatively little gain in accuracy. In fact the cubic law proves to be a popular choice because it is more accurate than the quadratic law but easier to implement than the quintic one, cf. McKay & Straughan and the references therein.

A cubic density law is also employed by McKay & Straughan [51]. In that work McKay & Straughan investigated the influence of a cubic density law on patterned ground formation. In this chapter we consider a system essentially the same as that given in

McKay & Straughan but with three notable exceptions. Two of the differences are due to the fact that McKay & Straughan considered the specific case of patterned ground formation, an application of the analysis presented here. The third is that McKay & Straughan did not include a Forchheimer drag term in their governing equations whereas here we do. McKay & Straughan employed the well known Darcy [21] equations to describe flow in the porous medium, cf. chapters 2-4. The equations of Darcy are believed to be valid for flow in a region where the velocity is not too large. For situations where the fluid velocity is not so small however, Darcy's equations are usually modified by adding a Forchheimer term, see Forchheimer [31] and Nield & Bejan [73]. Various mathematical and experimental justifications of Forchheimer theory have recently been given cf. Gilver & Altobelli [36], Whitaker [105], and Giorgi [35]. In fact Giorgi points out that Forchheimer terms were actually used much earlier by Dupuit [25]. A thorough discussion of Darcy's equations and the Forchheimer modification can be found in Nield & Bejan [73].

To establish unconditional nonlinear results we found it necessary to use Forchheimer theory and introduce higher order norms. The attractive mathematical features of Forchheimer theory are highlighted in Payne & Straughan [77, 78]. Payne & Straughan [78] used Forchheimer theory to establish unconditional nonlinear results for flow in porous media where viscosity was assumed to vary with temperature and density was assumed constant. They also obtained unconditional results for which the viscosity was assumed linear in temperature and the density quadratic. We use a similar analysis to that presented in Payne & Straughan [78] but address the issue of unconditional stability for flow in porous media for which the viscosity is assumed constant and the density cubic in temperature dependence.

McKay & Straughan [51] successfully developed a linear instability and a nonlinear stability analysis for the onset of convection in the formation of patterned ground. However, the nonlinear stability results they achieve are conditional i.e. they are restricted to initial data thresholds. In this chapter we tackle the important question of unconditional stability and stress that we establish a fully unconditional result i.e. for all initial data. In section 6.4, a comparison is made between the unconditional results derived here and the linear results of McKay & Straughan. Very close agreement is found between the critical parameters of both theories. The nonlinear theory presented here establishes an uncon-

ditional threshold, below which stability is guaranteed. The linear work of McKay & Straughan provides an instability threshold above which instability is guaranteed. Since the two thresholds are so close, we effectively guarantee that there are no subcritical instabilities, and conclude that the linear analysis of McKay & Straughan gives a very good physical representation of what happens in reality.

An outline of this chapter is as follows. In the next section the equations and boundary conditions which govern the system are described. It is then shown that the standard energy technique with an L^2 norm is insufficient to establish unconditional results. Higher order norms are then introduced and an unconditional nonlinear stability bound is established. The numerical solution of the nonlinear system is then discussed and finally a presentation of the numerical results and a comparison with those published in McKay & Straughan [51] is given.

6.1 Convection in a Porous Medium with a Cubic Density Law

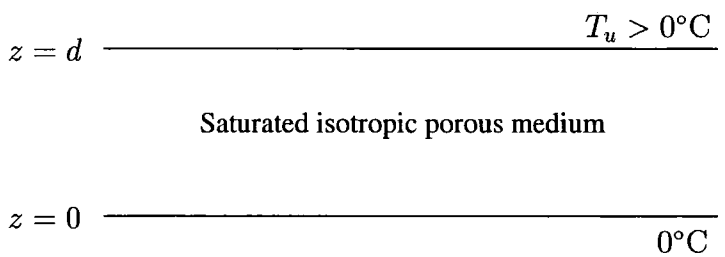

Figure 6.1: Schematic diagram of the governing system.

Consider an isotropic porous layer saturated with fluid contained between the horizontal planes $z = 0$ and $z = d$. The z direction is denoted by the vector $\mathbf{k}$ with $\mathbf{i}, \mathbf{j}, \mathbf{k}$ being the standard Cartesian basis. Gravity acts in the negative z direction and the upper and lower planes are held fixed at temperatures $T_u > 0°\mathrm{C}$ and $0°\mathrm{C}$ respectively, see figure 6.1. The equation of state is assumed to have a cubic temperature dependence, as advocated by Merker *et al.* [61], namely

$$\rho = \rho_0 \left[1 + AT - BT^2 + CT^3\right], \tag{6.1.1}$$

where ρ is the liquid density, ρ_0 is the density at 0°C, $T(°C)$ is the temperature and A, B, C, have constant values obtained by curve fitting to data points (cf. Merker *et al.*).

Neglecting fluid inertia, absorbing the constant term in (6.1.1) into the pressure and employing Darcy's law with Forchheimer drag terms (cf. Forchheimer [31] and Nield & Bejan [73]), yields a momentum equation of the form

$$p_{,i} = -\frac{\mu}{K}v_i - g\rho_0 k_i \left(AT - BT^2 + CT^3\right) - b'|\mathbf{v}|v_i - c'|\mathbf{v}|^2 v_i, \tag{6.1.2}$$

where $p, \mu, K, v_i, g, b', c'$ are pressure, dynamic viscosity, permeability, velocity, gravity and Forchheimer terms respectively. Standard indicial notation and the Einstein summation convention are employed throughout, and as previously mentioned $\mathbf{k} = (0, 0, 1)^T$. Equation (6.1.2) together with the incompressibility condition and the equation of energy balance yield the following system of governing equations

$$\begin{aligned} &p_{,i} = -\frac{\mu}{K}v_i - g\rho_0 k_i \left(AT - BT^2 + CT^3\right) - b'|\mathbf{v}|v_i - c'|\mathbf{v}|^2 v_i, \\ &v_{i,i} = 0, \\ &T_{,t} + v_i T_{,i} = \kappa \Delta T, \end{aligned} \tag{6.1.3}$$

where t, κ, and Δ are time, thermal diffusivity and the Laplacian operator respectively. The upper and lower boundaries of the porous medium are assumed fixed, so the boundary conditions $v_3(0) = v_3(d) = 0$, $T(0) = 0°C$, $T(d) = T_u$ are imposed.

The basic steady state solutions of (6.1.3) are,

$$\bar{v}_i = 0, \qquad \bar{T} = \beta z,$$

where $\beta = T_u/d$. The hydrostatic pressure $\bar{p}$ may be found from $(6.1.3)_1$ but since $\bar{p}$ is eliminated from our analysis later on, a derivation of it is not included here.

To study the stability of (6.1.3), perturbations (u_i, θ, π) to the steady state solution are introduced as follows

$$v_i = \bar{v}_i + u_i, \qquad T = \bar{T} + \theta, \qquad p = \bar{p} + \pi.$$

Substituting the perturbed expressions into (6.1.3) and non-dimensionalising with scalings of

$$X = d, \qquad \mathcal{T} = \frac{\rho_0 K}{\mu}, \qquad U = \frac{\mu d}{\rho_0 K}, \qquad P = \frac{\mu d U}{K}, \qquad T^{\#} = U\sqrt{\frac{T_u Pr}{gdA}},$$

for displacement, time, velocity, pressure and temperature respectively, yields

$$\begin{aligned} \pi_{,i} &= -u_i - R\theta F(z)k_i + \theta^2 G(z)k_i - \frac{a_2\theta^3 Pr^2}{R}k_i - b|\mathbf{u}|u_i - c|\mathbf{u}|^2 u_i, \\ u_{i,i} &= 0, \\ Pr\,(\theta_{,t} + u_i\theta_{,i}) &= -Rw + \Delta\theta, \end{aligned} \tag{6.1.4}$$

where

$$\begin{aligned} F(z) &= 1 - 2a_1 z + 3a_2 z^2, \qquad G(z) = Pr\,(a_1 - 3a_2 z), \\ a_1 &= \frac{B}{A}T_u, \qquad a_2 = \frac{C}{A}T_u, \qquad b = \frac{b'd}{\rho_0}, \qquad c = \frac{c'\mu d^2}{\rho_0^2 K}. \end{aligned}$$

The Prandtl number Pr, and associated Rayleigh number R^2 are given by

$$Pr = \frac{\mu d^2}{\kappa\rho_0 K}, \qquad R^2 = \frac{gdA\rho_0 K T_u}{\kappa\mu}.$$

The spatial domain of the porous layer is now $\{(x,y) \in \mathbb{R}^2\} \times \{z \in (0,1)\}$ and $w = u_3$. The perturbed boundary conditions are given by

$$w(0) = w(1) = 0, \qquad \theta(0) = \theta(1) = 0. \tag{6.1.5}$$

It is assumed that (u_i, θ, π) have a periodic plan-form shape that tiles the (x,y) plane and henceforth we let V denote the period cell for the perturbations.

6.2 Unconditional Nonlinear Stability

The standard approach to obtain a global nonlinear stability bound in $L^2(V)$, (where $L^2(V)$ is the space of square integrable functions on V), proceeds as follows. First multiply $(6.1.4)_1$ by u_i, integrate over V and make use of (6.1.5) and some integration by parts to obtain

$$\begin{aligned} 0 = -\|\mathbf{u}\|^2 - R\langle F(z)w\theta\rangle + \langle G(z)w\theta^2\rangle - \frac{a_2 Pr^2}{R}\langle w\theta^3\rangle \\ -b\int_V |\mathbf{u}|^3 d\mathbf{x} - c\int_V |\mathbf{u}|^4 d\mathbf{x}, \end{aligned} \tag{6.2.1}$$

where $\|\cdot\|$ denotes the norm on $L^2(V)$ and $\langle\cdot\rangle$ denotes integration over V. Similarly, multiplying $(6.1.4)_3$ by θ, integrating over V and making use of (6.1.5) yields (after some integrations by parts)

$$\frac{d}{dt}\left(\frac{Pr}{2}\|\theta\|^2\right) = -R\langle w\theta\rangle - \|\nabla\theta\|^2. \tag{6.2.2}$$

An energy equation is then obtained by adding (6.2.1) to (6.2.2), hence

$$\frac{d}{dt}\left(\frac{Pr}{2}\|\theta\|^2\right) = -R\langle w\theta\rangle - \|\nabla\theta\|^2 - \|\mathbf{u}\|^2 - R\langle F(z)w\theta\rangle + \langle G(z)w\theta^2\rangle - \frac{a_2 Pr^2}{R}\langle w\theta^3\rangle - b\int_V |\mathbf{u}|^3 d\mathbf{x} - c\int_V |\mathbf{u}|^4 d\mathbf{x}. \tag{6.2.3}$$

However, due to the higher order terms in the right hand side of (6.2.3), a standard energy technique in $L^2(V)$ fails to provide an unconditional nonlinear stability bound. To see why this is, we follow an argument similar to that given in Payne & Straughan [78]. We begin by defining the sign indefinite terms on the right of (6.2.3) by I and the sign definite dissipation by D. Therefore, assuming $b, c > 0$,

$$I = -R\langle w\theta\rangle - R\langle F(z)w\theta\rangle + \langle G(z)w\theta^2\rangle - \frac{a_2 Pr^2}{R}\langle w\theta^3\rangle, \tag{6.2.4}$$

$$D = \|\nabla\theta\|^2 + \|\mathbf{u}\|^2 + b\int_V |\mathbf{u}|^3 d\mathbf{x} + c\int_V |\mathbf{u}|^4 d\mathbf{x}. \tag{6.2.5}$$

Suppose an energy is defined as $E = \frac{1}{2}Pr\|\theta\|^2$ then from (6.2.3)

$$\frac{dE}{dt} = I - D = -D\left(1 - \frac{I}{D}\right).$$

Then by the usual energy argument, if

$$\max_{\mathcal{H}} \frac{I}{D} < 1,$$

where $\mathcal{H}$ is the space of admissible functions, we may conclude nonlinear stability (cf. section 4.3).

In this case however, the term $\max_{\mathcal{H}} I/D$ is not bounded above by 1. To see this we begin by noting that since the space $\mathcal{H}$ is linear, u_i may be written as αu_i and θ as $\beta\theta$ for arbitrary real numbers α, β. Then

$$\frac{I}{D} = \frac{A\alpha\beta + B\alpha\beta^2 + C\alpha\beta^3}{D\beta^2 + E\alpha^2 + F\alpha^3 + G\alpha^4}$$

where $A, \ldots, G$ are the appropriate integrals from (6.2.4) and (6.2.5). Suppose u_i and θ are fixed, then $A, \ldots, G$ can be treated as constants. Let $\beta = \alpha^{1+\omega}$ where ω is some positive constant, then

$$\frac{I}{D} = \frac{A\alpha^{2+\omega} + B\alpha^{3+2\omega} + C\alpha^{4+3\omega}}{D\alpha^{2+2\omega} + E\alpha^2 + F\alpha^3 + G\alpha^4} = \frac{A/\alpha^{\omega} + B\alpha + C\alpha^{2+\omega}}{D + E/\alpha^{2\omega} + F\alpha/\alpha^{2\omega} + G\alpha^2/\alpha^{2\omega}}.$$

Suppose we choose $\omega = 1/2$ then

$$\frac{I}{D} = \frac{A/\alpha^{1/2} + B\alpha + C\alpha^{5/2}}{D + E/\alpha + F + G\alpha} = \frac{A/\alpha^{3/2} + B + C\alpha^{3/2}}{D/\alpha + E/\alpha^2 + F/\alpha + G} \to \infty \quad \text{as} \quad \alpha \to \infty.$$

Hence the maximum of I/D in $\mathcal{H}$ cannot be achieved and we conclude that any straightforward approach to derive global nonlinear stability using $L^2(V)$ theory seems to fail. We note at this point however that a *conditional* nonlinear stability bound can be found in $L^2(V)$, cf. McKay & Straughan [51]. In the remainder of this section unconditional stability results are established by introducing norms of higher order and following an analysis analogous to that presented in Payne & Straughan [78].

$L^p(V)$, where $p > 2$, is defined as the space of functions on V such that

$$L^p(V) = \left\{ \mathbf{v} \in V | \int_V |\mathbf{v}|^p d\mathbf{x} < \infty \right\}.$$

Let the associated norm $\| \cdot \|_p$ be given by

$$\|\mathbf{v}\|_p = \left\{ \int_V |\mathbf{v}|^p d\mathbf{x} \right\}^{\frac{1}{p}}.$$

Using $(6.1.4)_3$, the fact that the derivative of $\text{sign}\theta$ is a Dirac delta function and employing properties of the delta function, the following can be derived

$$\begin{aligned} \frac{d}{dt}\left(\frac{Pr}{3}\|\theta\|_3^3\right) &= \frac{d}{dt}\left(\frac{Pr}{3}\int_V \theta^3(\text{sign}\theta)d\mathbf{x}\right) \\ &= -R\int_V w\theta^2(\text{sign}\theta)d\mathbf{x} - \frac{8}{9}\int_V |\theta|_{,i}^{\frac{3}{2}}|\theta|_{,i}^{\frac{3}{2}}d\mathbf{x}. \end{aligned} \tag{6.2.6}$$

The second term in the right hand side of (6.2.6) can be bounded using Poincaré's inequality (appendix B.1) to yield

$$\frac{d}{dt}\left(\frac{Pr}{3}\|\theta\|_3^3\right) \leq -R\int_V w\theta^2(\text{sign}\theta)d\mathbf{x} - \frac{8\pi^2}{9}\int_V |\theta|^3 d\mathbf{x}. \tag{6.2.7}$$

Young's inequality (appendix B.2) is used on the first term in the right hand side of (6.2.7) to obtain

$$\frac{d}{dt}\left(\frac{Pr}{3}\|\theta\|_3^3\right) \leq \left(\frac{2R}{3\beta} - \frac{8\pi^2}{9}\right)\int_V |\theta|^3 d\mathbf{x} + \frac{R\beta^2}{3}\int_V |\mathbf{u}|^3 d\mathbf{x}, \tag{6.2.8}$$

where $\beta > 0$ is some constant which we are free to choose.

In a similar fashion an identity for L^4 is introduced as follows. First observe that

$$\frac{d}{dt}\left(\frac{Pr}{3}\|\theta\|_4^4\right) = -R\langle w\theta^3\rangle - \frac{3}{4}\int_V \theta_{,i}^2\theta_{,i}^2 d\mathbf{x}. \tag{6.2.9}$$

Then bounding the first term on the right by Young's inequality and the second via Poincaré's inequality yields

$$\frac{d}{dt}\left(\frac{Pr}{3}\|\theta\|_4^4\right) \leq \frac{3}{4}\left(R\gamma - \pi^2\right)\int_V \theta^4 d\mathbf{x} + \frac{R}{4\gamma^3}\int_V |\mathbf{u}|^4 d\mathbf{x}, \tag{6.2.10}$$

where $\gamma > 0$ is some constant which we are free to choose. We now define an "energy", $E(t)$ by

$$E(t) = \frac{\mu Pr}{2}\|\theta\|^2 + \frac{\lambda Pr}{3}\|\theta\|_3^3 + \frac{\tau Pr}{4}\|\theta\|_4^4, \tag{6.2.11}$$

where μ, λ and τ are positive constant coupling parameters at our disposal. Then using (6.2.1), (6.2.2), (6.2.8) and (6.2.10), it is found that

$$\begin{aligned}\frac{dE}{dt} \leq -R\mu\left\langle w\theta\right\rangle - \mu\|\nabla\theta\|^2 + \lambda\left(\frac{2R}{3\beta} - \frac{8\pi^2}{9}\right)\int_V |\theta|^3 d\mathbf{x} + \frac{\lambda R\beta^2}{3}\int_V |\mathbf{u}|^3 d\mathbf{x} \\ + \frac{3\tau}{4}\left(R\gamma - \pi^2\right)\int_V \theta^4 d\mathbf{x} + \frac{R\tau}{4\gamma^3}\int_V |\mathbf{u}|^4 d\mathbf{x} \\ -\|\mathbf{u}\|^2 - R\left\langle F(z)w\theta\right\rangle + \left\langle G(z)w\theta^2\right\rangle - \frac{a_2 Pr^2}{R}\left\langle w\theta^3\right\rangle - b\int_V |\mathbf{u}|^3 d\mathbf{x} - c\int_V |\mathbf{u}|^4 d\mathbf{x}.\end{aligned} \tag{6.2.12}$$

To bound the $\langle w\theta^3\rangle$ term, Young's inequality is used as follows

$$\frac{a_2 Pr^2}{R}\left\langle -w\theta^3\right\rangle \leq \frac{3a_2 Pr^2\gamma}{4R}\int_V \theta^4 d\mathbf{x} + \frac{a_2 Pr^2}{4R\gamma^3}\int_V |\mathbf{u}|^4 d\mathbf{x}. \tag{6.2.13}$$

To deal with $\langle G(z)w\theta^2\rangle$ we maximise $G(z)$ for $z \in (0,1)$ and then use Young's inequality again to deduce that

$$\left\langle G(z)w\theta^2\right\rangle \leq a_1 Pr\left\langle w\theta^2\right\rangle \leq \frac{2a_1 Pr}{3\beta}\int_V |\theta|^3 d\mathbf{x} + \frac{a_1 Pr\beta^2}{3}\int_V |\mathbf{u}|^3 d\mathbf{x}. \tag{6.2.14}$$

Let

$$I = -\mu\left\langle w\theta\right\rangle - \left\langle F(z)w\theta\right\rangle, \qquad D = \mu\|\nabla\theta\|^2 + \|\mathbf{u}\|^2, \tag{6.2.15}$$

and define R_E by

$$\frac{1}{R_E} = \max_{\mathcal{H}} \frac{I}{D}. \tag{6.2.16}$$

Substituting (6.2.13), (6.2.14) and (6.2.16) into (6.2.12) yields

$$\begin{aligned}\frac{dE}{dt} \leq -\left(\frac{R_E - R}{R_E}\right)D + \int_V |\mathbf{u}|^3\left\{\frac{\beta^2}{3}\left(R\lambda + a_1 Pr\right) - b\right\}d\mathbf{x} \\ + \int_V |\theta|^3\left\{\frac{2}{3\beta}\left(R\lambda + a_1 Pr\right) - \frac{8\pi^2\lambda}{9}\right\}d\mathbf{x} \\ + \int_V |\mathbf{u}|^4\left\{\frac{1}{4\gamma^3}\left(R\tau + \frac{a_2 Pr^2}{R}\right) - c\right\}d\mathbf{x} \\ + \int_V \theta^4\left\{\frac{3\tau}{4}\left(R\gamma - \pi^2\right) + \frac{3a_2 Pr^2\gamma}{4R}\right\}d\mathbf{x}.\end{aligned} \tag{6.2.17}$$

To deal with the higher order terms, we begin by choosing $\lambda, \tau, \gamma, \beta$ such that

$$\lambda = \lambda' + k_1\epsilon_1, \qquad \frac{2}{3\beta}\left(R\lambda' + a_1 Pr\right) - \frac{8\pi^2\lambda'}{9} = 0, \tag{6.2.18}$$

$$\tau = \tau' + k_2\epsilon_2, \qquad \frac{3\tau'}{4}\left(R\gamma - \pi^2\right) + \frac{3a_2 Pr^2\gamma}{4R} = 0, \tag{6.2.19}$$

where ϵ_1, ϵ_2, are arbitrary (small) positive numbers and k_1, k_2 are free to choose. The following are then minimised

$$\frac{\beta^2}{3}\left(R\lambda' + a_1 Pr\right), \qquad \frac{1}{4\gamma^3}\left(R\tau' + \frac{a_2 Pr^2}{R}\right). \tag{6.2.20}$$

To do this, $(6.2.18)_2$ is solved for λ', $(6.2.19)_2$ for τ' and the respective terms substituted into (6.2.20). The resulting terms are then differentiated with respect to β and γ respectively and β, γ found such that (6.2.20) are minimised. This yields the selection

$$\beta = \frac{9R}{8\pi^2}, \qquad \gamma = \frac{3\pi^2}{4R}, \qquad \lambda' = \frac{2a_1 Pr}{R}, \qquad \tau' = \frac{3a_2 Pr^2}{R^2}.$$

The choice $k_1 = 27/8\pi^2, k_2 = 16/3\pi^2$ is then made and, hence (6.2.17) reduces to

$$\begin{aligned}\frac{dE}{dt} \leq -\left(\frac{R_E - R}{R_E}\right) D - \hat{b}\int_V |\mathbf{u}|^3 d\mathbf{x} - \epsilon_1 \int_V |\theta|^3 d\mathbf{x} \\ -\hat{c}\int_V |\mathbf{u}|^4 d\mathbf{x} - \epsilon_2 \int_V \theta^4 d\mathbf{x},\end{aligned} \tag{6.2.21}$$

where

$$\hat{b} = b - a_1 Pr\left(\frac{9R}{8\pi^2}\right)^2 - \epsilon_1\left(\frac{9R}{8\pi^2}\right)^3, \qquad \hat{c} = c - \frac{a_2 Pr^2}{R}\left(\frac{4R}{3\pi^2}\right)^3 - \epsilon_2\left(\frac{4R}{3\pi^2}\right)^4.$$

To ensure $\hat{b}, \hat{c} > 0$, b and c are restricted as follows

$$b > a_1 Pr\left(\frac{9R}{8\pi^2}\right)^2 + \epsilon_1\left(\frac{9R}{8\pi^2}\right)^3, \qquad c > \frac{a_2 Pr^2}{R}\left(\frac{4R}{3\pi^2}\right)^3 + \epsilon_2\left(\frac{4R}{3\pi^2}\right)^4.$$

Since $\epsilon_1, \epsilon_2 > 0$ are at our disposal and we chose them arbitrarily small, the effective restrictions on b and c are

$$b > a_1 Pr\left(\frac{9R}{8\pi^2}\right)^2, \qquad c > \frac{a_2 Pr^2}{R}\left(\frac{4R}{3\pi^2}\right)^3. \tag{6.2.22}$$

Let $\hat{a} = (R_E - R)/R_E$, and suppose b, c satisfy (6.2.22), then provided $R < R_E$, (6.2.21) reduces to

$$\frac{dE}{dt} \leq -\hat{a}D - \epsilon_1 \int_V |\theta|^3 d\mathbf{x} - \epsilon_2 \int_V \theta^4 d\mathbf{x}. \tag{6.2.23}$$

Using Poincaré's inequality in (6.2.15) we note that

$$D \geq \mu\pi^2\|\theta\|^2 + \|\mathbf{u}\|^2 \geq \mu\pi^2\|\theta\|^2. \tag{6.2.24}$$

Hence using (6.2.24) in (6.2.23), yields

$$\begin{aligned} \frac{dE}{dt} &\leq -\hat{a}\mu\pi^2\|\theta\|^2 - \epsilon_1\int_V |\theta|^3 d\mathbf{x} - \epsilon_2\int_V \theta^4 d\mathbf{x}, \\ &\leq -kE, \\ \Rightarrow E(t) &\leq E(0)e^{-kt}, \end{aligned} \tag{6.2.25}$$

where

$$k = \min\left\{\frac{2\hat{a}\pi^2}{Pr}, \quad \frac{3\epsilon_1}{\lambda Pr}, \quad \frac{4\epsilon_2}{\tau Pr}\right\}.$$

Therefore, $E(t) \to 0$ as $t \to \infty$ where convergence is at least exponential.

Observe that decay in $\|\mathbf{u}\|^2$, $\|\mathbf{u}\|_3^3$, $\|\mathbf{u}\|_4^4$ can also be established. To see this first note from (6.2.1) that

$$\|\mathbf{u}\|^2 + b\|\mathbf{u}\|_3^3 + c\|\mathbf{u}\|_4^4 = -R\langle F(z)w\theta\rangle + \langle G(z)w\theta^2\rangle - \frac{a_2Pr^2}{R}\langle w\theta^3\rangle. \tag{6.2.26}$$

To bound the first term on the right hand side of (6.2.26) we minimise $-F(z)$ for $z \in (0,1)$ and use Young's inequality to deduce that

$$\begin{aligned} \langle -RF(z)w\theta\rangle &\leq \int_V R\left(\frac{a_1^2}{3a_2} - 1\right)\theta w d\mathbf{x}, \\ &\leq \int_V \left(\frac{a_1^2}{3a_2} - 1\right)^2 \frac{R^2\theta^2}{2} d\mathbf{x} + \int_V \frac{|\mathbf{u}|^2}{2} d\mathbf{x}. \end{aligned} \tag{6.2.27}$$

Then, using (6.2.27), (6.2.13), and (6.2.14) in (6.2.26) yields

$$\|\mathbf{u}\|^2 + b\|\mathbf{u}\|_3^3 + c\|\mathbf{u}\|_4^4 \leq R^2\left(\frac{a_1^2}{3a_2} - 1\right)^2\|\theta\|^2 + \frac{4a_1Pr}{3\beta}\|\theta\|_3^3 + \frac{3a_2Pr^2\gamma}{2R}\|\theta\|_4^4, \tag{6.2.28}$$

where we have chosen $\beta^2 = 3b/2a_1Pr$ and $\gamma^3 = a_2Pr^2/2Rc$. Decay in $\|\mathbf{u}\|^2$, $\|\mathbf{u}\|_3^3$, $\|\mathbf{u}\|_4^4$ is then obtained from (6.2.28) since $E(t)$ is decaying at least exponentially. Hence we have established that, provided $R < R_E$ and the non dimensional Forchheimer coefficients b, c satisfy (6.2.22), then global nonlinear stability is achieved.

It is worth noting at this point that an unconditional stability bound can also be achieved in L^2 and L^3 if weights are employed (L^4 is not necessary). Unfortunately the resulting Euler-Lagrange equations contain the function $\text{sign}\theta$. It is unclear how to deal with this function in a numerical method and so the weighted method does not yield any practical information in this case.

6.3 Numerical Solution of the Euler-Lagrange Equations

The Euler-Lagrange equations for the maximum in (6.2.16) are found to be

$$\begin{aligned} -p_{,i} &= R_E\left(F(z)+\mu\right)k_i\theta + 2u_i, \\ 0 &= -R_E\left(F(z)+\mu\right)w + 2\mu\Delta\theta, \end{aligned} \tag{6.3.1}$$

where here, p is a Lagrange multiplier which we eliminate from $(6.3.1)_1$ by taking curlcurl of both sides. Then, setting $i = 3$ and assuming a normal mode representation for w and θ of the form $w = W(z)g(x,y)$ and $\theta = \Theta(z)g(x,y)$, where $g(x,y)$ is a horizontal plan form satisfying $(\partial^2/\partial x^2 + \partial^2/\partial y^2)g = -a^2 g$, yields

$$\begin{aligned} 2\left(D^2 - a^2\right)W - R_E\left(F(z)+\mu\right)a^2\Theta &= 0, \\ R_E\left(F(z)+\mu\right)W - 2\mu\left(D^2 - a^2\right)\Theta &= 0, \end{aligned} \tag{6.3.2}$$

where $D^2 = \partial^2/\partial z^2$ and a is the wave number. The corresponding boundary conditions written in terms of the normal modes are

$$W(0) = W(1) = \Theta(0) = \Theta(1) = 0. \tag{6.3.3}$$

This fourth order system was solved numerically for R_E by the compound matrix method and the Chebyshev tau D^2 algorithm. Without going into detail, the basics of both routines are briefly described for the system in hand.

For the compound matrix method, the vector $\mathbf{W}$ is defined as $\mathbf{W} = (W, W', \Theta, \Theta')^T$. Let $\mathbf{W}_1$ and $\mathbf{W}_2$ be independent solutions of (6.3.2) obtained by replacing the boundary condition at $z = 1$ by the initial conditions $\mathbf{W}_1(0) = (0,1,0,0)^T$ and $\mathbf{W}_2(0) = (0,0,0,1)^T$. The variables $y_1, \ldots, y_6$ are formed from the 2×2 minors of the 4×2 solution matrix with columns $\mathbf{W}_1, \mathbf{W}_2$, to give

$$\begin{aligned} y_1 &= W_1W_2' - W_2W_1', & y_2 &= W_1\Theta_2 - W_2\Theta_1, \\ y_3 &= W_1\Theta_2' - W_2\Theta_1', & y_4 &= W_1'\Theta_2 - W_2'\Theta_1, \\ y_5 &= W_1'\Theta_2' - W_2'\Theta_1', & y_6 &= \Theta_1\Theta_2' - \Theta_2\Theta_1'. \end{aligned}$$

Then using (6.3.2) the compound matrix equations are

$$\begin{aligned} y_1' &= R_E \frac{(F(z)+\mu)\,a^2}{2} y_2, \quad & y_2' &= y_3 + y_4, \\ y_3' &= a^2 y_2 + y_5, & y_4' &= a^2 y_2 + y_5, \\ y_5' &= -R_E \frac{(F(z)+\mu)}{2\mu} y_1 + a^2 (y_3 + y_4) + R_E \frac{(F(z)+\mu)\,a^2}{2} y_6, & & \\ y_6' &= -R_E \frac{(F(z)+\mu)}{2\mu} y_2. & & \end{aligned} \tag{6.3.4}$$

This system was integrated numerically subject to the initial condition $y_5(0) = 1$, and the value of R_E varied such that $y_2(1) = 0$ was satisfied to some predefined accuracy. Keeping $\mu, a^2 > 0$, a golden section search routine was then used to numerically find

$$Ra = \max_{\mu} \min_{a^2} R_E^2(\mu, a^2). \tag{6.3.5}$$

A Chebyshev tau D^2 routine was also performed to solve (6.3.2). First, equations (6.3.2) were transformed to the Chebyshev domain $(-1, 1)$ by letting $\hat{z} = 2z - 1$. Then dropping the hats, (6.3.2), yields

$$\begin{aligned} 2\left(4D^2 - a^2\right) W &= R_E \left(\bar{F}(z) + \mu\right) a^2 \Theta, \\ 2\mu \left(4D^2 - a^2\right) \Theta &= R_E \left(\bar{F}(z) + \mu\right) W, \end{aligned} \tag{6.3.6}$$

where $\bar{F}(z) = 3a_2 z^2/4 + (3a_2/2 - a_1)z + 3a_2/4 + 1 - a_1$, $z \in (-1, 1)$ and $W = \Theta = 0$ for $z = \{-1, 1\}$. Since $\bar{F}$ is a quadratic function of z we seek the Chebshev matrix representation of z^2. To construct this matrix we follow an analysis similar to that for the representation of z as given in section 2.5.1.

The solutions W and Θ are expanded in a series of Chebyshev polynomials

$$W = \sum_{n=0}^{N} w_n T_n(z), \qquad \Theta = \sum_{n=0}^{N} \theta_n T_n(z),$$

and the inner product of each equation is taken with some T_k. To find $(z^2\Theta, T_k)$, we begin by noting the following,

$$\begin{aligned} z^2\Theta &= T_1^2 \sum_{n=0}^{N} \theta_n T_n \\ &= T_1^2 \left(\theta_0 T_0 + \theta_1 T_1 + \ldots + \theta_N T_N\right). \end{aligned}$$

So, taking inner products with $T_0, T_1, T_2, \ldots$, and using the orthogonality of Chebyshev polynomials it can be deduced that,

$$\begin{aligned}(z^2\Theta, T_0) &= \frac{\pi}{2}\theta_0 + \frac{\pi}{4}\theta_2,\\ (z^2\Theta, T_1) &= \frac{3\pi}{8}\theta_1 + \frac{\pi}{8}\theta_3,\\ (z^2\Theta, T_2) &= \frac{\pi}{4}\theta_0 + \frac{\pi}{4}\theta_2 + \frac{\pi}{8}\theta_4, \ldots \text{etc.}\end{aligned}$$

This can be expressed in matrix form as,

$$\begin{pmatrix} \frac{1}{2} & 0 & \frac{1}{4} & 0 & 0 & \ldots & 0 \\ 0 & \frac{3}{4} & 0 & \frac{1}{4} & 0 & \ldots & 0 \\ \frac{1}{2} & 0 & \frac{1}{2} & 0 & \frac{1}{4} & \ldots & 0 \\ \vdots & & \ddots & \ddots & \ddots & & \\ 0 & & & & & & \end{pmatrix} \begin{pmatrix} \theta_0 \\ \theta_1 \\ \theta_2 \\ \vdots \\ \theta_N \end{pmatrix} = \begin{pmatrix} \frac{1}{\pi}(z^2\theta, T_0) \\ \frac{2}{\pi}(z^2\theta, T_1) \\ \frac{2}{\pi}(z^2\theta, T_2) \\ \vdots \\ \frac{2}{\pi}(z^2\theta, T_N) \end{pmatrix} \tag{6.3.7}$$

Let the coefficient matrix in (6.3.7) be denoted by Z^2. Note that Z^2 is exactly the same as the matrix product $Z \times Z$, where Z is given in section 2.5.1. Then (6.3.6) can be rewritten as the eigenvalue problem,

$$\begin{pmatrix} 8D^2 - 2a^2 I & 0 \\ 0 & 8\mu D^2 - 2\mu a^2 I \end{pmatrix} \begin{pmatrix} \mathbf{W} \\ \Theta \end{pmatrix} = R_E \begin{pmatrix} 0 & a^2 * \\ * & 0 \end{pmatrix} \begin{pmatrix} \mathbf{W} \\ \Theta \end{pmatrix},$$

where here D^2 is the Chebyshev matrix representation of $\partial^2/\partial z^2$, I is the identity, $* = 3a_2Z^2/4 + (3a_2/2 - a_1)Z + (3a_2/4 - a_1 + 1 + \mu)I$, $\mathbf{W} = (w_o, ..., w_N)^T$ and $\Theta = (\theta_o, ..., \theta_N)^T$. The last two rows of each $(N+1) \times (N+1)$ block were removed and replaced by the discrete form of the four boundary conditions (6.3.3). The resulting system was then solved using the QZ algorithm. The numerical results obtained from the Chebyshev tau D^2 routine are not presented since excellent agreement was found between them and those obtained via the compound matrix method. A presentation and discussion of the results found from the compound matrix routine are now given.

6.4 Numerical Results and Conclusions

In this section we compare our numerical results with those of McKay & Straughan [51]. Therefore, we assume that the saturating fluid is water and take the following values for

A, B, C (cf. Merker *et al.* [61]),

$$A = 6.85650 \times 10^{-5}\,(^{\circ}\mathrm{C})^{-1},$$
$$B = 8.82063 \times 10^{-6}\,(^{\circ}\mathrm{C})^{-2},$$
$$C = 4.16668 \times 10^{-8}\,(^{\circ}\mathrm{C})^{-3}.$$

To be in keeping with George *et al.* [33], McKay & Straughan adopted a Rayleigh number that reflected the layer depth which is destabilising, namely

$$Ra = \chi^3 \left(\frac{g\alpha\rho_0 K d T_u^2}{\kappa\mu} \right),$$

where $\alpha = 7.68 \times 10^{-6}(^{\circ}\mathrm{C}^{-2})$ and $\chi = 4/T_u$. Therefore, in order to compare the nonlinear results calculated here with the linear results of McKay & Straughan [51], we adopt a Rayleigh number of the form

$$Ra = \frac{4\alpha}{A}\chi^2 R_E^2 \approx 0.448\chi^2 R_E^2.$$

In McKay & Straughan [51] the governing equations and boundary conditions are essentially the same as those used here but with three notable exceptions. Firstly the Forchheimer terms, necessary to establish unconditional stability, are not present in McKay & Straughan. However, in this work the Forchheimer terms are eliminated from the final system due to the way the energy analysis is implemented. Therefore provided the Forchheimer terms satisfy the constraint (6.2.22) we can compare both works. The second difference to note is in the permeability term. McKay & Straughan allowed the permeability to have dependence on z of the form

$$K = k_0\,(1 + \gamma z)\,, \tag{6.4.1}$$

where k_0 was the permeability at the base of the layer and γ was a positive constant. They choose this relationship since it reflects the physics of what happens in patterned ground formation. In the results that follow we only compare results with those published in McKay & Straughan for which they set $\gamma = 0$ and hence K is equivalent to the definition used here. We remark at this point however, that if we allow the permeability to take the same form as (6.4.1) then we can still obtain an unconditional stability bound. To see this note that if we employ (6.4.1) then the first term in the non-dimensional perturbation

equation $(6.1.4)_1$ is of the form $-u_i/(1+\gamma z d)$, where k_0 has been absorbed into the scales. In deriving an energy identity for $\mathbf{u}$ we multiply this term by u_i, integrate over V and bound above as follows

$$-\int_V \frac{u_i u_i}{(1+\gamma z d)} d\mathbf{x} \leq -\frac{\|\mathbf{u}\|^2}{(1+\gamma d)} \qquad \text{for} \quad z \in (0,1). \tag{6.4.2}$$

Since the right hand side of (6.4.2) is sign definite our energy analysis can follow as before. Finally McKay & Straughan allowed for radiation heating at the upper surface. Their boundary condition at $z = 1$ in terms of the perturbed variables was

$$\theta_{,z} + a\theta = 0,$$

where $a \geq 0$ was a constant "radiation parameter". Again this boundary condition was used because it is physically relevant to the specific case of patterned ground formation. We only compare results with those published in McKay & Straughan for which $a = \infty$ and we recover the boundary condition imposed here.

In table 6.1 we compare the linear results of McKay & Straughan [51] with the non-linear results of this work. The critical parameters of linear and energy theory are denoted by subscript L and E respectively. Ra_L and a_L denote the critical Rayleigh number and wave number obtained by McKay & Straughan via a linear instability analysis. Ra_E and a_E denote the critical Rayleigh number and wave number obtained here via the compound matrix method. From table 6.1 we see that there is excellent agreement between the linear and nonlinear results. Hence we conclude that the linear analysis of McKay & Straughan has captured the essential physics of reality. We stress that the unconditional stability threshold established here is of physical importance since it effectively guarantees there are no subcritical instabilities.

T_u(°C)	Ra_L	Ra_E	a_L	a_E	μ
0.5	1209.546	1209.163	3.142	3.142	0.936
1.0	324.427	324.267	3.143	3.143	0.873
1.5	155.419	155.316	3.145	3.145	0.812
2.0	94.727	94.640	3.148	3.150	0.751
2.5	66.083	65.992	3.153	3.156	0.693
3.0	50.363	50.248	3.162	3.167	0.636
3.5	40.922	40.760	3.176	3.183	0.582
4.0	34.957	34.713	3.197	3.208	0.531
4.5	31.120	30.745	3.230	3.245	0.485
5.0	28.705	28.126	3.283	3.300	0.444

Table 6.1: A comparison of the critical parameters of linear instability and nonlinear stability theory. μ is the best coupling parameter.

Chapter 7

Conclusion

Throughout this thesis the subject of thermal convection in fluid and porous media has been investigated. Linear instability and nonlinear stability analyses have been employed to establish critical thresholds for the onset and type of convection involved. Two layer and single layer systems were investigated and convection modelled primarily via a quadratic equation of state and alternatively by internal heating or a cubic density law. Before a discussion of the work and suggestions for the future are made, a quick summary is provided.

In chapter 2 penetrative convection in a superposed porous-fluid layer was modelled via a quadratic equation of state. A similar system was then investigated in chapter 3 but represented alternatively using internal heating. It was found that the two models generated the same eigenvalues when mathematically adjoint but different eigenfunctions. It was concluded that physically the two models were very different and care must be taken when interpreting results.

In chapter 4 penetrative convection in a single anisotropic porous layer was modelled by both a quadratic equation of state and internal heating. The porous medium was assumed to have a horizontally isotropic configuration in which the permeability in the horizontal plane was different to that in the vertical direction. An unconditional nonlinear stability bound, as well as a linear instability bound was established and the two shown to be very close.

In chapter 5 a model for convection in the evolution of under-ice meltponds was presented. Again linear and nonlinear analyses were given and it was shown that to establish unconditional nonlinear results a weighted energy must be employed. The linear insta-

bility and nonlinear stability bounds did not coincide and a region of possible subcritical instabilities was presented.

Finally in chapter 6, an unconditional nonlinear stability bound was found for a layer of isotropic porous medium. Convection in the porous medium was described by a cubic equation of state and Forchheimer drag terms were included in the equations of motion. Higher order norms were found necessary to establish an unconditional bound and so employed to achieve the given result.

In all five chapters a linear instability analysis was performed. The analyses were effective and efficient in establishing basic results for the convection problems at hand. For example the numerical results in chapters 2 & 3 were novel and quite striking. To establish how representative these linear results are however requires a nonlinear approach. This is highlighted by chapters 4, 5 & 6, where linear and nonlinear results were derived and compared for a single layer of fluid or porous medium. A nonlinear analysis of the two layer system however is highly nontrivial. It is hoped that in future work the energy method may be applied to the two layer problem to form a nonlinear stability bound. The inclusion of a Q term may simplify the nonlinear analysis, cf. chapter 4. Indeed this was the motivation behind chapter 3. It is hoped that such work will be of use in future analyses. The introduction of a weight as outlined in chapter 5, or higher order norms as given in chapter 6, are further techniques that may also be of benefit here.

In chapter 4 the porous medium was assumed to have a horizontally isotropic configuration in which the permeability in the horizontal plane was different to that in the vertical direction. Such a configuration is common in the real world. In particular we mentioned frost heave in the formation of patterned ground. Future work could include coupling the work done in chapter 4 with that given in chapter 2. In other words penetrative convection could be modelled in a superposed porous-fluid layer in which the porous medium has an anisotropic configuration like that described in chapter 4. This would provided a more refined model for the onset of penetrative convection in the formation of under water patterned ground. In addition a radiative boundary condition at the upper fluid surface could be included to further reflect the physics involved cf. George *et al.* [33].

A further example of the anisotropic configuration used in chapter 4 is sea ice. Eicken *et al.* [27] suggested that sea ice has a different permeability in the vertical direction to

that given in the horizontal plane. Hence the configuration presented in chapter 4 is an appropriate representation for the permeability of sea ice in the melt season. This could be coupled with the work done in chapters 2 & 5 to yield a model with very serious applications as detailed below.

In chapter 5 a model for convection in the evolution of under-ice meltponds was presented. While the model employed very accurate numerical techniques and gave interesting and useful results, a far more sophisticated approach could be taken. The analysis of chapters 2, 4 & 5, could be used in conjunction with one another to build a layered model which incorporates the overlying melt water, the sea ice, and the layer of fresh water below.

There is evidence that sea ice in the Arctic region is thinning at a most dramatic rate, see for example Rothrock *et al.* [85] and Wadhams & Davis [103, 104]. Ice cover in the Arctic, and anywhere else for that matter, plays a very important role in climate. The effect of ice on Earth's surface albedo and its role in reducing the amount of heat exchanged between the atmosphere and the ocean (or land) beneath the ice make it a vital component of our climate. The amount of ice also affects the density, salinity and flow of sea water. In recent literature a lot of attention has been paid to fast sea ice melting and it's implication for polar climates. For example see Goldman [38], Kerr [42], Rignot & Thomas [82], chapter 5, and the references therein.

One factor which affects sea ice melting but about which relatively little is known, is the formation of under-ice melt ponds. There is very little field data on under-ice melt ponds and as far as I am aware, the work of Bogorodskii & Nagurnyi [9], Eicken [26], Notz *et al.* [74], and that given in chapter 5, are the only recent attempts at modelling them. The formation of under-ice melt ponds however are instrumental in the melting of summer Arctic sea ice. Future research on their formation and evolution is both vital and worthwhile. A model that combines the analysis of chapters 2, 4, 5, and takes account of the surface melt water above would be most beneficial in this area. An investigation of how convection in the fresh water effects the underside of the ice and the pycnocline (layer of water where the density changes rapidly with depth) below, would undoubtedly enhance our current understanding of under-ice meltponds.

Appendix A

Numerical Methods

A.1 The Chebyshev Tau Method

A full discussion of the Chebyshev tau algorithm applied to hydrodynamic stability problems can be found in Dongarra *et al.* [23] and Straughan & Walker [95]. For the purposes of this appendix consider the boundary value problem as outlined in Dongarra *et al.* ,

$$\begin{aligned} u'' + \lambda u &= 0, \quad x \in (-1,1), \\ u(-1) &= u(1) = 0, \end{aligned} \tag{A.1.1}$$

where $u \in L^2(-1,1)$ and we work in the weighted $L^2(-1,1)$ space with inner product

$$(f,g) = \int_{-1}^{1} \frac{fg}{\sqrt{1-x^2}} dx,$$

and associated norm $\|\cdot\|$.

Let u be written as a truncated series of Chebyshev polynomials,

$$u(x) = \sum_{k=0}^{N+2} u_k T_k(x). \tag{A.1.2}$$

Instead of solving (A.1.1), the tau method argues that the following is solved exactly

$$u'' + \lambda u = \tau_1 T_{N+1} + \tau_2 T_{N+2}, \tag{A.1.3}$$

where u is given by (A.1.2) and τ_1, τ_2 are the tau coefficients which may be used to measure the error associated with the truncation of (A.1.2).

The Chebyshev polynomials are orthogonal in the $L^2(-1,1)$ space, so multiplication of (A.1.3) by T_i yields

$$(Lu, T_i) = 0, \quad i = 0, 1, \ldots, N, \tag{A.1.4}$$

$$(Lu, T_{N+j}) = \tau_j \|T_{N+j}\|^2, \quad j = 1, 2, \tag{A.1.5}$$

where L is the differential operator defined by $Lu \equiv u'' + \lambda u$. In (A.1.2), there are $(N+3)$ unknowns, namely, $u_i, i = 0, \ldots, N+2$. Equation (A.1.4) yields $(N+1)$ conditions for u_i and (A.1.5) can be used to calculate the τ's. To find a further two conditions note that $T_n(\pm 1) = (\pm 1)^n$ and use the boundary conditions $u(-1) = u(1) = 0$ to deduce

$$\sum_{n=0}^{N+2} (-1)^n u_n = 0, \qquad \sum_{n=0}^{N+2} u_n = 0. \tag{A.1.6}$$

Hence (A.1.4) and (A.1.6) yield a system of $(N+3)$ equations for the $(N+3)$ unknowns $u_i, i = 0, \ldots, N+2$.

The derivative of a Chebyshev polynomial is a linear combination of lower order Chebyshev polynomials and can be expressed as

$$T_n' = \begin{cases} 2n \sum_{k=1}^{n-1} T_k, & n \text{ even}, \\ 2n \sum_{k=2}^{n-1} T_k + n T_0, & n \text{ odd}. \end{cases} \tag{A.1.7}$$

Then (A.1.4) can be written as

$$u_i^{(2)} + \lambda u_i = 0, \qquad i = 0, \ldots, N, \tag{A.1.8}$$

where the coefficients $u_i^{(2)}$ are given by

$$u_i^{(2)} = \frac{1}{c_i} \sum_{p=i+2, p+i \text{ even}}^{N+2} p(p^2 - i^2) u_p, \tag{A.1.9}$$

with $c_0 = 2$, and $c_i = 1, i = 1, 2, \ldots$. To see why this is, begin by differentiating (A.1.2) to yield

$$u' = \sum_{k=0}^{N+2} u_k T_k'(x) = \sum_{k=0}^{N+2} \sum_{r=0}^{N+2} u_k D_{rk} T_r = \sum_{r=0}^{N+2} u_r^{(1)} T_r, \tag{A.1.10}$$

where

$$T_k'(x) = \sum_{r=0}^{N+2} D_{rk} T_r, \qquad u_r^{(1)} = \sum_{k=0}^{N+2} D_{rk} u_k.$$

Differentiating (A.1.10) yields

$$u'' = \sum_{r=0}^{N+2} u_r^{(1)} T_r' = \sum_{r=0}^{N+2} \sum_{p=0}^{N+2} u_r^{(1)} D_{pr} T_p = \sum_{p=0}^{N+2} u_p^{(2)} T_p, \tag{A.1.11}$$

where

$$u_p^{(2)} = \sum_{r=0}^{N+2} D_{pr} u_r^{(1)} = \sum_{r=0}^{N+2} \sum_{k=0}^{N+2} D_{pr} D_{rk} u_k.$$

Therefore relabelling (A.1.10) and (A.1.11)

$$Lu = \sum_{i=0}^{N+2} \left(u_i^{(2)} + \lambda u_i \right) T_i.$$

Then using (A.1.4) we deduce (A.1.8) and it only remains to show that

$$u_i^{(2)} = \sum_{p=0}^{N+2} \sum_{k=0}^{N+2} D_{ip} D_{pk} u_k = \frac{1}{c_i} \sum_{p=i+2, p+i \text{ even}}^{N+2} p(p^2 - i^2) u_p. \tag{A.1.12}$$

To do this we use induction and (A.1.7). The differentiation matrices D and D^2 are established in the process.

To begin note the following

$$T_k'(x) = \sum_{r=0}^{N+2} D_{rk} T_r = D_{0k} T_0 + D_{1k} T_1 + \cdots + D_{N+2,k} T_{N+2}. \tag{A.1.13}$$

Using (A.1.7) we can write

$$\begin{aligned} T_k'(x) &= 2k(T_1 + T_2 + \cdots + T_{k-1}) \qquad \text{for } k \text{ even}, \\ T_k'(x) &= kT_0 + 2k(T_2 + T_3 + \cdots + T_{k-1}) \quad \text{for } k \text{ odd}, \end{aligned} \tag{A.1.14}$$

Therefore comparing the coefficients in (A.1.13) and (A.1.14) it can be deduce that

$$D_{0,2j} = 0, \quad j \geq 1, \tag{A.1.15}$$

$$D_{0,2j-1} = 2j - 1, \quad j \geq 1, \tag{A.1.16}$$

$$D_{i,i+2j-1} = 2(i + 2j - 1), \quad j \geq 1, \; i \geq 1, \tag{A.1.17}$$

$$D_{i,0} = 0, \quad i \geq 1, \tag{A.1.18}$$

or, in matrix form

$$D = \begin{pmatrix} 0 & 1 & 0 & 3 & 0 & 5 & 0 & 7 & \dots \\ 0 & 0 & 4 & 0 & 8 & 0 & 12 & 0 & \dots \\ 0 & 0 & 0 & 6 & 0 & 10 & 0 & 14 & \dots \\ \vdots & & & \ddots & & & & & \\ 0 & & & & & & & & \end{pmatrix}$$

To find D^2 we explicitly expand

$$u_i^{(2)} = \sum_{p=0}^{N+2} \sum_{k=0}^{N+2} D_{ip} D_{pk} u_k.$$

Then using (A.1.15) and comparing the coefficients of $u_i^{(2)}$ for $i = 0, \ldots, N+2$, it can be seen that

$$u_0^{(2)} = \frac{1}{2} \sum_{p=2,p \text{ even}}^{N+2} p^3 u_p,$$

$$u_1^{(2)} = \frac{1}{2} \sum_{p=3,p \text{ odd}}^{N+2} p(p^2-1) u_p,$$

$$u_2^{(2)} = \frac{1}{2} \sum_{p=4,p \text{ even}}^{N+2} p(p^2-2^2) u_p.$$

Hence by induction (A.1.12) is proved as required. Further expansion and comparison of the coefficients of u_p yields

$$D^2_{0,2j} = \frac{1}{2}(2j)^3, \quad j \geq 1,$$
$$D^2_{i,i+2j} = (i+2j)4j(i+j), \quad i \geq 1,\ j \geq 1,$$

which can be expressed in matrix form as

$$D^2 = \begin{pmatrix} 0 & 0 & 4 & 0 & 32 & 0 & 108 & \ldots \\ 0 & 0 & 0 & 24 & 0 & 120 & 0 & \ldots \\ 0 & 0 & 0 & 0 & 48 & 0 & 192 & \ldots \\ \vdots & & & \ddots & & & & \\ 0 & & & & & & & \end{pmatrix}$$

Note that the matrix $D^2 = D.D$ in the sense of matrix multiplication.

A.2 The Compound Matrix Method

To illustrate how the compound matrix method is implemented consider the simple 4th order eigenvalue problem as detailed in Straughan [94],

$$\begin{aligned} D^2 W &= a^2 W - R_E a^2 F(z,\lambda)\Theta, \\ D^2 \Theta &= a^2 \Theta - R_E F(z,\lambda) W, \end{aligned} \tag{A.2.1}$$

where W, Θ, z are unknown variables, and a^2, λ are constants we wish to minimise and maximise over respectively. F is an arbitrary function of z and λ, and R_E is the generalised eigenvalue of the system. Suppose we have boundary conditions

$$W = \Theta = 0, \qquad \text{on } z = 0, 1. \tag{A.2.2}$$

To solve (A.2.1) subject to (A.2.2) the compound matrix method proceeds as follows.

Let $\mathbf{W} = (W, W', \Theta, \Theta')^T$, and suppose $\mathbf{W}_1$ and $\mathbf{W}_2$ are solutions to (A.2.1) with initial values

$$\mathbf{W}_1(0) = (0, 1, 0, 0)^T, \qquad \mathbf{W}_2(0) = (0, 0, 0, 1)^T. \tag{A.2.3}$$

A new six vector

$$\mathbf{Y} = (y_1, y_2, y_3, y_4, y_5, y_6)^T,$$

is defined by the 2×2 minors of the 4×2 solution matrix $(\mathbf{W}_1, \mathbf{W}_2)$. Then,

$$\begin{aligned} y_1 &= W_1 W_2' - W_2 W_1', \\ y_2 &= W_1 \Theta_2 - W_2 \Theta_1, \\ y_3 &= W_1 \Theta_2' - W_2 \Theta_1', \\ y_4 &= W_1' \Theta_2 - W_2' \Theta_1, \\ y_5 &= W_1' \Theta_2' - W_2' \Theta_1', \\ y_6 &= \Theta_1 \Theta_2' - \Theta_2 \Theta_1' \end{aligned} \tag{A.2.4}$$

Differentiating (A.2.4) and using the governing equations (A.2.1), the initial value problem for y_i is found to be

$$\begin{aligned} y_1' &= -R_E F a^2 y_2, \\ y_2' &= y_3 + y_4, \\ y_3' &= a^2 y_2 + y_5, \\ y_4' &= a^2 y_2 + y_5, \\ y_5' &= R_E F y_1 + a^2 (y_3 + y_4) - R_E F a^2 y_6, \\ y_6' &= R_E F y_2. \end{aligned} \tag{A.2.5}$$

System (A.2.5) is integrated numerically from 0 to 1 subject to initial and final conditions. The initial values (A.2.3) yield $y_5(0) = 1$ and the boundary conditions at $z = 1$ give

$y_2(1) = 0$. The eigenvalue, R_E, is varied until $y_2(1) = 0$ is satisfied to some preassigned tolerance. In the computational work presented within this thesis the secant method was used to locate the root and a golden section search routine to find the critical eigenvalue

$$Ra_E = \max_{\lambda} \min_{a^2} R_E^2(a^2, \lambda).$$

More details and a thorough discussion of the compound matrix method, applied to energy eigenvalue problems can be found in Straughan [94].

Appendix B

Inequalities

B.1 Poincaré's Inequality

Let V be a cell in three dimensions. Suppose for simplicity V is the cell $0 \leq x < 2a_1$, $0 \leq y < 2a_2$, and $0 < z < 1$. Let u be a function periodic in x, y of period $2a_1, 2a_2$, respectively, and suppose $u = 0$ on $z = 0, 1$. Poincaré's inequality may be written as

$$\int_V u^2 dV \leq \frac{1}{\pi^2} \int_V |\nabla u|^2 dV. \tag{B.1.1}$$

In general, the constant $1/\pi^2$ in (B.1.1) depends on the geometry and size of the domain V. Further discussion of this and Poincaré's inequality can be found in Saloff-Coste [86].

B.2 Young's Inequality

Let a, b be arbitrary functions and p, q positive constants such that $1/p + 1/q = 1$, then Young's [106] inequality may be written as

$$ab \leq \frac{a^p}{p} + \frac{b^q}{q}. \tag{B.2.1}$$

An elementary derivation of Young's inequality in this form can be found in Beckenbach & Bellman [6], p.15.

Bibliography

[1] Allen MB. 1984. *Collocation Techniques for Modeling Compositional Flows in Oil Reservoirs.* Springer-Verlag, New York.

[2] Allen MB. 1986. Mechanics of multiphase fluid flows in variably saturated porous media. *Int. J. Engng. Sci.* **24**, 339–351.

[3] Allen MB & Khosravani A. 1992. Solute transport via alternating-direction collocation using the modified method of characteristics. *Advances in Water Resources.* **15**, 125–132.

[4] Baral DR, Hutter K & Greve R. 2001. Asymptotic theories of large-scale motion, temperature and moisture distribution in land-based polythermal ice sheets. A critical review and new developments. *Appl Mech Reviews.* **54(3)**, 215–256.

[5] Basurto & Lombardo. 2003. Global nonlinear stability in the Bénard problem for a mixture near the bifurcation point. *Continuum Mech. Thermodyn.* **15(3)**, 265–274.

[6] Beckenbach EF & Bellman R. 1965. *Inequalities.* Springer-Verlag, Berlin.

[7] Bénard H. 1900. Les tourbillons cellulaires dans une nappe liquide. *Revue générale des Sciences pures et appliquées.* **11**, 1261–1271, 1309–1328.

[8] Bénard H. 1901. Les tourbillons cellulaires dans une nappe liquide transportant de la chaleur par convection en régime permanent. *Annales de Chimie et de Physique.* **23**, 62–144.

[9] Bogorodskii PV & Nagurnyi AP. 2000. Under ice meltwater puddles: A factor of fast sea ice melting in the Arctic. *Doklady Earth Sciences.* **373**, 885–887.

[10] Brown GO. 2002. Henry Darcy and the making of a law. *Water Resources Research.* **38(07)**, 11.1–11.12.

[11] Carr M. 2003. A model for convection in the evolution of under-ice melt ponds. *Continuum Mech. Thermodyn.* **15(1)**, 45–54.

[12] Carr M. 2003. Unconditional nonlinear stability for temperature dependent density flow in a porous medium. *Math. Models. Methods. Appl Sci.* **13(2)**, 207–220.

[13] Carr M & de Putter S. 2003. Penetrative convection in a horizontally isotropic porous layer. *Continuum Mech. Thermodyn.* **15(1)**, 33–43.

[14] Carr M & Straughan B. 2003. Penetrative convection in a fluid overlying a porous layer. *Advances in Water Resources.* **26**, 263–276.

[15] Chandrasekhar S. 1981. *Hydrodynamic and Hydromagnetic Stability.* Dover, New York.

[16] Chasnov JR & Tse KL. 2001. Turbulent penetrative convection with an internal heat source. *Fluid Dyn. Res.* **28**, 397–421.

[17] Chen F & Chen CF. 1988. Onset of finger convection in a horizontal porous layer underlying a fluid layer. *J. Heat Transfer.* **110**, 403–409.

[18] Chen Q.-S, Prasad V & Chatterjee A. 1999. Modeling of fluid flow and heat transfer in a hydrothermal crystal growth system: Use of fluid-superposed porous layer theory. *J. Heat Transfer.* **121(4)**, 1049–1058.

[19] Clark PU, Pisias NG, Stocker TF & Weaver AJ. 2002. The role of thermohaline circulation in abrupt climate change. *Nature.* **415**, 863–869.

[20] Curran MC & Allen MB. 1990. Parallel computing for solute transport models via alternating direction collocation. *Advances in Water Resources.* **13**, 70–75.

[21] Darcy H. 1956. *Les fontaines publiques de la ville de Dijon.* Dalmont, Paris.

[22] Dawkins P, Dunbar S & Douglass R. 1998. The origin and nature of spurious eigenvalues in the spectral tau method. *J. Computational Phys.* **147**, 441–462.

[23] Dongarra JJ, Straughan B & Walker DW. 1996. Chebyshev tau - QZ algorithm methods for calculating spectra of hydrodynamic stability problems. *Appl. Numer. Math.* **22**, 399–435.

[24] Drazin PG & Reid WH. 1981. *Hydrodynamic Stability.* Cambridge University Press.

[25] Dupuit J. 1863. *Etudes Théoriques et Pratiques sur le Mouvement des Eaux.* Dunod, Paris.

[26] Eicken H. 1994. Structure of under-ice melt ponds in the central Arctic and their effect on the sea-ice cover. *Limnol. Oceanogr.* **39(3)**, 682–694.

[27] Eicken H, Krouse HR, Kadko D & Perovich DK. 2002. Tracer studies of pathways and rates of meltwater transport through Arctic summer sea ice. *J. Geophys. Res.* **107(C10), 8046**, 22.1–22.20.

[28] El-Habel F, Mendoza C & Bagtzoglou AC. 2002. Solute transport in open channel flows and porous streambeds. *Advances in Water Resources.* **25**, 455–469.

[29] Ewing RE. 1996. Multidisciplinary interactions in energy and environmental engineering. *J. Comp. Appl. Math.* **74**, 193–215.

[30] Ewing RE & Weekes S. 1998. Numerical methods for contaminant transport in porous media. *Computational Mathematics.* **202** (Marcel Decker, Inc., New York), 75–95.

[31] Forchheimer P. 1901. Wasserbewegung durch Boden. *Zeitschrift für Vereines Deutscher Ingnieure.* **50**, 1781–1788.

[32] Fox L. 1962. Chebyshev methods for ordinary differential equations. *Computer J.* **4**, 318–331.

[33] George JH, Gunn RD & Straughan B. 1989. Patterned ground formation and penetrative convection in porous media. *Geophys. Astrophys. Fluid Dyn.* **46**, 135–158.

[34] Ghosal S & Spiegel EA. 1991. On thermonuclear convection: I. Shellular instability. *Geophys. Astrophys. Fluid Dyn.* **61**, 161-178.

[35] Giorgi T. 1997. Derivation of the Forchheimer law via matched asymptotic expansions. *Transport in porous media.* **29**, 191–206.

[36] Givler RC & Altobelli SA. 1994. A determination of effective viscosity for the Brinkman-Forchheimer flow model. *J. Fluid Mechs.* **258**, 355–370.

[37] Gleason KJ. 1984. *Nonlinear Boussinesq Convection in Porous Media: Application to Patterned Ground Formation.* M.S. Thesis, Univ. Colorado.

[38] Goldman E. 2002. Even in high Arctic nothing is permanent. *Science.* **297**, 1493.

[39] Hansen U & Yuen DA. 1989. Subcritical double-diffusive convection at infinite Prandtl number. *Geophys and Astrophys Fluid Dyns.* **47**, 199–224.

[40] Hutter K. 1983. *Theoretical Glaciology: Material Science of Ice and the Mechanics of Glaciers and Ice Sheets.* Reidel, Dordrecht.

[41] Joseph DD. 1969. Uniqueness criteria for the conduction-diffusion solution of the Boussinesq equations. *Arch. Rational Mech. Anal.* **35(3)**, 169–177.

[42] Kerr R. 2002. A warmer Arctic means change for all. *Science.* **297**, 1490–1493.

[43] Kessler MA & Werner BT. 2003. Self organization of sorted patterned ground. *Science.* **299**, 380–383.

[44] Krantz WB, Gleason KJ & Caine N. 1988. Patterned ground. *Scientific American.* **256**, 68–76.

[45] Krishnamurti R. 1997. Convection induced by selective absorption of radiation: a laboratory model of conditional instability. *Dynamics of Atmospheres and Oceans.* **27**, 367–382.

[46] Larson VE. 2000. Stability properties of and scaling laws for a dry radiative-convective atmosphere. *Q. J. Royal Meteorological Soc.* **126**, 145–171.

[47] Larson VE. 2001. The effects of thermal radiation on dry convective instability. *Dynamics of Atmospheres and Oceans.* **34**, 45–71.

[48] Lombardo S, Mulone G & Rionero S. 2000. Global stability in the Bénard problem for a mixture with superimposed plane parallel shear flows. *Math. Methods Appl. Sci.* **23**, 1447–1465.

[49] Lombardo S, Mulone G & Rionero S. 2001. Global nonlinear exponential stability of the conduction-diffusion solution for Schmidt numbers greater than Prandtl numbers. *J. Math. An. and Appl.* **262**, 191–207.

[50] Lombardo S, Mulone G & Straughan B. 2001. Non-linear stability in the Bénard problem for a double-diffusive mixture in a porous medium. *Math. Methods Appl. Sci.* **24**, 1229–1246.

[51] McKay G & Straughan B. 1991. The influence of a cubic density law on patterned ground formation. *Math. Models. Meth. Appl Sci.* **1(1)**, 27–39.

[52] McKay G & Straughan B. 1992. Non-linear energy stability and convection near the density maximum. *Acta Mechanica.* **95**, 9–28.

[53] McKay G & Straughan B. 1993. Patterned ground formation under water. *Continuum Mech. Thermodyn.* **5**, 145–162.

[54] McKenzie DP, Roberts JM & Weiss NO. 1974. Convection in the earth's mantle: towards a numerical simulation. *J. Fluid Mech.* **62**, 465–538.

[55] Malin Space Science Systems. (11 May 1999). South Melea Planum, By The Dawn's Early Light. *MGS MOC Release No. MOC2-126.*

[56] Malin Space Science Systems. (19 July 1999). Indications of Subsurface Ice: Polygons on the Nothern Plains. *MGS MOC Release No. MOC2-150.*

[57] Malin Space Science Systems. (29 May 2002). Southern Hemisphere Polygonal Patterned Ground. *MGS MOC Release No. MOC2-315.*

[58] Mann D. 2003. On patterned ground. *Science.* **299**, 354–355.

[59] Martin S & Kauffman P. 1974. The evolution of under-ice melt ponds, or double diffusion at the freezing point. *J. Fluid Mech.* **64(3)**, 507–527.

[60] Matthews PC. 1988. A model for the onset of penetrative convection. *J. Fluid Mech.* **188**, 571–583.

[61] Merker GP, Waas P & Grigull U. 1979. Onset of convection in a horizontal water layer with maximum density effects. *Int. J. Heat Mass Transfer.* **22**, 505–515.

[62] Moler CB & Stewart GW. 1973. An algorithm for generalized matrix eigenproblems. *SIAM Journal of Numerical Analysis.* **10**, 241–256.

[63] Moore DR & Weiss NO. 1973. Nonlinear penetrative convection. *J. Fluid Mech.* **61**, 553–581.

[64] Mulone G. 1994. On the nonlinear stability of a fluid layer of a mixture heated and salted from below. *Continuum Mech. Thermodyn.* **6**, 161–184.

[65] Ng BS & Reid WH. 1979. An intial-value method for eigenvalue problems using compound matrices. *J. Comp. Phys.* **30**, 125–136.

[66] Ng BS & Reid WH. 1980. On the numerical solution of the Orr-Sommerfeld problem: asymptotic initial conditions for shooting methods. *J. Comp. Phys.* **38**, 275–293.

[67] Ng BS & Reid WH. 1985. The compound matrix method for ordinary differential systems. *J. Comp. Phys.* **58**, 209–228.

[68] Nield DA. 1977. Onset of convection in a fluid layer overlying a layer of a porous medium. *J. Fluid Mech.* **81**, 513–522.

[69] Nield DA. 1983. The boundary correction for the Rayleigh-Darcy problem: limitations of the Brinkman equation. *J. Fluid Mech.* **128**, 37–46.

[70] Nield DA. 1991. The limitations of the Brinkman-Forchheimer equation in modelling flow in a saturated porous medium and at an interface. *Int. J. Heat & Fluid Flow.* **12**, 269–272.

[71] Nield DA. 1998. Instability and turbulence in convective flows in porous media. In *Nonlinear Instability, Chaos and Turbulence*, pp. 225–276. Eds. L. Debnath & D.N. Riahi, WIT Press, Boston, Southampton.

[72] Nield DA. 1998. Modelling the effect of surface tension on the onset of natural convection in a saturated porous medium. *Transport in Porous Media.* **31**, 365–368.

[73] Nield DA & Bejan A. 1999. *Convection in Porous Media.* Second Edition. Springer - Verlag, New York.

[74] Notz D, McPhee MG, Worster MG, Maykut GA, Schlunzen KH & Eicken H. 2003. Impact of underwater-ice evolution on Arctic summer sea ice. *J. Geophys. Res.* To appear.

[75] Orszag SA. 1971. Accurate solution of the Orr-Sommerfeld stability equation. *J. Fluid Mech.* **50(4)**, 689–703.

[76] Payne LE & Straughan B. 1987. Unconditional nonlinear stability in penetrative convection. *Geophys. Astrophys. Fluid Dyn.* **39**, 57–63 (see also, Corrected and extended numerical results. *Geophys. Astrophys. Fluid Dyn.* **43**, 307–309).

[77] Payne LE & Straughan B. 1999. Convergence and continuous dependence for the Brinkman-Forchheimer equations. *Stud. Appl. Math.* **102**, 419–439.

[78] Payne LE & Straughan B. 2000. Unconditional Nonlinear Stability in Temperature-Dependent Viscosity Flow in a Porous Medium. *Stud. Appl. Math.* **105**, 59–81.

[79] Proctor MRE. 1981. Steady subcritical thermohaline convection. *J. Fluid Mech.* **105**, 507–521.

[80] Qin Y & Kaloni PN. 1994. Convective instabilities in anisotropic porous media. *Stud. App. Math.* **91**, 189–204.

[81] Rahmstorf S. 2001. *Abrupt Change.* Encyclopedia of Ocean Sciences. Academic Press, London, p.1–6.

[82] Rignot E & Thomas RH. 2002. Mass balance of polar ice sheets. *Science.* **297**, 1502–1506.

[83] Roberts PH. 1967. Convection in horizontal layers with internal heat generation, Theory. *J. Fluid Mech.* **30**, 33–49.

[84] Rodrigues JF & Urbano JM. 1999. On a Darcy-Stefan problem arising in freezing and thawing of saturated porous media. *Continuum Mech. Thermodyn.* **11**, 181–191.

[85] Rothrock DA, Yu Y & Maykut G. 1999. Thinning of the Arctic sea-ice cover. *Geophys Res Letts.* **26(23)**, 3469–3472.

[86] Saloff-Coste L. 2002. *Aspects of Sobolev-Type Inequalities.* University Press, Cambridge.

[87] Schmittner A, Yoshimori M & Weaver AJ. 2002. Instability of glacial climate in a model of the ocean-atmosphere-cryosphere system. *Science.* **295**; 1489–1493.

[88] Schubert G, Turcotte DL & Oxburgh ER. 1969. Stability of planetary interiors. *Geophys. J. R. Astron. Soc.* **18**, 441–460.

[89] Selak R & Lebon G. 1997. Rayleigh-Marangoni thermoconvective instability with non-Boussinesq corrections. *Int. J. Heat Mass Trans.* **40**, 785-798.

[90] Shir CC & Joseph DD. 1968. Convective instability in a temperature and concentration field. *Arch. Rational Mech. Anal.* **30(1)**, 38–80.

[91] Straughan B. 1993. *Mathematical Aspects of Penetrative Convection.* Longman, Harlow.

[92] Straughan B. 2001. Surface tension driven convection in a fluid overlying a porous layer. *J. Computational Phys.* **170**, 320–337.

[93] Straughan B. 2002. Effect of property variation and modelling on convection in a fluid overlying a porous layer. *Int. J. Num. Anal. Meth. Geomech.* **26**, 75–97.

[94] Straughan B. 2003. *The Energy Method, Stability, and Nonlinear Convection.* Second Edition. Springer-Verlag, New York.

[95] Straughan B & Walker DW. 1996. Two very accurate and efficient methods for computing eigenvalues and eigenfunctions in porous convection problems. *J. Comp. Phys.* **127**, 128–141.

[96] Straughan B & Walker DW. 1996. Anisotropic porous penetrative convection. *Proc. R. Soc. Lond.* A **452**, 97–115.

[97] Suchomel BJ, Chen BM & Allen MB. 1998. Network model of flow, transport and biofilm effects in porous media. *Transport in Porous Media.* **30**, 1–23.

[98] Suchomel BJ, Chen BM & Allen MB. 1998. Macroscale properties of porous media from a network model of biofilm processes. *Transport in Porous Media.* **31**, 39–66.

[99] Tracey J. 1997. *Stability Analysis of Multi-Component Convection-Diffusion Problems.* PhD. Thesis, Univ. Glasgow.

[100] Tse KL & Chasnov JR. 1998. A Fourier-Hermite pseudospectral method for penetrative convection. *J. Computational Phys.* **142**, 489–505.

[101] Unterberg W. 1964. Thermophysical properties of aqueous sodium chloride solutions. *Dept Eng. UCLA.* Rept 64-21.

[102] Veronis G. 1963. Penetrative convection. *Astrophys. J.* **137**, 641–663.

[103] Wadhams P & Davis NR. 2000. Further evidence of ice thinning in the Arctic Ocean. *Geophys Res Letts.* **27(24)**, 3973–3975.

[104] Wadhams P & Davis NR. 2001. Arctic sea-ice morphological characteristics in summer 1996. *Anns. Glaciology.* **33**, 165–170.

[105] Whitaker S. 1996. The Forchheimer equation: a theoretical development. *Transport in porous media.* **25**, 27–62.

[106] Young WH. 1912. On classes of summable functions and their Fourier series. *Proc. Roy. Soc.* A **87**, 225–229.

[107] Zhang KK & Schubert G. 2000. Teleconvection: remotely driven thermal convection in rotating stratified spherical layers. *Science.* **290**, 1944–1947.

[108] Zhang KK & Schubert G. 2002. From penetrative convection to teleconvection. *Astrophys J.* **572**, 461–476.